

Experimental and Numerical Investigation of the Mechanical Response of Injection Moulded Polypropylene Materials

Doctoral Dissertation by

Hamid Daiyan



Submitted to the Faculty of Mathematics and Natural Sciences at the
University of Oslo in partial fulfilment of the requirements for the degree
Philosophiae Doctor (PhD)

2011

Dedicated to my parents

When you do things from your soul,

You feel a river moving in you, a joy.

Rumi (1207–1273)

Abstract

The mechanical response of polymer materials and components subjected to impact loading is of increasing interest, as these materials are frequently applied in critical applications. The response to impact loads is of particular interest in automotive applications related to passenger and pedestrian safety, in which the material may undergo large multiaxial deformations at high strain rates. Numerical simulation is attractive because it reduces cost and time in the product development phase. The present thesis focuses on ductile thermoplastic materials; polypropylene compounds containing elastomers and talc. These compounds are developed for injection-moulded automotive exterior parts such as bumper covers. The aim of the thesis is to contribute to improving material models and test methods, thereby improving the numerical prediction of the response to impact loading. All numerical simulations were performed with LS-DYNA, a commercial nonlinear finite element analysis software package which is one of the most well-known codes for impact and crash applications. Numerical simulations require an adequate material model, calibrated with reliable experimental data. The material model which was used and evaluated in this thesis, SAMP-1, is specially developed for polymeric materials. SAMP-1 is a linear-elastic-viscoplastic model, which features pressure-dependent yield stress, plastic dilatation (plastic Poisson's ratio < 0.5) and a simple damage model.

The model was calibrated with data from tests in uniaxial tension, uniaxial compression and shear. Test methodologies and material responses were studied, in particular for tests in uniaxial tension and shear. 3D digital image correlation with two cameras and stereo-vision was used to determine full-field in-plane and out-of-plane displacements during the tests. From these data, true-cross sections and strains were calculated. For the tensile tests, the true stress-strain, as well as the volume strain, was obtained by DIC. Two in-plane shear test fixtures/geometries were used; Iosipescu and V-Notched-Rail. For these two geometries and three different materials, shear strain distributions, strain triaxiality and crack initiation, were assessed by DIC, and the two test geometries were compared. For the calibration tests in general inverse modelling could be employed to improve the input to the models.

With the calibrated material model (SAMP-1), two load cases were simulated; centrally loaded clamped plates and three-point bending of bars. The predictions of force vs. deflection were good to fair. The results were discussed in terms of the deficiencies of the calibration data, the heterogeneity and anisotropy of the injection-moulded components, and shortcomings of the model. In particular, the hardening curves at high strain rates are uncertain, and tests in biaxial tension would be useful.

The performance of the materials at low temperatures was the topic of an experimental study. The impact response was characterised by instrumented falling-weight impact testing of plates with annular clamping. Different loading conditions were assessed by varying plate thickness, moulding conditions, incident impact velocity, testing temperature (-60 to 20 °C), striker geometry, clamping, plate surface texture, melt flow weld lines, and paint. The occurrence of brittle and ductile failures and the macroscopic fracture patterns were investigated experimentally.

Acknowledgement

I would like to thank all people who have helped and inspired me during my doctoral study. This thesis is the result of valuable contribution of individuals and organizations. The PhD studentship was funded by the Research Council of Norway (BIA programme) and Plastal AS.

I especially want to express my sincere thank to my advisor, Erik Andreassen, for his guidance during my research at SINTEF. His continuous energy and interest in research always motivated me. In addition, he was always accessible and willing to help his students with their research. I would also like to thank my co-advisors, Harald Osnes and Frode Grytten, for their time and effort and especially for their helpful discussion and suggestions.

Many thanks to Rune Gaarder, Philippe Brachet, Helene Amedro and Mariusz Blochowiak for their experimental advice and measurements. Thanks to Mario Polanco-Loria at SINTEF in Trondheim for his kind collaboration, and to Einar Hinrichsen, the research group leader.

I had a great time with my friendly officemates, Terje Tofteberg, Jakub Kalus and lately Tuan-Anh Nguyen and Le Thuy Truong. I am also thankful to Shifte Mihanyar, Amin Farjad Bastani and Saeed Bikass, other Iranian Ph.D. student at SINTEF, for their encouragements and made me feel like I was home while I was approximately 6500 km away from my home town.

I would like to express my deepest thanks to my entire family, especially my parents, for their support and inspiration throughout the years.

Lastly, I appreciate all the assistance I received during this wonderful journey.

Hamid Daiyan
Narvik, March 2011

Table of Contents

Scope of the thesis	viii
Part A Introduction	
1. Motivation and Scope	2
2. General introduction	3
2.1. Polypropylene	3
2.1.1. Polypropylene chains – tacticity, copolymerization	3
2.1.2. Crystallization – lamellae and spherulites	4
2.2. Mechanical properties.....	5
2.2.1. Deformation mechanisms at the micro scale	6
2.3. The injection moulding process	7
2.3.1. The process and applications	7
2.3.2. Process-induced features and defects	8
2.4. Numerical simulation of mechanical response	9
3. Materials and methodologies in this thesis	13
3.1. Materials and processing	13
3.2. Numerical simulation	15
3.2.1. Material model	15
3.3. Calibration procedure.....	20
3.4. Mechanical testing	22
3.4.1. Digital image correlation (DIC)	22
3.4.2. Providing input to numerical simulations	23
3.4.2.1. Uniaxial tension	23
3.4.2.2. Uniaxial compression	24
3.4.2.3. Shear	24
3.4.3. Material performance and verification tests	25
3.4.3.1. Instrumented falling weight impact	25
4. Conclusion	27
Bibliography	28

Part B Papers

Paper 1	32
H. Daiyan, E. Andreassen, F. Grytten, O.V. Lyngstad, T. Luksepp, H. Osnes	
Low-velocity impact response of injection-moulded polypropylene plates – Part 1: Effects of plate thickness, impact velocity and temperature	
<i>Polymer Testing</i> , Volume 29, Issue 6, 2010, Pages 648-657	
Paper 2	43
H. Daiyan, E. Andreassen, F. Grytten, O.V. Lyngstad, T. Luksepp, H. Osnes	
Low-velocity impact response of injection-moulded polypropylene plates – Part 2: Effects of moulding conditions, striker geometry, clamping, surface texture, weld line and paint	
<i>Polymer Testing</i> , Volume 29, Issue 7, 2010, Pages 894-901	
Paper 3	52
F. Grytten, H. Daiyan, M. Polanco-Loria, S. Dumoulin	
Use of digital image correlation to measure large-strain tensile properties of ductile thermoplastics	
<i>Polymer Testing</i> , Volume 28, Issue 6, 2009, Pages 653-660	
Paper 4	61
H. Daiyan, E. Andreassen, F. Grytten, H. Osnes, R. H. Gaarder	
Shear testing of polypropylene materials analysed by digital image correlation and numerical simulations	
Paper 5	80
H. Daiyan, E. Andreassen, F. Grytten, H. Osnes, O.V. Lyngstad	
Numerical simulation of low-velocity impact loading of a ductile thermoplastic material	
Paper 6	94
M. Polanco-Loria, H. Daiyan, F. Grytten	
Material parameters identification: An inverse modelling procedure applicable for thermoplastic materials	
Accepted for publication, <i>Polymer Engineering & Science</i> , 2011	

Scope of the thesis

This thesis deals with the mechanical properties of polypropylene (a thermoplastic polymer material), investigated using a combined experimental and numerical approach.

Part A of the thesis introduces the polymer material (polypropylene), the processing (injection moulding), the experimental methodology, the material model and the numerical simulations. **Part A** is followed by **Part B** which consists of six papers.

Paper 1 and **paper 2** deal with the response of polypropylene plates subjected to impact loading. Both ductile and brittle behaviour was observed under different temperature and loading condition. Effects of the plate thickness, injection moulding processing, surface roughness, paint and weld line was considered.

In the next two papers, **paper 3** and **paper 4**, the mechanical response of the thermoplastic material was measured experimentally. **Paper 3** presents a 3D digital image correlation (DIC) technique which was applied to determine the tensile behaviour of these ductile materials. These materials usually show a strong localized deformation. Using DIC gives the opportunity to measure the strain locally. A comparison of the local and average strain over the gauge length shows considerable differences for large strains. The average strain was obtained using a standard extensometer. It is worth mentioning that the higher accuracy of the extensometer makes it more desirable than DIC for small strains. The constant volume assumption after yielding in tension is not valid for this material. In **paper 3**, 3D DI was also utilized in order to measure the true cross section. The Cauchy stress was derived by true cross section and the applied force. Other material parameters such as Poisson's ratio and local strain rate were also extracted from the measured data. **Paper 4** deals with the determination of material parameters from shear testing. Three polypropylene compounds were tested using both the V-Notched-Rail test and the Iosipescu test. The aim of this work was to obtain reliable shear data for the pre and post yield regimes. DIC and numerical simulations were the supportive tools in this work. The paper presents an evaluation of these two shear test methods for three different polypropylene materials.

The first four papers deal with experimental characterization. The aim of the experimental studies was to characterise the material behaviour under different loading conditions, and obtain reliable data which can be used as an input for numerical simulations. **Paper 5** and **paper 6** both present numerical simulation results. The aim of **paper 5** is to establish and validate numerical models for impact response. All simulation were performed in LS-DYNA and the material model, SAMP-1, was calibrated from the experimental results presented in the previous papers. SAMP-1 is a material model which includes a pressure dependent yield surface, plastic dilation and strain rate sensitivity. For small and moderate deformations a good correlation between tests and simulations was obtained. Nevertheless, still some improvement is needed to predict large deformation under biaxial tension. Some extreme case of validation tests are reported and discussed in **paper 5**. The aim of **paper 6** is to propose a new material model calibration methodology. This methodology is based on the local behaviour and it was performed by using LS-OPT, a graphical optimization tool that interfaces with LS-DYNA.

In addition to the six papers, some results have been presented at conferences and workshops:

- H. Daiyan, E. Andreassen, F. Grytten, H. Osnes, M. Polanco-Loria, "Impact response of polypropylene plates", 3rd International Conference on Impact Loading of Lightweight Structures, Valenciennes, France, June 2011.
- H. Daiyan, F. Grytten, E. Andreassen, M. Polanco-Loria, S. Dumoulin, "Three-dimensional digital image correlation in constitutive property measurement and model verification", Invited lecture, LIMESS User Meeting, Berlin, Germany, October 2009.
- H. Daiyan, F. Grytten, E. L. Hinrichsen, E. Andreassen, "Some effects of processing on the mechanical response of polyolefins", Invited lecture, International workshop on behavior and modeling of polymers, Trondheim, Norway, June 2009.
- H. Daiyan, F. Grytten, E. Andreassen, O. V. Lyngstad, H. Osnes, R. H. Gaarder, E. L. Hinrichsen, "Numerical simulation of low-velocity impact loading of polymer materials", 7th European LS-DYNA Conference, Salzburg, Austria, May 2009.
- H. Daiyan, E. Andreassen, F. Grytten, O. V. Lyngstad, T. Luksepp, E. L. Hinrichsen, "Impact response of injection-moulded polypropylene parts for automotive exteriors", 14th International Conference on Deformation, Yield and Fracture of Polymers, Kerkrade, The Netherlands, April 2009.
- Andreassen, H. Daiyan, F. Grytten, O.V. Lyngstad, R.H. Gaarder, E.L. Hinrichsen, "Mechanical Testing for Generating Input to Numerical Simulation of Impact Response of Injection-Moulded Components", PPS-24, Salerno, Italy, June 2008.
- H. Daiyan, E. Andreassen, F. Grytten, O.V. Lyngstad, R.H. Gaarder, E.L. Hinrichsen, "Mechanical Properties of Injection-Moulded Automotive Parts", Impact Loading of Lightweight Structures, Trondheim, Norway, June 2008.

Part A
Introduction

1 Motivation and scope

The response of polymeric materials subjected to impact loading is of increasing interest, as these materials are frequently applied in critical applications and constructions. The response to impact loads is of particular interest in automotive applications related to passenger and pedestrian safety (Figure 1), in which the material may undergo large multi-axial deformations at high strain rates. The automotive industry is therefore a driving force in this field. Electronic casings and various “everyday” products must also be designed to resist impact loads.

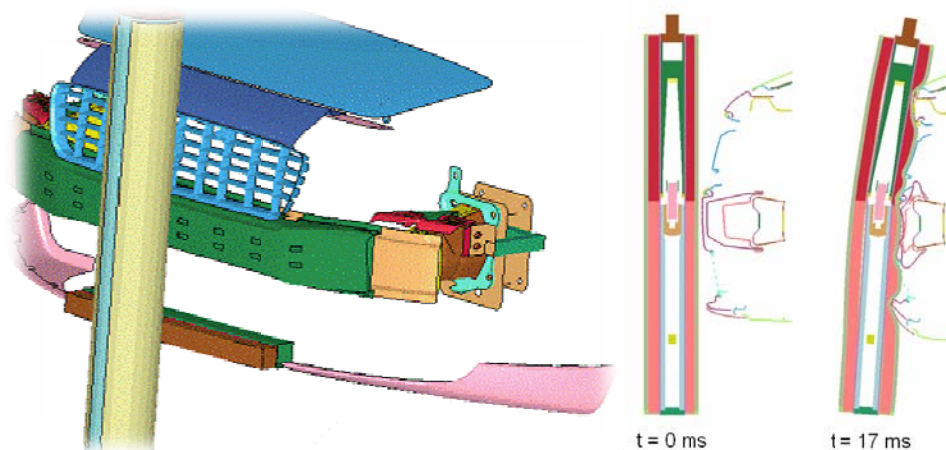


Figure 1 Simulation of a pedestrian-car accident in LS-DYNA. Impact speed: 40 km/h. Figures by Plastal AS.

Various commercial simulation codes have suitable numerical techniques to simulate the dynamic event of an impact. Most of the constitutive models in these codes, however, were developed for metals. As regards polymeric materials, a reliable constitutive description is not yet available. One reason for this is that the mechanical response of polymers can be more complex than for metals. Polymeric materials used in components designed to withstand impact and/or absorb impact energy are usually highly ductile. Ductile polymeric materials show a complex behaviour in impact loading involving large strains. The complexity applies to the micromechanical mechanisms as well as the macroscopic response. Therefore, more complex constitutive models are needed, requiring material input which may be difficult to determine experimentally. Data from experiments with well-defined stress states, e.g. shear, are needed as input for numerical simulation. Furthermore, true (local) stress-strain data must be calculated from the experiments, and these data should preferentially extend to as high strains and strain rates as possible.

The topic of the thesis is the mechanical behaviour of ductile thermoplastic materials (polypropylene compounds). Specifically, the thesis deals with the following topics:

- A. Impact response of injection-moulded plates to improve the understanding of material performance, particularly at low temperatures.
- B. Improved tests and specimen geometries for shear, uniaxial compression and uniaxial tension at low strain rates (by application of 3D digital image correlation) and some tensile tests at high strain rates. Methodology to calibrate the material model with these data.
- C. With the calibrated model, numerical simulation of impact loading cases (three-point bending, impact of plate) and comparison with experiments.

2 General introduction

2.1 Polypropylene

Polypropylene (PP) is a semi-crystalline thermoplastic polymer with a large variety of applications. It offers a cost-effective combination of physical, mechanical and thermal properties [1-5]. The global consumption of PP is around 47 million tons per year and the consumption of PP per capita in Europe is 17 kg per year [6]. It is worth mentioning that 19% of the European production of plastics is PP. The automotive sector uses about 7 % of the PP production [7], and PP is the single most used polymer material in cars with an average of 60 kg/car, and the trend is upwards [8].

2.1.1 Polypropylene chains – tacticity, copolymerization

Polypropylene is produced by polymerization of propylene ($\text{CH}_2=\text{CHCH}_3$). Most PP materials are dominantly isotactic. In isotactic polypropylene (iPP), all methyl groups are positioned at the same side with respect to the backbone of the polymer chain, Figure 2. PP can also be syndiotactic or atactic, depending on the polymerization process. In syndiotactic polypropylene (sPP), the methyl groups are positioned in a regular fashion from one side of the chain to the other with respect to the backbone of the polymer chain, see. In atactic polypropylene (aPP), the methyl groups are positioned in a random configuration. aPP is an amorphous wax-like polymer with poor mechanical properties since the structure is irregular and it does not crystallize.

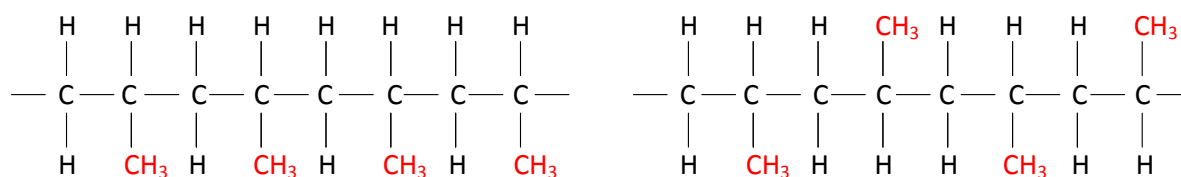


Figure 2 Schematic representation of isotactic (left) and syndiotactic (right) polypropylene.

Three main types of PP materials can be distinguished: **Homopolymer** (stiff but brittle at low temperatures). **Random copolymer**, i.e. a propylene-ethylene copolymer with propylene being the main component. **Heterophasic copolymer** also referred to as “block copolymer”, impact-modified PP, high-impact PP etc. Today this is typically a polypropylene homopolymer (iPP) matrix reactor-blended with an ethylene-propylene random copolymer (or rubber) (EPR), and a series of ethylene-propylene block copolymers with different sequence lengths (some propylene-rich and some ethylene-rich) [9]. A heterophasic copolymer has good impact properties down to e.g. -30 °C, while retaining a sufficient elastic modulus at the highest service temperatures. PP grades use in car exteriors (the materials in this thesis) are heterophasic copolymers with fillers such as talc in order to optimize the stiffness/toughness balance and reduce thermal expansion and shrinkage.

2.1.2 Crystallization – lamellae and spherulites

The tacticity has a strong effect on the polymer's ability to form crystals. The chain must be regular (isotactic or syndiotactic) in order to crystallize. For iPP, a three-fold helix with periodicity 0.65 nm is found in all crystalline forms. The energy of this helix conformation is close to the absolute minimum for the polymer chain.

PP is semi-crystalline polymer, i.e. it has both crystalline and amorphous regions. Semi-crystallinity is a desirable property for most plastics, because the strength of crystalline polymers is combined with the flexibility of amorphous phases, especially when the latter is above the glass transition temperature. During the solidification process the PP chains crystallize in the form of lamella (plate-like crystals). The most common crystalline structure of isotactic PP is the α structure shown in Figure 3. The lamella are often organized in a spherical shape known as a spherulite [10]. A schematic drawing of spherulite is shown in Figure 4.

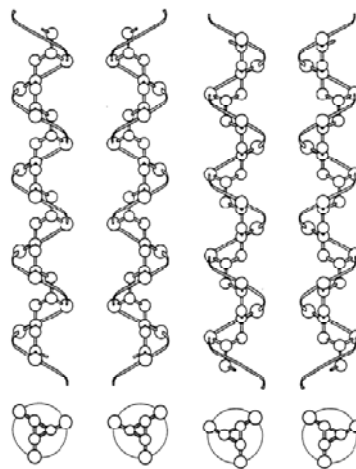


Figure 3 Chain conformations of isotactic polypropylene in the unit cell of the α phase. Helices in their up and down as well as right and left configurations. Source: van der Burgt, PhD thesis [11].

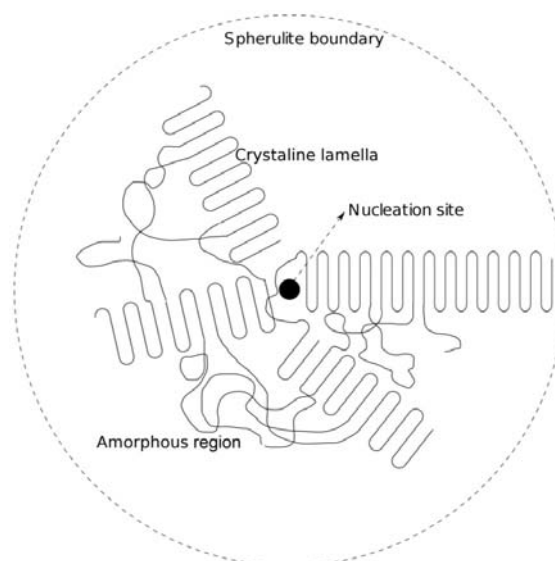


Figure 4 Schematic representation of the spherulite (semi-crystalline region). Source: Wikipedia.

2.2 Mechanical properties

The mechanical properties of semi-crystalline polymers strongly depend on the degree of crystallinity, the crystallite size and the concentration of tie-chains. The tie-chains connect the adjacent crystals (lamellae). In addition, the (average) molecular weight and the molecular weight distribution (MWD) also affect the mechanical properties. Nucleating agents can reduce the cycle time in the injection moulding process, increase the stiffness, increase the tie-chain concentration, improve the clarity, promote the β phase etc.

Single crystals (lamellae) are highly anisotropic because of the nature of bonding between atoms and molecules, strong covalent bonds along the chain vs. weak van der Waals interaction etc between chains, see Figure 5(left). Random formations of spherulite structure in the 3D space create an isotropic composition [12]. Therefore, even if the individual crystals are anisotropic, the differences in the properties tend to average and, overall, the material is isotropic. Note that the degree of crystallinity and molecular orientation are affected by the fabrication process, which could lead to anisotropic mechanical response in solid polymers.

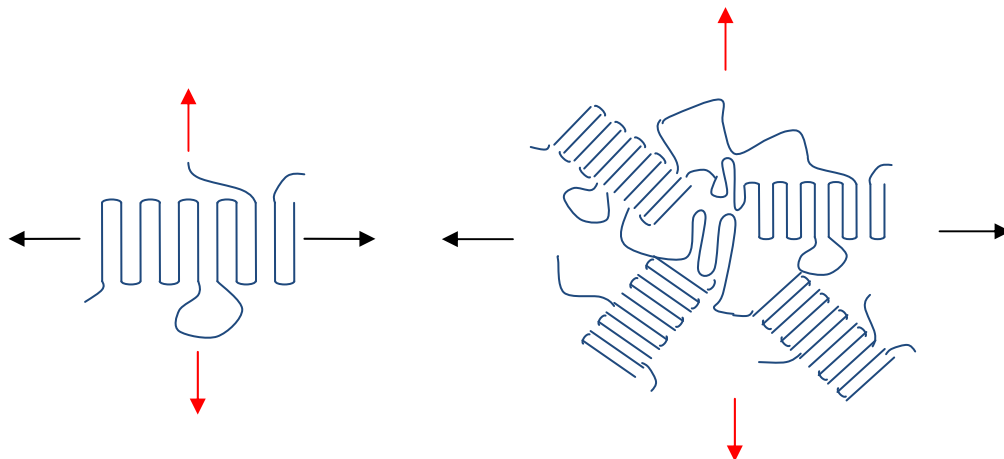


Figure 5 Illustration of a single crystalline lamella (left) and the spherulite (right).

The mechanical properties of polypropylene depend on the structure of the crystals. Isotactic polypropylene can crystallize at least in three different forms, the α (Figure 3), β and γ phases. The monoclinic α phase is the most common and most stable phase in iPP. The β phase, with a hexagonal crystal structure, is formed under special conditions like shear, temperature gradients or in the presence of nucleating agents. It has been reported that the impact resistance is improved by the β phase. Finally, the less common γ phase has a triclinic crystal structure and its formation is related to pressure and molecular weight.

Commercial polypropylene materials are blended with a number of additives in order to improve the properties. Inorganic fillers, rubber, carbon black, antioxidants and nucleating agents are the most important ones. One of the most important and common industrial fillers for polypropylene is talc. Talc as a mineral filler improves the mechanical (stiffness and creep resistance) and thermal properties [13], and it also reduces the price in some cases. Talc is also a nucleating agent for PP and as such it may enhance the mechanical properties of the compound [14]. Increasing the filler content leads to an increase in the mechanical strength of the material, but in most cases with a simultaneous decrease in the fracture toughness [15]. If the stress reaches a critical value, micro

cracks are initiated around the particles (e.g. talc) [16, 17] and failure results. A rubbery second phase is added to the matrix for the purpose of increasing the toughness which concurrently results in a reduction of the stiffness [18]. The second phase, by making the craze initiation easier (void formation), significantly affects the toughness [19]. This is often referred to as the "rubber toughening mechanism". Usually a balance between toughness and stiffness is required in most industrial applications.

2.2.1 Deformation mechanisms at the micro scale

In general, two stages of deformation can be considered; pre-yield and post-yield behaviour. The pre-yield deformation is dominated by the deformation and uncoiling of the amorphous phase and the van der Waals interaction, much weaker than covalent chemical bonds, contribute at this step [20]. The post-yield deformation comprises several complex stages and it depends on the level of strain and the stress state. A simplified model of deformation is illustrated in Figure 6. Plastic deformation occurs by tilting of the lamellae so that the chain folds become more aligned, followed by separation of the crystalline block segments [20].

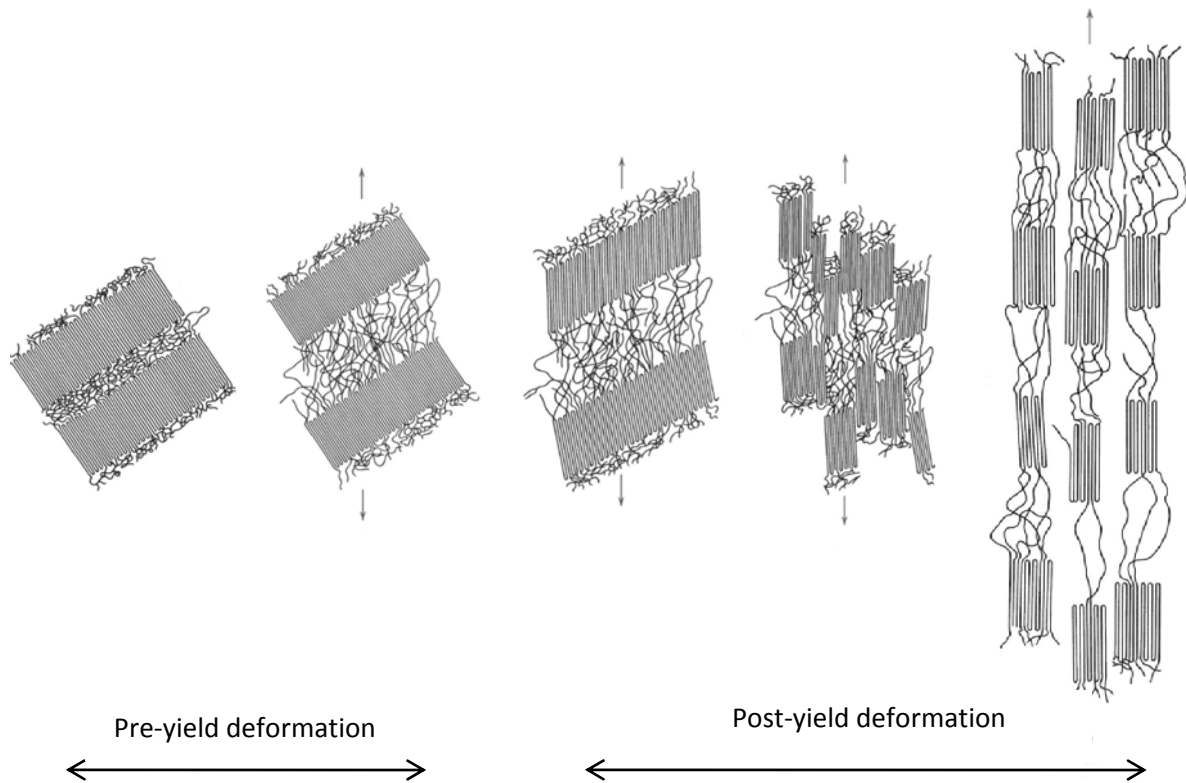


Figure 6 Deformation of semi-crystalline polymer. Source: Callister [20].

Yielding in polymers occurs either through shear or crazing [17]. Shear yielding consists of the sliding of molecules with respect to each other and happens when the shear stress reaches a critical value. It forms in the maximum shear stress direction, which is 45° to the principal stress [21]. Shear yielding is considered as local deformation and it is not associated with volume dilatation. On the other hand, a significant volume increase is observed when crazes form [22]. Crazing is a localized yield behaviour which arises mostly in amorphous phases. When semicrystalline polymers are

subjected to a tensile stress, microvoids nucleate at a critical strain [17]. Thus, this yielding process is dilatational due to the void formation. Microvoids form between fibrils, elongated molecules, and eventually lead to crack. Crazes usually grow perpendicular to the maximum principal stress [23] in tensile stress states. The craze growth is controlled by either chain scission or chain disentanglement mechanisms [24].

Which yielding mechanism that dominates depends on the molecular structure, the stress state, the strain rate and the temperature. Stress-state dependent behaviour indicates pressure sensitivity, unlike many metallic materials, whose yield is not affected by hydrostatic components.

Describing the mechanical response of polymers is not complete without discussing the temperature effect. Both deformation and fracture are affected by molecular mobility which strongly depends on the temperature. The glass transition temperature of the material is a reference temperature that is related to the ductile-brittle transition.

2.3 The injection moulding process

2.3.1 The process and applications

Many plastic products are manufactured by injection moulding. Injection moulding is a conceptually simple process that allows the manufacture of cheap and durable plastic parts with relatively few constraints on shape, size and complexity. Some advantages of injection moulding are high production rates, repeatable high tolerances, the ability to use a wide range of materials, and little need to finish parts after moulding. Some disadvantages of this process are high investments (mould, machine), and the need to design mouldable parts [10, 25, 26].

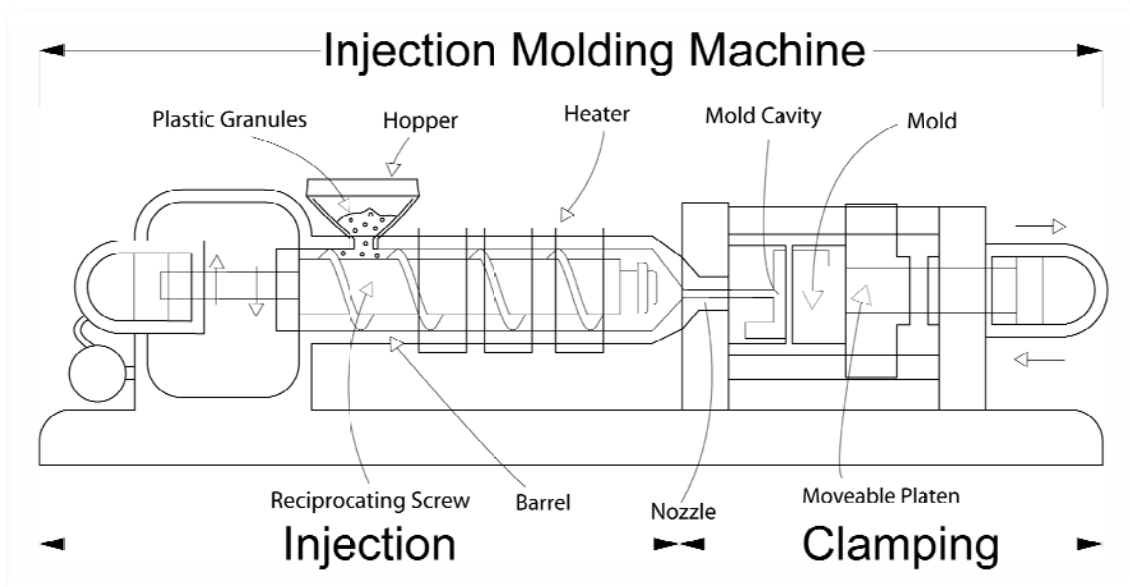


Figure 7 Schematic representation of injection moulding machine. Created by Brendan Rockey (used with permission of the creator). Source: Wikipedia.

The injection moulding process can be divided into different stages, as follows, see Figure 7.

Melting/plasticization and metering: Melting the plastics granules is achieved by two sources of energy, shear heating and external electric heaters. Shear heating arises owing to the high friction resistance which exists when molecular chain segments deform. When plastic granules are forced by the rotating screw the mechanical work converts to heat. The rotation of the screw and the screw design, are important for obtaining a melt with homogeneous temperature homogeneous mixing of the melt. The second source of energy consists of electrical heaters that surround the barrel and the nozzle. These heaters are controlled by the machine to keep the right temperature.

Injection: After obtaining a shot volume with rather homogeneous temperature, the melt is pushed from the screw chamber through the nozzle into the mould. The injection rate depends on the part geometry and the polymer material.

Holding pressure and cooling: After injection, the solidifying material is still pressurised (by the screw) so that the shrinkage during solidification is compensated for by a (small) flow of additional melt into the mould. This is called the holding pressure stage. The physical properties (mechanical, surface quality etc) of the final part can be improved dramatically by applying the right holding pressure. After the flow into the mould has stopped, the part must be cooled until it is stiff enough to be ejected from the mould. For medium to thick parts, the cooling stage may be the longest part of the injection moulding cycle.

Ejection: The last step is when the solidified part is removed (usually ejected) from the mould. The ejection system is a mechanical system with pins that push the part out of the mold.

2.3.2 Process-induced features and defects

The molecular structure of injection-moulded plastics may have some special features, and the details depend on the material, the processing conditions and the part geometry. Typically, a heterogeneous and anisotropic microstructure develops due to the high shear rates and the temporal and spatial variations in thermo-mechanical history [27]. High shear rates and rapid cooling in the region close to the mould surface lead to a highly oriented low-crystallinity microstructure. The anisotropy induced by the shear stress during the injection process is a dominant molecular or crystalline orientation in the flow direction [28]. The morphology gradually changes from the skin to the core, where a spherulitic structure with a high degree of crystallinity is typically observed. A typical skin-core structure for injection-moulded polypropylene is shown in Figure 8. Melt and mould temperatures, injection speed and holding pressure are the main parameters affecting these process-induced features.

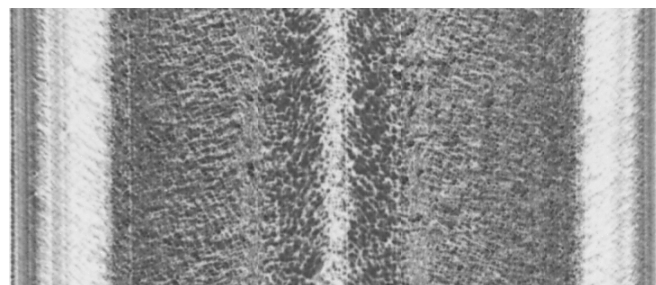


Figure 8 Skin-core structure of injection moulded polypropylene. Polarized optical microscopy was measured by Odny Debernard at SINTEF (used with permission).

A defect that can be caused by the part geometry is weld lines [29]. These are generally caused by holes or inserts in the part, multiple gates or jetting stream. Weld lines are considered as weak zones in moulded parts and they have a considerable effect on mechanical properties. In most commercial products it is almost impossible to avoid weld lines, although their performances can be improved by processing conditions.

Thermoplastic materials have a relatively high coefficient of thermal expansion because of highly temperature-dependent secondary bonds of molecular chain segments. Crystalline and semi-crystalline polymers in particular shrink considerably during solidification, to form a more ordered and compact structure. Structural imperfections such as voids and warping are related to the shrinkage. The holding pressure in the injection moulding process (see Sect. 2.3.1) is a key parameter in order to prevent/reduce the formation of such imperfections.

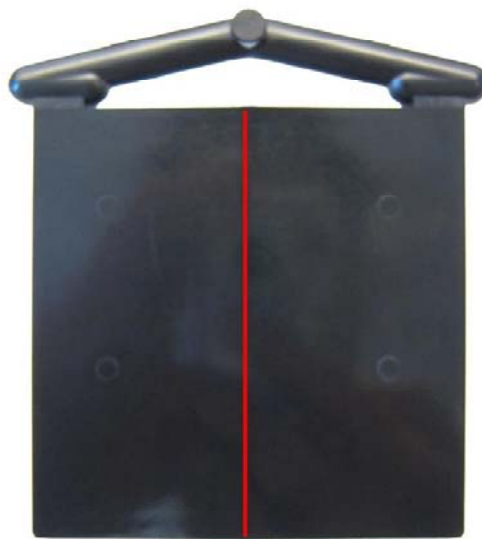


Figure 9 Injection moulded part with weld-line (indicated by the solid red line) induced by multiple gates.

2.4 Numerical simulation of the mechanical response

Because of the complex nature of semi-crystalline polymers, predicting their mechanical behaviour is not as straightforward as for some other materials. In addition, additives (rubber particles, filler particles etc) and processing-induced structures increase the complexity. The main features in the mechanical behaviour of semi-crystalline polymers are summarised in Table 1. Mechanical behaviour in relation to all these factors has been the subject of many studies since the 1980s.

Increasing interest in predicting the mechanical response has seen the emergence of several constitutive models. Two main categories can be mentioned: Phenomenological models and models with a basis in polymer physics. The phenomenological models are based on a macromechanical description, owing to the difficulty of describing the observations by established theories. Conversely, models based on polymer physics relate the macromechanical response to micromechanical responses and describe interactions at the micro level (not necessarily the molecular level).

The next step after choosing the material model is the calibration. It consists of two phases, performing the experiment and extracting the parameters. Usually the number of experiments for polymeric materials is high. Stress state, temperature, strain rate and damage can vary depending on the application. Extracting the parameters for the constitutive model can be a challenge, especially when one is dealing with models based on polymer physics. In such material models the molecular interactions are often represented by mechanical elements. Special techniques may be applied in order to define physical parameters at the *micro level* by material testing at the *macro level*. Phenomenological constitutive models, since they are on the same scale as the experiments, are usually easier to calibrate, but still may not be measurable directly by experiments. The main features summarized in Table 1 should be considered in the constitutive models.

Table 1 The main features of mechanical behaviour of injection-moulded modified polypropylene

Features	Comments
Heterogeneity	Skin-core morphology, and variation in morphology along the flow path.
Anisotropy	Orientation of polymer chains and crystals induced by the injection-moulding process
Viscoelasticity	Strain rate dependent modulus. Mostly controlled by the amorphous phase.
Stress state dependent elasticity	Often just referred to as pressure dependent modulus.
Viscoplasticity	Strain rate dependent yield stress.
Stress state dependent yield stress and hardening curve	Often just referred to as pressure dependent yield stress. The hardening curve can also depend on the stress state. Related to the pressure dependent free volume and molecular motion.
Plastic dilatation	I.e. a plastic Poisson's ratio < 0.5 . A characteristic of crazing.
Damage	
Temperature dependence	Related to the free volume and molecular motion. Properties of polymer materials have relatively high temperature sensitivity.

Due to the increasing demand for understanding and predicting the mechanical response of thermoplastic polymer materials, several constitutive models for these materials have been developed and reported in the literature. Table 2 summarizes some of the material models for polypropylene which have been implemented in finite element codes.

G'Sell and Jonas proposed a phenomenological model [30] for PVC and HDPE. Initially this model considered independent contributions of strain and strain rate. Later on it was modified for viscoelastic, temperature and strain hardening effect [31, 32]. The mechanical response of polypropylene materials under complex loading condition [33, 34] and the impact response [35] was modelled based on this constitutive law. Hizoum et al. reported another phenomenological model [36] based on earlier work by Oshmyan et al. [37]. They simulated the strain rate dependency and unloading behaviour of semi-crystalline polymers (HDPE and PP) by considering strain-induced evolution of material structure. For small strains, improved predictions were obtained with this model

Several models based on microstructural descriptions have also been developed. The competition between molecular orientation processes and molecular relaxation processes was modelled by Boyce et al. [38] in order to account for the rate and temperature behaviour of PET. Polanco-Loria et al. [39] developed a material model, inspired of Boyce's model, to predict the impact response of thermoplastics. This model was examined for a polypropylene material. Another physical model was proposed by Wang and Arruda [40]. This was a relatively complex model with "a quantitative rate-dependent Young's modulus, a nonlinear viscoelastic response between initial linear elastic response and yield due to inherent microstructural irregularity, rate and temperature dependent yield with two distinctive yield mechanisms for low and high strain rates, temperature-dependent strain hardening, plastic deformation of crystalline regions, and adiabatic heating" [40]. Drozdov and Gupta also derived a viscoelastic-viscoplastic constitutive model for isotactic polypropylene [41]. This model was based on molecular interactions, valid for small strains.

Table 2 Summary of selected polypropylene material models in the literature. Considered features are marked by a cross.

Articles	Features							Calibration tests	Materials (information given in the papers)	Validation tests
	Software	Viscoelasticity	Viscoplasticity	Stress state dependent yield stress and hardening curve	Plastic dilatation	Damage/ unloading	Temperature			
Wang and Arruda [40]		X	X	X	X		X	<ul style="list-style-type: none"> • Compression <ul style="list-style-type: none"> • Low strain rate • High strain rate 	Blend of PP, EPDM, and HDPE. The total elastomeric content is 15 wt % [40]	<ul style="list-style-type: none"> • Plane strain compression
Temimi-Maaref [34]	ABAQUS		X	X	X	X		<ul style="list-style-type: none"> • Tensile <ul style="list-style-type: none"> • Different strain rates • Loading-unloading • Compression • Shear 	Polypropylene copolymer compounded with 20% mineral fillers [34]	<ul style="list-style-type: none"> • Tensile • Compression • Shear
Kolling et. al (SAMP-1) [42-44]	LS-DYNA		X	X	X	X		<ul style="list-style-type: none"> • Tensile <ul style="list-style-type: none"> • Different strain rates • Loading-unloading • Compression • Shear 	PP-T10 (bumper) [45]	<ul style="list-style-type: none"> • Impact on automotive exterior parts
Dean and Crocker [46, 47]	ABAQUS		X	X	X			<ul style="list-style-type: none"> • Tensile <ul style="list-style-type: none"> • High strain rates • Compression • Shear 	Rubber toughened, propylene-ethylene copolymer containing talc filler [46, 48-51]	<ul style="list-style-type: none"> • Impact on automotive interior parts

Polanco-Loria et al. [39, 52]	LS-DYNA		X	X	X			<ul style="list-style-type: none"> • Tensile <ul style="list-style-type: none"> • Different strain rates • Compression 	Mineral and elastomer modified polypropylene (PP) [39]	<ul style="list-style-type: none"> • Plate impact test • Three point bending
Zrida et al. [53]	HEREZH++	X			X	X		<ul style="list-style-type: none"> • Tensile <ul style="list-style-type: none"> • Different strain rates • Loading-unloading • Relaxation 	Three heterophasic polypropylene copolymers containing talc and ethylene [53]	<ul style="list-style-type: none"> • Tensile <ul style="list-style-type: none"> • Loading-unloading • Two-step loading-relaxation • Torsion
Viana et al. [33, 35]	FORGE 2		X				X	<ul style="list-style-type: none"> • Tensile <ul style="list-style-type: none"> • Low strain rates 	Propylene copolymer [35]	<ul style="list-style-type: none"> • Plate impact test
Ma et al. [54]	ABAQUS		X				X	<ul style="list-style-type: none"> • Tensile <ul style="list-style-type: none"> • Different strain rates • Different temperatures 	TPO composite with 57.5 wt.% PP homopolymer, 20 wt.% ethylene octane rubber and 22.5 wt.% fine particle size talc [54]	<ul style="list-style-type: none"> • Tensile <ul style="list-style-type: none"> • Necking and neck propagation

3 Materials and methodologies in this thesis

3.1 Materials and processing

The main material in this study is a mineral (talc) and elastomer modified polypropylene compound for automotive exterior part. The talc content is ca 20 wt%, so this material is referred to as PP20 in the thesis. Some selected properties from the material data sheets are given in Table 3. Note that unnotched specimens of PP20 do not break in Charpy impact tests (ISO 179/1eU) at -20 °C and 23 °C. PP20 has a melting point at 163 °C (injection-moulded plate characterised by differential scanning calorimetry, peak of endotherm during first heating, 10 K/min). In the shear test study a similar PP with 40 wt% talc (referred to as PP40) and a polypropylene homopolymer (PPH) was also used. PPH specimens were machined from extruded plates (PP DWU AlphaPlus from Simona).

Dogbones (type 1A of ISO 527-2) and plates of PP20 and PP40 were manufactured injection moulding. Plates with thicknesses of 2.0, 2.4, 2.9, 3.3 and 3.9 mm were injection moulded using fan-gated cavities with polished surfaces. All plates measured 60×60 mm² except the 3.9 mm thick plates which measured 80×80 mm². The injection moulding conditions were based on the standard ISO 1873-2:2007 [55]. The mould temperature was 40 °C, the melt temperature was 200 °C and the holding pressure profile was optimised for each plate thickness (maximum holding pressure in the range 30-40 MPa). The flow front speed was the same for all plates (0.2 m/s). Hence, the shear rate differed between the plates (higher in thinner plates). Thermal effects (slower cooling inside a thicker plate) could also give rise to different morphological distributions in thin and thick plates.

Mould inserts, as seen in Figure 11, were used to make plates with weld lines (Figure 9) and plates with textured surfaces. For the latter the mould insert was photoetched with one of the coarsest patterns used for unpainted bumper covers, see more details in paper 2.

The dogbone shape specimens (type 1A of the ISO 527-2:1993 standard [56]) were injection moulded with processing conditions based on ISO 294-1:1996 [57] and ISO 1873-2:2007 [55]. The injection moulding machine was a servo-electric Battenfeld EM 50/120 with maximum clamping force 500 kN and a 25 mm diameter general-purpose screw, see Figure 12 .

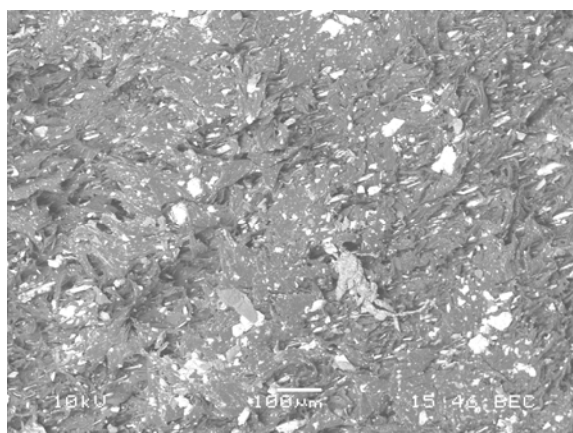


Figure 10 SEM photomicrograph (backscattered electron analysis) of the polypropylene blend containing 20 wt% talc (PP20). Talc particles are white in this micrograph.

Table 3 Selected properties for the materials in this thesis (mechanical properties at 23 °C).

	PP40	PP20	PPH
Melt flow rate (ISO 1133) (230 °C, 2.16 kg) [dg/min]	2	13	-
Density (ISO 1183) [kg/m ³]	1222	1050	915
Tensile modulus (ISO 527) (2 mm/min) [GPa]	3.8	1.4	1.7
Tensile stress at yield (ISO 527-2) (50 mm/min) [MPa]	31	16	33
Ratio of yield stress to modulus (both in tension)	8.2	11.4	19.4
Charpy impact strength, notched (ISO 179/1eA) [kJ/m ²]	5	58	9

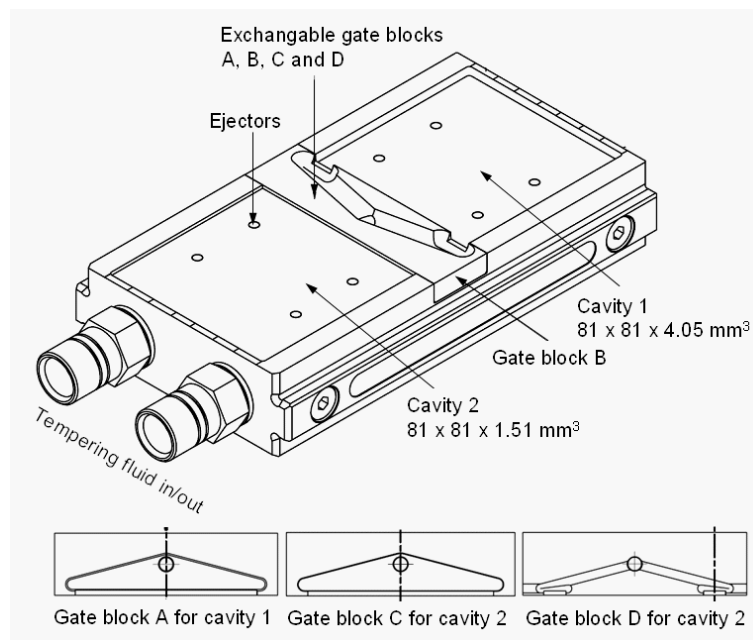


Figure 11 Exchangeable mould was used to make plates with and without weld-line and plates with textured surfaces



Figure 12 SINTEF's injection moulding machine. Battenfeld EM 50/120.

3.2 Numerical simulation

This thesis deals only with macro-scale simulations using a phenomenological model. All simulations were performed using LS-DYNA [58], a commercial nonlinear finite element analysis software package developed by LSTC. LS-DYNA is among the most well-known codes for impact and crash applications. It has both implicit and explicit solvers, and high flexibility in contact modelling. It supports a broad range of material models. Most material models were historically developed to describe metals, but recently a few models have been specially developed for polymeric materials and some of those are also available in the standard LS-DYNA version. The table below summarizes the most common material models which, depending on the application, can be used to simulate thermoplastic materials.

3.2.1 Material model

There is an increasing demand for more realistic numerical simulation of polymeric materials in the automotive industry. This thesis was defined in close relation with the industrial partner Plastal AS, which designs and produces plastic parts for automotive exteriors. Numerical simulation is an important tool in the design process. One of the important steps in the numerical simulation is to choose the appropriate material model. This material model should represent the important features of the desired material. The mode SAMP-1 was suggested by Plastal AS because of its claimed capability and its availability in LS-DYNA (Plastal AS uses LS-DYNA). SAMP-1 (Semi-Analytical Model for Polymers with C1-differentiable yield surface) [44] is specially developed for thermoplastic polymer materials [59]. Generally it is developed to be able to capture the different features of polymers. SAMP-1 is an elastic-viscoplastic material model with a quadratic or multi-linear yield surface [42]. The yield surface can be defined via up to four yield points, corresponding to biaxial tension, uniaxial tension, shear and uniaxial compression. The uniaxial tension yield stress vs. plastic strain is a mandatory input for this model, while the other input can be defined by the user upon the desired pressure dependency function. Von Mises, Drucker-Prager, quadratic and multi-linear yield behaviour can be implemented in the $p - \sigma_{vm}$ stress space, see Figure 13.

Table 4 The existing isotropic materials model for polymers in LS-DYNA [59].

Material Model	Features	Input
PIECEWISE_LINEAR_PLASTICITY	<ul style="list-style-type: none"> Linear elastic Von Mises plasticity Strain rate effect 	<ul style="list-style-type: none"> Tensile modulus Poisson's ratio Von Mises effective stress vs. effective plastic strain curve at different strain rate
PLASTICITY_POLYMER	<ul style="list-style-type: none"> Linear elastic Von Mises plasticity Strain rate effect 	<ul style="list-style-type: none"> Tensile modulus Poisson's ratio Von Mises effective stress vs. total effective strain curves at different strain rate
GEPLASTIC_SRATE_2000A	<ul style="list-style-type: none"> Linear elastic Pressure-dependent yield Strain rate effect Damage 	<ul style="list-style-type: none"> Tensile modulus Poisson's ratio Pressure sensitivity factor Yield stress vs. total effective strain in tension Strain rate parameter Unloading modulus as a function of plastic strain
PLASTICITY_COMPRESSION_TENSION	<ul style="list-style-type: none"> Viscoelastic Pressure-dependent yield Strain rate effect 	<ul style="list-style-type: none"> Tensile modulus Poisson's ratio Bulk modulus Shear relaxation modulus Shear decay constant Yield stress vs. effective plastic strain curve at different strain rate for compression and tension
SAMP-1	<ul style="list-style-type: none"> Linear elastic Pressure-dependent yield Strain rate effect Damage Volume dilation 	<ul style="list-style-type: none"> Tensile modulus Poisson's ratio Stress vs. plastic strain curve for tensile at different strain rate Stress vs. plastic strain curve for compression, shear and biaxial tension Damage parameter vs. plastic strain Plastic Poisson's ratio
POLYMER	<ul style="list-style-type: none"> Large elastic deformation (Neo-Hookean) Strain rate effect ($\dot{\epsilon}$) Hydrostatic stress effect Temperature effect (T) 	<ul style="list-style-type: none"> Tensile modulus Poisson's ratio Pre-exponential factor (correlates with initial flow stress, T and $\dot{\epsilon}$) Energy barrier to flow (correlates with initial flow stress, T and $\dot{\epsilon}$) Shear resistance in compression Shear resistance in tension Number of "rigid links" between entanglements Products (correlates with the initial hardening slope) Relaxation factor Absolute temperature

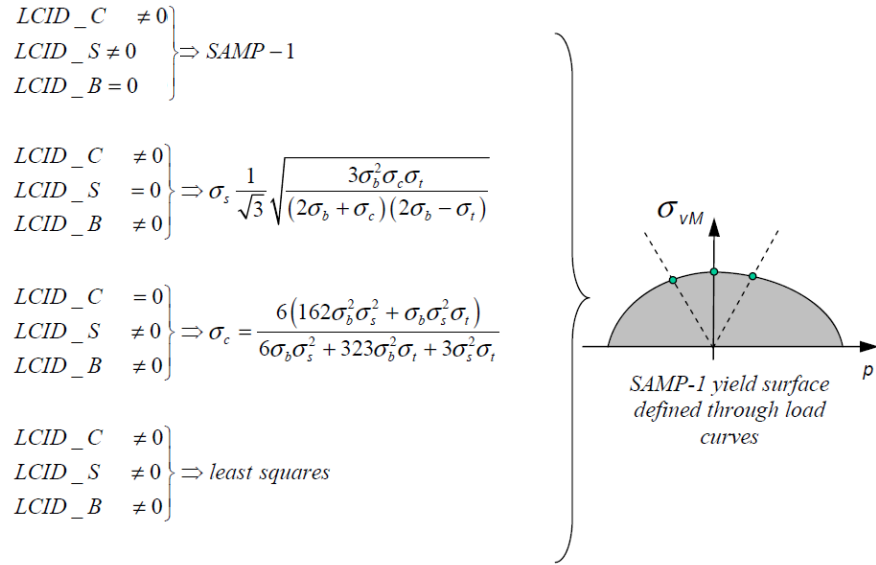


Figure 13 Generated yield surface in the stress invariant space by SAMP-1. LCID_C, LCID_S and LCID_B indicate the compression, shear and biaxial tension yield stress by assuming the tension yield stress always is defined. Source: LS-DYAN keyword user's manual V971/ Rev 5.

The pressure dependent yield surface is given by

$$f(p, \sigma_{vm}, \varepsilon_p) = \sigma_{vm}^2 - A_0 - A_1 p - A_2 p^2 \leq 0 \quad (1)$$

Where, σ_{vm} is the von-Mises equivalent stress, p is the pressure and A_0 , A_1 and A_2 are the constants derived from the yield stresses in different stress states [44].

The yield stresses in different stress states can be defined as a function of plastic strain. Therefore SAMP-1 will internally modify all input data to convert the plastic strain to the equivalent plastic strain.

The non-associated flow rule in SAMP-1 is based on the plastic potential which can be calibrated by α either as a constant or as a function of the equivalent plastic strain.

$$g = \sqrt{\sigma_{vm}^2 + \alpha p^2} \quad (2)$$

Where, α is the parameter used by SAMP-1 to define the plastic potential surface, see eq. 3. For materials with different flow behaviour in tension and compression a non-symmetrical flow surface can be accomplished by a different value for α in tension and compression. The input for the material model in LS-DYNA is the plastic Poisson's ratio:

$$\nu_p = \frac{9-2\alpha}{18+2\alpha} \quad (3)$$

Where, ν_p is the plastic Poisson's ratio and. A plastic flow potential surface based on $\nu_p = 0.5$ in compression and $\nu_p = 0.2$ in tension is shown in Figure 14. This flow potential leads to an isochoric deformation under compression and deformation with volume dilation under tensile stress.

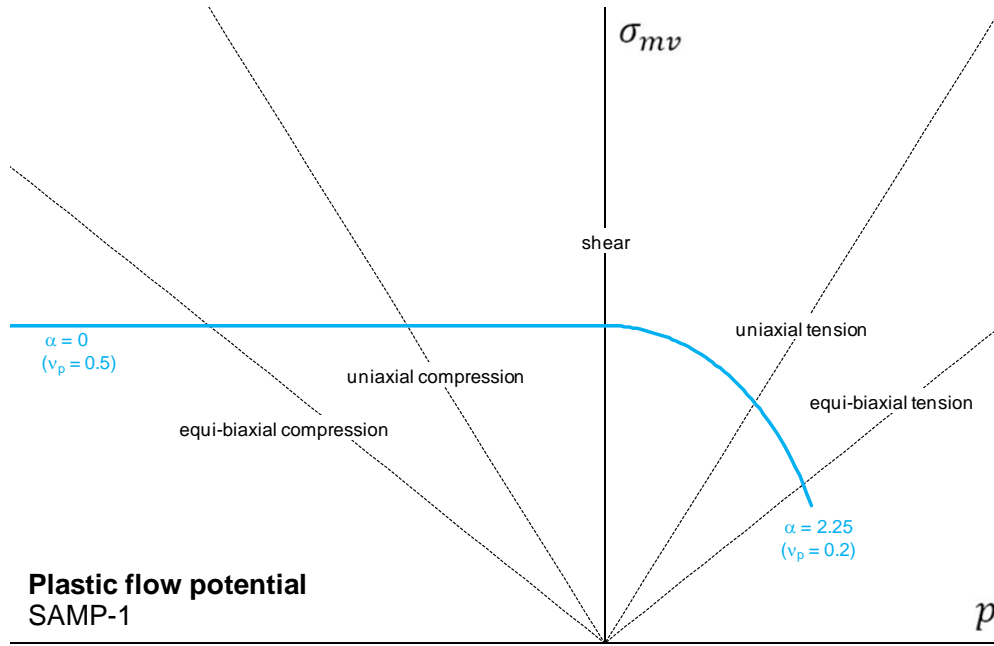


Figure 14 Non-symmetrical flow potential in the stress invariant space of SAMP-1.

Strain rate sensitivity is also among the features of the SAMP-1 for modelling the impact events. This option works via defining the strain rate sensitivity in uniaxial tension. The same strain rate sensitivity is used for the other stress state and there is no option for the rate sensitivity as function of triaxiality [44].

Unloading of polymeric materials is a challenge for numerical simulations. By increasing the plastic strain in thermoplastic polymers, the elastic modulus decreases due to damage evolution. Continuum damage models [60] can be calibrated based on uniaxial tensile loading-unloading tests to different plastic strains, see eq. (2). In SAMP-1 a simple damage parameter is defined vs. plastic strain:

$$d = 1 - \frac{E_{eff}}{E_0} \quad (4)$$

where E_{eff} and E_0 are the tensile moduli of the damaged and undamaged material, respectively. The net stress will be:

$$\sigma^{net} = \frac{\sigma}{1-d} \quad (5)$$

SAMP-1 is available in the explicit solver in LS-DYNA. It utilises the explicit cutting plane algorithm [61] for stress updating.

We can summarize SAMP-1 as an elastic-viscoplastic model with

- Strain rate dependent yield stress (i.e. viscoplastic)
- Pressure dependent yield surface

- Non-associated flow rule
- Volume dilation during the plastic deformation
- Effect of the damage for unloading events

Also, SAMP-1 assumes

- No visco-elasticity
- Same elastic behaviour for all stress states
- Same rate effect for all stress states
- No effect of stress state on the damage evolution

3.3 Calibration procedure

The calibration procedure is described below. It is based on data from tests in uniaxial tension, uniaxial compression and shear. Therefore based on three yield stresses a quadratic yield surface (eq. 1) was calibrated and studied.

Tensile tests were performed up to high strain rates, while compression and shear tests were quasi-static. In order to obtain the true stress-strain behaviour, digital image correlation (DIC) was used. More details about the experiments can be found in the experimental section (3.4.2) and in paper 1. A schematic chart of the calibration procedure is shown in Figure 14.

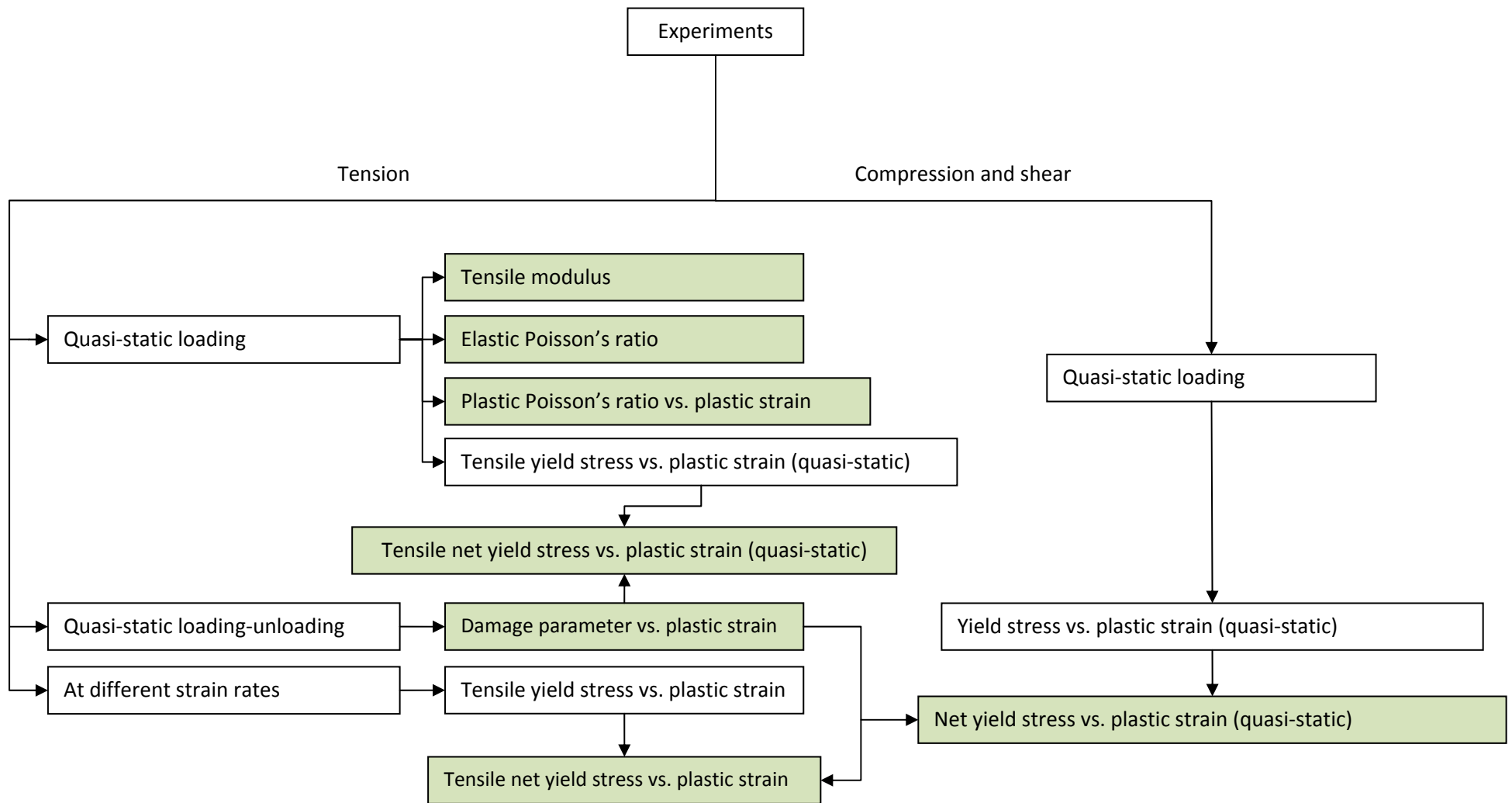


Figure 15 Schematic chart of the calibration procedure of SAMP-1. The green boxes indicate the input for the model.

3.4 Mechanical testing

In this section a brief explanation of the mechanical testing is presented. Having reliable experimental results is essential to understanding the nature of the behaviour. Experimental mechanics is in close connection with other areas such as optics and electronics which can improve the results dramatically. However, the hardware limitation is not the only challenge in this subject. Examining the material under constant strain rate and/or a particular stress state needs special consideration. Advanced measuring techniques can be used in order to reduce the number of assumptions. Two sets of mechanical testing were performed. The first set dealt with material behaviour in the different stress states in order to obtain input data for model calibration. The second tests series was performed in order to study the material performance and to validate the material model under combined stress states as well as different strain rates.

3.4.1 Digital Image Correlation (DIC)

DIC is a non-contact strain measurement method which can follow the displacement of deformable or rigid objects. This technique consists of capturing consecutive images with a digital camera during the deformation period to evaluate the change in surface characteristics of the specimen while it is subject to incremental loads [62]. To apply this method, the specimen needs to be prepared by applying a random dot pattern (speckle pattern) to its surface.

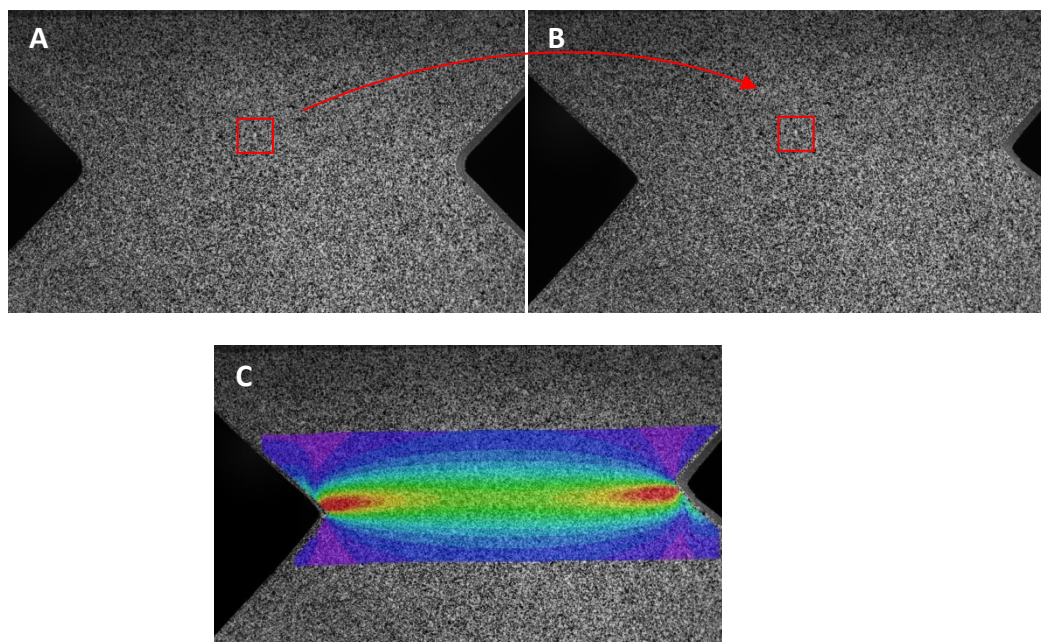


Figure 16 The method tracks the speckle pattern in small neighbourhoods (subset). A) Before deformation. B) After deformation. C) Measured shear strain field on a test specimen subjected to the shear (paper 4).

3.4.2 Providing input to numerical simulations

3.4.2.1 Uniaxial tension

The tensile test is the most common experiment to define a material's mechanical performance. This test is performed on a universal testing machine as shown in Figure 16. There are two classes of testing machines, electromechanical and hydraulic. In general, a hydraulic machine is capable of carrying higher forces at higher test speeds, while an electromechanical testing machine is more accurate for controlling the position and speed. A dogbone shaped specimen has been suggested by the standard [63] in order to avoid the stress concentration near the grips. In this study the test specimens were fabricated either directly by the injection moulding or by machining from plates. A Charly CNC machine was used to cut dogbone shape specimens and a 2.0 mm diameter double-tooth milling tool was employed.



Figure 16 Zwick Z250 electromechanical universal testing machine at SINTEF

High-speed servohydraulic testing machines are now available in many labs. Commercial machines have cross-head speeds up to 25 m/s, and special fixtures and force measuring solutions. However, testing and data analysis is not trivial. Ductile polymers (large strains) with low yield stress are challenging. At high loading rates, dynamic effects lead to oscillations in the recorded force. Furthermore, strains cannot be measured with conventional extensometers. Contact-less optical techniques, such as digital image correlation (mentioned in Sect. 3.4.1), can be used to obtain the true stress-strain response.

The high-speed tensile tests were performed with a modified servohydraulic Schenk/Instron VHS machine. This machine has a maximum cross-head speed of 10 m/s. Most of the high-speed data in this thesis were measured earlier (with the same material and in the same laboratory) [64]. True stress-strain responses were obtained by using a high-speed digital camera and 2D digital image correlation.

3.4.2.2 Uniaxial compression

The compression tests were partly based on the standard ISO 607 [65]. Specimens with two different dimensions, $4 \times 10 \times 10 \text{ mm}^3$ and $4 \times 4 \times 4 \text{ mm}^3$, were studied. The test specimens were machined from injection-moulded plates or dogbones, using a 2.0 mm diameter double-tooth milling tool. The last of the dimensions given above was parallel to the loading direction, and parallel to the flow direction in the injection-moulded parts. A combination of PTFE tape and soap water [66] was used in order to reduce the barreling effect, due to friction in contact with the compression plates, for the specimens with aspect ratio 1. At 50% compression, specimens from dogbones barreled considerably (Figure 17a), but not those from plates (Figure 17b). Hence, the latter were used for the calibration tests. Making samples from this soft material can be a challenge, especially when it comes to small dimensions. 3D digital image correlation (DIC) was used to obtain the true strain and the true cross-section (Figure 18).



Figure 17 Barreling behaviour of lubricated test specimens with original dimensions $4 \times 4 \times 4 \text{ mm}^3$ for a nominal strain of 50% (pictures after unloading). The specimens were machined from a dogbone (a) and a plate (b), respectively. In the pictures, the compression loading is vertical (and along the flow direction of the injection-moulded parts), and the as-moulded surfaces are vertical and into the paper plane.

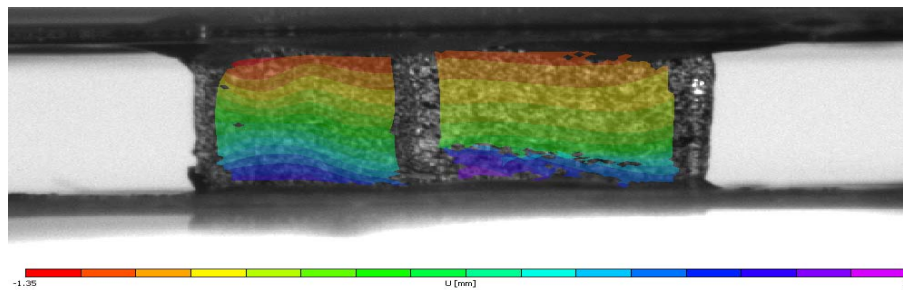


Figure 18 3D DIC measurement of vertical displacements of a $4 \times 4 \times 4 \text{ mm}^3$ test specimen at ca 50% compressive strain. This specimen was machined from a plate, as the specimen in Figure 17b.

3.4.2.3 Shear

The V-Notched-Rail test and the Iosipescu test are common in-plane shear tests. Both methods are using a butterfly shape specimen which was machined from plates in this case. Test specimens were machined according to ASTM standards (see paper 4), either from 3.9 mm thick injection moulded plates or 4.0 mm thick extruded plates. To assess the effect of the notch root radius, specimens with notch root radius 0.65 mm, 1.3 mm and 2.6 mm were prepared. Depending on the notch root radius, 1.3 mm or 2.0 mm diameter double-tooth milling tools were used. The shear test fixtures were mounted in a universal test machine fitted with a 5 kN load cell. Effects of strain distribution, strain rate, geometry and failure on the shear response was investigated by applying 3D digital image correlation. Details can be found in paper 4.

3.4.3 Material performance and verification tests

3.4.3.1 Instrumented falling-weight impact

Most verification tests were performed with an instrumented falling-weight impact tester, see Figure 19. Piezoelectric force transducers with maximum load 20 kN and 2.5 kN were used (Kistler 9331B and 9301B). Some tests were also done with constant cross-head velocity on a servo-hydraulic test machine.

The drop mass was 3.5 kg in all falling-weight impact tests. Tests were performed at 20 °C, as well as -30 °C and some lower temperatures. The plates were pneumatically clamped by a serrated ring with inner diameter 40 mm. The clamping force was 3 kN. A hemispherical \varnothing 20 mm striker was used in most of the tests reported in paper 1 and paper 2. The striker was lubricated with silicone grease in order to avoid some of the scatter and complexities associated with friction effects. However, note that the lubrication has a significant effect on the force-deflection curves, especially for ductile plates and large deflections.



Figure 19 The instrumented falling-weight impact tester used in this thesis (Rosand type 4, modified by Imatek).

Three-point bending of bars (falling-weight impact) was performed with the same machine. Bars with cross-section $4 \times 10 \text{ mm}^2$ and length 80 mm were tested oriented flatwise or edgewise. The adjustable span was set to 60 mm and the impact speeds were in the range 1–4 m/s. The drop weight was 3.5 kg.

Force oscillations is a problem in impact tests. The oscillations are reduced when moving the force sensor closer to the specimen, thereby shortening the ‘load train’ and reducing the number of interfaces at which elastic stress waves are partly reflected. The material and the design of the ‘load train’ including the force sensor also play a role, and the system is usually designed to have a natural frequency far above that of the test specimen. In order to improve the force signal, we have made some modifications to the striker for three-point bending (and Charpy impact testing) in our

instrumented falling-weight impact tester (Rosand/Imatek Type 4). Placing the force sensor close to the contact point between the specimen and the striker head gives the most substantial improvement [67], see Figure 20.

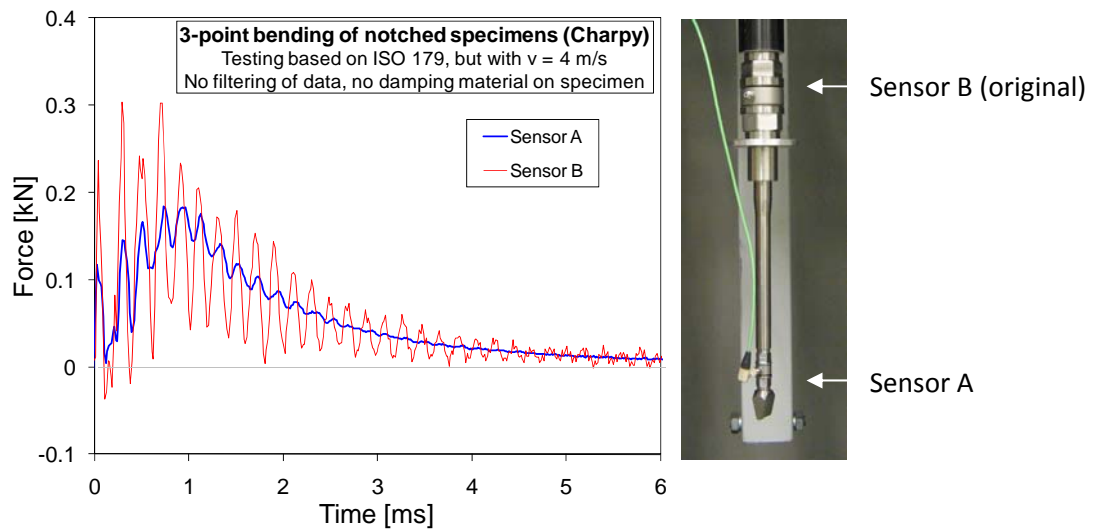


Figure 20 Reduced dynamic effects (force oscillations) for falling-weight impact tests.

4 Concluding remarks

The mechanical response of polypropylene materials was investigated experimentally as well as numerically in this thesis. The material was a talc-filled and elastomer-modified polypropylene developed for injection-moulded automotive exterior parts. The mechanical response of thermoplastic polymer materials is strongly related to their microstructure. The microstructure is also affected by fabrication, e.g. injection moulding, and the processing conditions. The anisotropy and inhomogeneity of injection moulded parts can be a challenge trying to predict their mechanical response. Due to the complexity of the molecular and composite structure of these polypropylene compounds, making an accurate simulation requires highly well-defined material models. It means the material model should be able to describe the most important features of the material behaviour, e.g. strain rate and pressure dependency, damage evolution, and plastic dilatation. Some of the challenges are related to the calibration testing in well-defined stress states, some are related to the heterogeneity and anisotropy of the injection-moulded parts, and some are related to shortcomings of the model. It should be noted, however, that with this rather complex material behaviour it is often difficult to separate the effects. Using an advanced material model needs more experiments for calibration. From an experimental point of view, performing material performance tests is not straightforward for all stress states. However, experimental mechanics is growing fast and the bridges between mechanics, electronics and optics make it possible to obtain more reliable and intrinsic material parameters. Using recently developed material models for polymeric materials, in combination with a number of experiments, can improve the predictions significantly. Moreover, there are still many unresolved issues, related to experiments and models, which should be investigated in order to understand the nature of the material behaviour and consequently improve the numerical predictions.

Bibliography

- [1] J. Karger-Kocsis (Ed.) Polypropylene - An A-Z Reference, Springer - Verlag, 1999.
- [2] N. Pasquini (Ed.) Polypropylene handbook, Hanser Gardner Pubns, 2005.
- [3] J. Karger-Kocsis (Ed.) Polypropylene: Structure, Blends and Composites; Structure and Morphology, Chapman & Hall, 1995.
- [4] J. Karger-Kocsis (Ed.) Polypropylene: Structure, Blends and Composites; Copolymers and blends, Chapman & Hall, 1995.
- [5] H.G. Karian (Ed.) Handbook of polypropylene and polypropylene composites, CRC, 2003.
- [6] S. Albus, World Market Special – Polypropylene Part 1, Kunststoffe international, 10 (2010) 61-63.
- [7] Plastics – the Facts 2010 – An analysis of European plastics production, demand and recovery for 2009, (2010).
- [8] S. Albus, World Market Special – Polypropylene Part 2, Kunststoffe international, 10 (2010) 64-67.
- [9] C. Zhang, Y. Shangguan, R. Chen, Y. Wu, F. Chen, Q. Zheng, G. Hu, Morphology, microstructure and compatibility of impact polypropylene copolymer, Polymer, 51 (2010) 4969-4977.
- [10] A. Birley, B. Haworth, J. Batchelor, Physics of Plastics: Processing, Properties, and Materials Engineering, Hanser, 1991.
- [11] F. van der Burgt, Crystallization of Isotactic Polypropylene: The Influence of Stereo-defects, Ph.D., Technische Universiteit Eindhoven, (2002).
- [12] J. Karger-Kocsis, S. Fakirov, Nano-and micro-mechanics of polymer blends and composites, Hanser Verlag, 2009.
- [13] S. Díez-Gutiérrez, M.A. Rodríguez-Pérez, J.A.D. Saja, J.I. Velasco, Heterogeneity and anisotropy of injection-molded discs of polypropylene and polypropylene composites, J. Appl. Polym. Sci., 77 (2000) 1275-1283.
- [14] E. Ferrage, F. Martin, A. Boudet, S. Petit, G. Fourty, F. Jouffret, P. Micoud, P. De Parseval, S. Salvi, C. Bourgerette, J. Ferret, Y. Saint-Gerard, S. Buratto, J.P. Fortune, Talc as nucleating agent of polypropylene: morphology induced by lamellar particles addition and interface mineral-matrix modelization, J. Mater. Sci., 37 (2002) 1561-1573.
- [15] K.W.Y. Wong, R.W. Truss, Effect of flyash content and coupling agent on the mechanical properties of flyash-filled polypropylene, Compos. Sci. Technol., 52 (1994) 361-368.
- [16] B. Pukánszky, M. Es, F.H.J. Maurer, G. Vörös, Micromechanical deformations in particulate filled thermoplastics: volume strain measurements, J. Mater. Sci., 29 (1994) 2350-2358.
- [17] T.L. Anderson, Fracture Mechanics: Fundamentals and Applications, Third ed., CRC Press, 2005.
- [18] N. Kukaleva, M. Jollands, F. Cser, E. Kosior, Influence of phase structure on impact toughening of isotactic polypropylene by metallocene-catalyzed linear low-density polyethylene, J. Appl. Polym. Sci., 76 (2000) 1011-1018.
- [19] A. Collyer, Rubber toughened engineering plastics, Kluwer Academic Publishers, 1994.
- [20] W. Callister, Materials science and engineering: an introduction, 7th ed. ed., John Wiley & Sons, 2007.
- [21] P.B. Bowden, J.A. Jukes, The plastic flow of isotropic polymers, J. Mater. Sci., 7 (1972) 52-63.
- [22] C. G'Sell, S.-L. Bai, J.-M. Hiver, Polypropylene/polyamide 6/polyethylene-octene elastomer blends. Part 2: volume dilatation during plastic deformation under uniaxial tension, Polymer, 45 (2004) 5785-5792.
- [23] H.H. Kausch, R. Gensler, C. Grein, C.J.G. Plummer, P. Scaramuzzino, Crazing in semicrystalline thermoplastics, J. Macromol. Sci.-Phys., B38 (1999) 803-815.
- [24] L.L. Berger, On the mechanism of craze fibril breakdown in glassy polymers, Macromolecules, 23 (1990) 2926-2934.
- [25] T.A. Osswald, L.S. Turng, P.J. Gramann, Injection Molding Handbook, Carl Hanser Publishers, 2007.
- [26] V. Goodship, Practical guide to injection moulding, Rapra Technology, 2004.

- [27] J.C. Viana, Structural interpretation of the strain-rate, temperature and morphology dependence of the yield stress of injection molded semicrystalline polymers, *Polymer*, 46 (2005) 11773-11785.
- [28] X.F. Yu, H. Wu, J. Li, S.Y. Guo, J.H. Qiu, Structure and property of injection-molded polypropylene along the flow direction, *Polym. Eng. Sci.*, 49 (2009) 703-712.
- [29] A. Enikeev, Y. Kazankov, V. Mironov, Mechanism of weld line formation in injection molding of plastics, *Chemical and Petroleum Engineering*, 35 (1999) 118-123.
- [30] C. G'Sell, J. Jonas, Determination of the plastic behaviour of solid polymers at constant true strain rate, *J. Mater. Sci.*, 14 (1979) 583-591.
- [31] C. G'Sell, N.A. Aly-Helal, J.J. Jonas, Effect of stress triaxiality on neck propagation during the tensile stretching of solid polymers, *J. Mater. Sci.*, 18 (1983) 1731-1742.
- [32] Y. Tillier, Mechanical characterization of solid polymers using inverse analysis: application to high velocity and multiaxial tests, PhD thesis Sciences et Génie des Matériaux, CEMEF Centre de Mise en Forme des Matériaux (1998).
- [33] J.C. Viana, A.M. Cunha, N. Billon, Prediction of the tensile impact behavior of injection molded samples from quasi-static data, *Polym. Eng. Sci.*, 39 (1999) 1463-1472.
- [34] N. Temimi-Maaref, A. Burr, N. Billon, Damaging processes in polypropylene compound: Experiment and modeling, *Polym. Sci. Ser. A*, 50 (2008) 558-567.
- [35] J.C. Viana, A.M. Cunha, N. Billon, Experimental characterization and computational simulations of the impact behavior of injection-molded polymers, *Polym. Eng. Sci.*, 47 (2007) 337-346.
- [36] K. Hizoum, Y. Remond, N. Bahlouli, V. Oshmyan, S. Patlazhan, S. Ahzi, Non linear strain rate dependency and unloading behavior of semi-crystalline polymers, *Oil Gas Sci. Technol.*, 61 (2006) 743-749.
- [37] V. Oshmyan, S. Patlazhan, Y. Remond, Simulation of small-strain deformations of semi-crystalline polymer: Coupling of structural transformations with stress-strain response, *J. Mater. Sci.*, 39 (2004) 3577-3586.
- [38] M.C. Boyce, S. Socrate, P.G. Llana, Constitutive model for the finite deformation stress-strain behavior of poly(ethylene terephthalate) above the glass transition, *Polymer*, 41 (2000) 2183-2201.
- [39] M. Polanco-Loria, A.H. Clausen, T. Berstad, O.S. Hopperstad, Constitutive model for thermoplastics with structural applications, *Int. J. Impact Eng.*, 37 (2010) 1207-1219.
- [40] Y. Wang, E.M. Arruda, Constitutive modeling of a thermoplastic olefin over a broad range of strain rates, *Journal of Engineering Materials and Technology-Transactions of the ASME*, 128 (2006) 551-558.
- [41] A.D. Drozdov, R.K. Gupta, Non-linear viscoelasticity and viscoplasticity of isotactic polypropylene, *International Journal of Engineering Science*, 41 (2003) 2335-2361.
- [42] S. Kolling, A. Haufe, M. Feucht, P. Du Bois, A Constitutive Formulation for Polymers Subjected to High Strain Rates, in: 9th International LS-DAYA Users Conference, 2006.
- [43] S. Kolling, A. Haufe, A constitutive model for thermoplastic materials subjected to high strain rates, *Proceedings in Applied Mathematics and Mechanics*, 5 (2005) 303-304.
- [44] S. Kolling, A. Haufe, M. Feucht, P. Du Bois, SAMP-1: A Semi-Analytical Model for the Simulation of Polymers, in: *LS-DYNA Anwenderforum*, 2005, pp. 26.
- [45] P. Du Bois, S. Kolling, M. Feucht, A. Haufe, The Influence of Permanent Volumetric Deformation on the Reduction of the Load Bearing Capability of Plastic Components, in: 10th International LS-DYNA Users Conference, USA, 2008.
- [46] G. Dean, L. Crocker, Prediction of impact performance of plastics mouldings. Part 1: Material models and determination of properties, *Plast. Rubber Compos.*, 36 (2007) 1-13.
- [47] L. Crocker, G. Dean, Prediction of impact performance of plastics mouldings, part 2: Finite element simulations, *Plast. Rubber Compos.*, 36 (2007) 14-25.
- [48] G. Dean, L. Crocker, Prediction of the impact performance of plastics using finite element methods, in: *Measurement Good Practice Guide No 87*, National Physical Laboratory, UK, 2006.

- [49] G. Dean, B. Read, Modelling the behaviour of plastics for design under impact, *Polym. Test.*, 20 (2001) 677-683.
- [50] G. Dean, L. Wright, An evaluation of the use of finite element analysis for predicting the deformation of plastics under impact loading, *Polym. Test.*, 22 (2003) 625-631.
- [51] G.D. Dean, L.E. Crocker, Prediction of the impact performance of plastics mouldings, NPL report DEPC-MPR-043, (2006).
- [52] M. Polanco-Loria, A.H. Clausen, T. Berstad, O.S. Hopperstad, A constitutive model for thermoplastics intended for structural applications, in: 7th European LS-DYNA Conference, Austria, 2009.
- [53] M. Zrida, H. Laurent, G. Rio, S. Pimbert, V. Grolleau, N. Masmoudi, C. Bradai, Experimental and numerical study of polypropylene behavior using an hyper-visco-hysteresis constitutive law, *Comp. Mater. Sci.*, 45 (2009) 516-527.
- [54] Q. Ma, X. Su, X. Lai, J. Lasecki, R. Frisch, Modeling and simulation of the large deformation behavior for thermoplastic olefin, *Comp. Mater. Sci.*, 47 (2010) 660-667.
- [55] ISO, 1873-2, Plastics - Polypropylene (PP) moulding and extrusion materials - Part 2: Preparation of test specimens and determination of properties, 2007
- [56] ISO, 527-2, Plastics - Determination of tensile properties - Part 2: Test conditions for moulding and extrusion plastics, 1993
- [57] ISO, 294-1, Plastics - Injection moulding of test specimens of thermoplastic materials - Part 1: General principles, and moulding of multipurpose and bar test specimens, 1996
- [58] <http://www.lstc.com/>
- [59] LS-DYNA KEYWORD USER's MANUAL 971 R4 beta (2009).
- [60] J. Lemaitre, A course on damage mechanics, Springer-Verlag, Berlin, 1992.
- [61] J.C. Simo, T.J.R. Hughes, Computational inelasticity, Springer Verlag, 1998.
- [62] R. Cintron, V. Saouma, Strain Measurements with the Digital Image Correlation System Vic-2D, in: CU-NEES-08-06, Center for Fast Hybrid Testing, University of Colorado, 2008.
- [63] ISO, 527, Plastics - Determination of tensile properties - Part 2: Test conditions for moulding and extrusion plastics, 1993
- [64] T. Glomsaker, E. Andreassen, M. Polanco-Loria, O. Lyngstad, R. Gaarder, E. Hinrichsen, Mechanical response of injection-moulded parts at high strain rates, in: PPS07ea (Polymer Processing Society), Gothenburg, Sweden, 2007.
- [65] ISO, 604, Plastics — Determination of compressive properties, 2002
- [66] B.A.G. Schrauwen, R.P.M. Janssen, L.E. Govaert, H.E.H. Meijer, Intrinsic deformation behavior of semicrystalline polymers, *Macromolecules*, 37 (2004) 6069-6078.
- [67] I. Horsfall, C.H. Watson, C.G. Chilese, A drop tower method for high rate fracture toughness testing of polymers, in: A.P. B.R.K. Blackman, J.G. Williams (Eds.) European Structural Integrity Society, Elsevier, 2003, pp. 221-229.

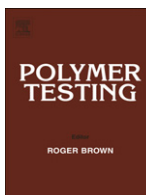
Part B
Papers

Paper 1

H. Daiyan, E. Andreassen, F. Grytten, O.V. Lyngstad, T. Luksepp, H. Osnes

Low-velocity impact response of injection-moulded polypropylene plates – Part 1: Effects of plate thickness, impact velocity and temperature

Polymer Testing, Volume 29, Issue 6, 2010



Material Performance

Low-velocity impact response of injection-moulded polypropylene plates – Part 1: Effects of plate thickness, impact velocity and temperature

H. Daiyan^a, E. Andreassen^{a,*}, F. Grytten^a, O.V. Lyngstad^{b,1}, T. Luksepp^{b,2}, H. Osnes^c

^aSINTEF, Box 124 Blindern, NO-0314 Oslo, Norway

^bPlastal AS, Box 94, NO-2831 Raufoss, Norway

^cDept. of Mathematics, University of Oslo, Box 1053 Blindern, NO-0316 Oslo, Norway

ARTICLE INFO

Article history:

Received 30 March 2010

Accepted 10 May 2010

Keywords:

Polypropylene

Impact

Plate

Low temperature

Fracture

ABSTRACT

The low-velocity, low-energy impact response of a mineral and elastomer modified polypropylene was characterised by instrumented falling-weight impact testing of plates with annular clamping. Different loading conditions were assessed by varying plate thickness (2–4 mm), incident impact velocity/energy (up to 4.4 ms⁻¹/34 J) and temperature (–60 to 20 °C). Force-deflection curves and fracture patterns were categorised and analysed. The main trends can be explained in terms of 1) deformations spanning from small-strain bending to large-strain stretching, 2) fracture responses spanning from linear-elastic brittle to highly ductile, 3) process-induced anisotropy, and 4) friction effects. With the highest impact velocity used in this study, plates thinner than ~2.5 mm fractured at both –30 and 20 °C, although with different mechanisms. A remarkable finding was that the central radial crack under the striker ran parallel to the (injection moulding) flow direction for the most brittle fractures (at low temperatures), while it ran perpendicular to the flow direction in other cases.

© 2010 Elsevier Ltd. All rights reserved.

1. Introduction

The impact resistance of thermoplastic polymer materials is important for many applications. The automotive industry and their suppliers are important driving forces in this field. The polypropylene (PP) compound studied in this paper is optimised for automotive exterior parts such as bumper covers (the bumper cover is the outer part of the bumper, with or without paint). A bumper cover must fulfil several demanding specifications. Some of these specifications are conflicting; in particular ductility vs. stiffness. Optimising the ductility-stiffness balance of PP compounds,

i.e. tailoring PP matrix, elastomers, nucleating agents and fillers (both separately and in combination), is still a major research topic [1–4]. PP compounds for exterior parts are specially modified to have enough ductility at low temperatures (down to –30 °C for some tests) in combination with requirements for high stiffness, low thermal expansion, high scratch resistance etc.

The study reported in this paper was initiated to improve the understanding of factors influencing the low-velocity, low-energy impact response, especially at low temperatures. In cold winter conditions, minor impacts on the bumper cover should not result in brittle fracture.

With a given polypropylene compound, the apparent brittleness of a bumper cover, when impacted with a striking object, is related to several coupled factors: 1) Loading conditions (temperature, velocity, energy, striker tip geometry). 2) Bumper cover details (thickness, paint, surface roughness, local constraints due to cover geometry and

* Corresponding author. Tel.: +47 98282492.

E-mail address: erik.andreassen@sintef.no (E. Andreassen).

¹ Present address: SINTEF Raufoss Manufacturing, Box 163, NO-2831 Raufoss, Norway.

² Present address: Norwegian Composite Center, Box 163, NO-2831 Raufoss, Norway.

assembly). 3) Injection moulding process (weld lines, inhomogeneity, anisotropy, residual stresses). This paper and a forthcoming paper [5] address some of these effects with an idealised test; out-of plane loading of plates with annular clamping. Note that with this test the fracture is in most cases initiated in a biaxial stress state (at the centre of the plate).

Another aim of this experimental study is to provide input for improving material models and data for numerical simulations, which will be addressed in a forthcoming paper. Current models for polymers have shortcomings when it comes to predicting unloading response (elastic rebound) and fracture [6,7].

Most of the experimental literature on the impact properties of PP and similar materials has focused on understanding the micromechanics and developing improved materials, and the experimental methods are either fracture mechanics tests (usually mode I) or standard impact tests of notched specimens (Charpy or Izod). Only a few PP studies have included out-of plane impact loading of (unnotched) plates (we will refer to these in the sections below) and, generally, the results are not analysed to the same degree as in some studies of metals and composites. Furthermore, many injection-moulded parts are subjected to out-of-plane loading, so this test is highly relevant for engineering purposes [8]. Finally, several studies on the numerical simulation of the impact response of polymer components have included out-of-plane loading as a verification case for the material models, mainly focusing on the loading up to maximum load. Issues such as friction between plate and striker [9–12], thermomechanical coupling [9–11,13], strain-hardening response [9,14], prediction of radial displacements [12] and failure criteria [10,11,13] have been considered in these studies. The loading of real injection-moulded components with similar strikers has also been simulated [15–17].

2. Experimental

2.1. Material and standard mechanical properties

The material in this study is a 20% mineral (talc) and elastomer modified polypropylene compound (ISO code PP+EPDM-TD20) for automotive exterior parts. This material was also used in an earlier study [18]. Some selected properties from the material data sheet are given in Table 1. Note that unnotched specimens of this material do not break in Charpy impact tests (ISO 179/1eU) at $-20\text{ }^{\circ}\text{C}$ and $23\text{ }^{\circ}\text{C}$. The material has a melting point at $163\text{ }^{\circ}\text{C}$ (injection-moulded plate characterised by differential scanning calorimetry, peak of endotherm during first heating, 10 K/min).

Note that the focus in this article is on the typical trends for this class of materials, not the details of this specific

material. Tests with a similar material from a different manufacturer showed similar results.

2.2. Preparation of test specimens

Plates with thicknesses of 2.0, 2.4, 2.9, 3.3 and 3.9 mm were injection-moulded using fan-gated cavities with polished surfaces, see Fig. 1. All plates measured $60 \times 60\text{ mm}^2$ and were used directly in the test, except the 3.9 mm thick plates which were milled to $\varnothing 60\text{ mm}$ plates from $80 \times 80\text{ mm}^2$ moulded plates.

The injection moulding conditions were based on the standard ISO 1873-2:2007. The mould temperature was $40\text{ }^{\circ}\text{C}$, the melt temperature was $200\text{ }^{\circ}\text{C}$ and the holding pressure profile was optimised for each plate thickness (maximum holding pressure in the range 30–40 MPa). The flow front speed was the same for all plates (0.2 m/s). Hence, the shear rate differed between the plates (higher in thinner plates). Thermal effects (slower cooling inside a thicker plate) could also give rise to different morphological distributions in thin and thick plates. The injection moulding machine was a servo-electric Battenfeld EM 50/120 with maximum clamping force 500 kN and a 25 mm diameter general-purpose screw. Plates with thickness 2.9 mm were not injection moulded in the authors' laboratory.

2.3. Mechanical testing

If nothing else is stated, the tests were performed with an instrumented falling-weight impact tester (Rosand type 4, modified by Imatek) fitted with a 20 kN piezoelectric force transducer (Kistler 9331B). Some tests were also done with constant test velocity using a servo-hydraulic test machine. The falling-weight impact test in this study is similar to the standard instrumented puncture impact test [19], but a lower drop mass was used, typical for low-energy impact tests in the automotive industry. The drop mass was 3.5 kg in all tests.

The plates were pneumatically clamped by a serrated ring with inner diameter 40 mm (Fig. 2). The clamping force was 3 kN. With this clamping ring and force, the part of the plate outside the clamped area was also slightly bent. As a consequence of this, 3.9 mm thick $80 \times 80\text{ mm}^2$ plates showed a slightly stiffer response than $\varnothing 60\text{ mm}$ plates with the same thickness, due to lower effective bending stiffness in the latter case. Only the latter results are reported in this paper.

A hemispherical $\varnothing 20\text{ mm}$ striker was used in the tests reported in the sections below. A ball striker was used in some tests to large deflections, since the standard hemispherical striker has two holes on the cylindrical section for the mounting bolt, and these holes may initiate a crack in some cases. The strikers were lubricated with silicone grease if nothing else is stated, in order to avoid some of the

Table 1
Selected material properties.

Melt flow rate (ISO 1133) ($230\text{ }^{\circ}\text{C}$, 2.16 kg) [dg/min]	Density (ISO 1183) [kg/m^3]	Flexural modulus (ISO 178) (2 mm/min) [GPa]	Tensile stress at yield (ISO 527-2) (50 mm/min) [MPa]	Flexural strength (ISO 178) [MPa]	Charpy impact strength, notched (ISO 179/1eA) at $T = -30, -20$ and $23\text{ }^{\circ}\text{C}$ [kJ/m^2]
13	1050	1.6	16	22	5, 6 and 58

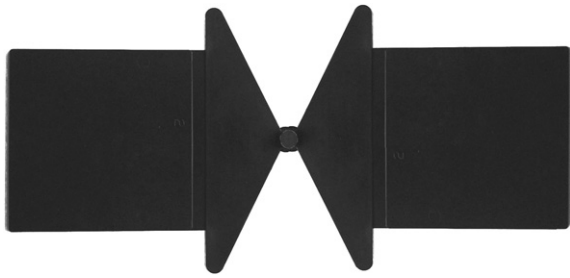


Fig. 1. Injection-moulded plates with fan gates.

scatter and complexities associated with friction effects [19]. However, note that the lubrication has a significant effect on the force-deflection curves, especially for ductile plates and large deflections, as shown in Fig. 3. With lubrication there is more localised biaxial plastic drawing under the striker hemisphere, while without lubrication there is more non-localised elastic and plastic bending, as well as uniaxial drawing outside the striker hemisphere. The higher peak force measured without lubrication agrees with the observations by Viana et al. [9].

Most of the tests were performed at 20 °C and –30 °C. When testing at –30 °C the specimens were conditioned according to the following procedure: Six specimens were loaded into the cold test chamber and one of them was mounted in the fixture. This first specimen was tested after 2 h. The next specimen was tested 15 min after mounting it and closing the chamber. The surface temperature of the specimen to be tested was monitored with a thermocouple.

The reproducibility of the force-deflection curves is generally quite good. The largest difference between repeated tests is typically seen near the maximum force where the variation in measured force for repeated tests is within 1–2%. The (natural) scatter is larger for the onset of unstable crack propagation.

3. Results and discussion

3.1. Force-deflection curves

All plate thicknesses were tested with impact velocities of 3.0 and 4.4 m/s at –30 °C and 20 °C. Some results for the

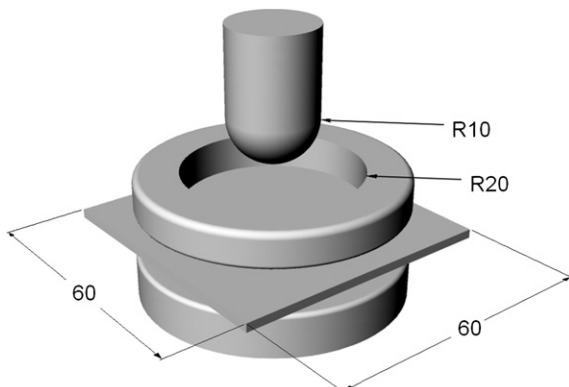


Fig. 2. Schematic drawing of striker, clamping device and test specimen.

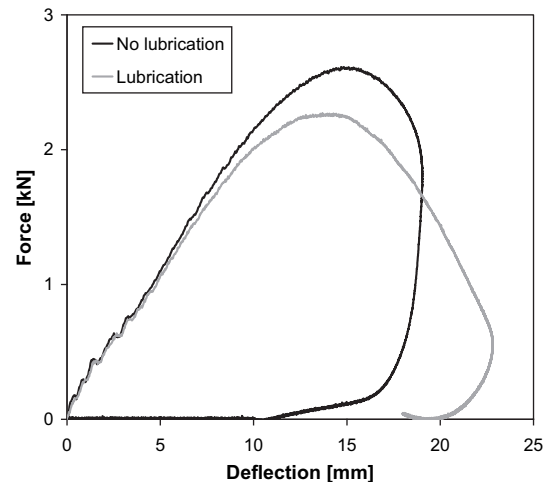


Fig. 3. Effect of lubrication on force vs. central deflection of plate (plate thickness 2.9 mm, impact velocity 4.4 m/s and temperature 20 °C).

highest impact velocity are shown in Fig. 4. This section will focus on the force-deflection curves in relation to macroscopic deformation mechanisms. First, note that the force-deflection curves can be categorised as follows:

- I. Curves with a predominantly positive slope after passing the peak force (zero derivative), i.e. a rather strong elastic rebound (but also some permanent deformation) so that the maximum deflection is close to the deflection at peak force. Examples: The thickest plates in Fig. 4a, as well as thick plates tested at 20 °C with lower impact velocities (not shown). The unloading slope and the permanent deformation are related to plastic deformation and other damages.
- II. Curves with a predominantly negative slope after passing the peak force (drawing), but no fracture and some rebound at the end of the curve. Example: The 2.9 mm thick plate in Fig. 4b.
- III. Curves showing fracture with mixed stable/unstable crack growth after drawing. Examples: The two thinnest plates in Fig. 4b.
- IV. Curves showing fracture with unstable crack growth (referred to as brittle fracture below) after passing the peak force. Example: The 2.0 mm thick plate in Fig. 4a. In this case, where brittle fracture occurs in all repeated tests, the fracture point (deflection, force) is highly reproducible.
- V. Curves showing fracture with unstable crack growth before reaching a zero derivative (i.e. no peak force). Example: Some repeated tests of 2.4 mm thick plates at –30 °C with impact velocity 4.4 m/s (not shown). However, note that 2.4 mm thick plates tested at these conditions also showed type I curves (Fig. 4a) and type IV curves.
- VI. Curves showing fracture with unstable crack growth in the elastic regime. Example: 2 mm thick plates tested at –60 °C with impact velocity 4.4 m/s fractured at deflections in the range 2–5 mm (not shown).

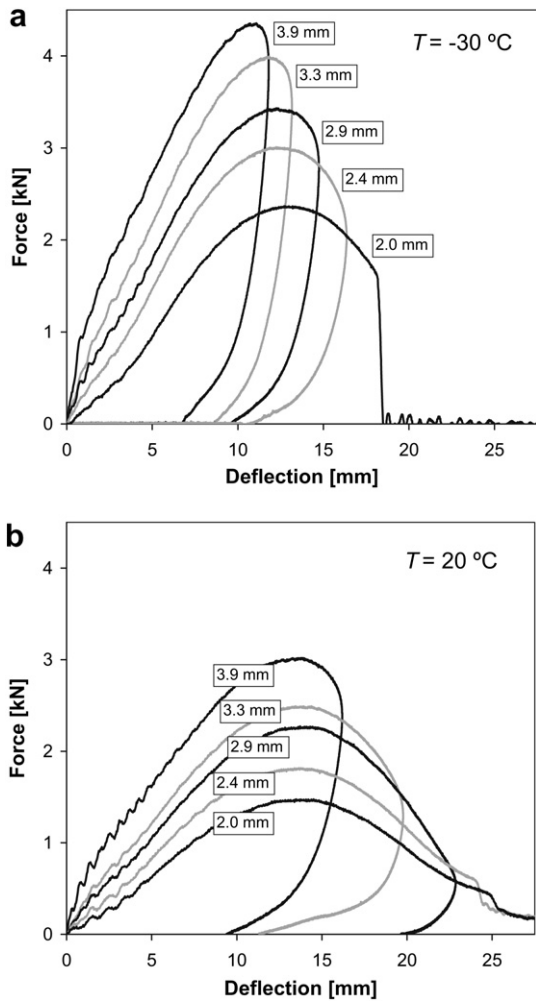


Fig. 4. Measured force vs. deflection (at the centre of the plate) for different plate thicknesses as indicated. Data for two different impact temperatures: a) $-30\text{ }^{\circ}\text{C}$ and b) $20\text{ }^{\circ}\text{C}$. The impact velocity was 4.4 m/s.

As a first approximation, the main effect of increasing the impact velocity is the same as that of reducing the test temperature or reducing the plate thickness. However, note that for a given plate thickness and temperature there is a force-deflection envelope curve corresponding to testing with a constant velocity throughout the (puncture) test, see Fig. 5. The peak force in a falling-weight test is lower than the peak force of the constant-velocity envelope curve, but the difference decreases with increasing impact energy in the falling-weight test. Note that the initial parts of the curves in Fig. 5 are almost independent of impact velocity. This is the case for all velocities in our study (1–6 m/s), i.e. the strain rate effect on the elastic modulus is negligible. From a certain force level before the peak force and well past the peak force (constant-velocity curves in Fig. 5) there is an effect of test velocity, which is probably the effect of strain rate on the yield stress.

Although this is a simple test geometry, the load-deflection curve is the result of a complicated interplay between the non-linear material response, the changing contact area and, possibly, changing friction between plate

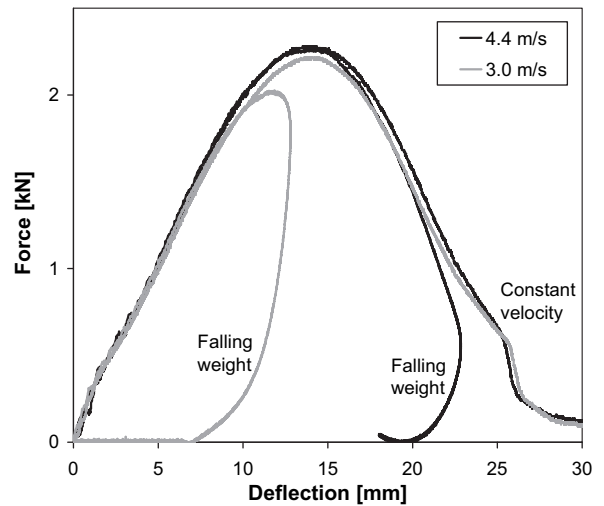


Fig. 5. Comparison between testing with falling weight and constant velocity. Data for 2.9 mm thick plates tested at $20\text{ }^{\circ}\text{C}$ with two different impact velocities.

and striker, the variation in strain rate and stress state over the geometry vs. deflection, and residual stresses in the plate. In the falling-weight test, the strain rate will also decrease with deflection up to peak force, and the strain rate sensitivity of the material may influence the force-deflection curve. Moreover, some parts of the force-deflection curves reflect rather localised deformations. Finally, dissipative heating may affect the response at the strain rates used in this study.

Initially, the deformation is dominated by (linear) elastic bending, for which the force is proportional to wh^3 [20,21], or $F^* \propto w^*$ (see Fig. 6 for plot and definition of the dimensionless parameters F^* and w^*). Our data seem to be in this regime for small deflections. The initial F^* - w^* slope for our data is in agreement with elastic bending theory, i.e. when using a reasonable modulus E to scale F^* , the theoretical F^* - w^* slope [20] is obtained (in Fig. 6 the quasi-static modulus at $23\text{ }^{\circ}\text{C}$ is used). It was noted that the effect of plate thickness on the force-deflection curves at small deflections could be slightly better described by $F \propto wh^2$ (insert in Fig. 6). With a lower exponent (for h), $< \sim 1.8$, the curves separated.

As the deflection increases, plastic bending and stretching will take over [20,22,23]. For pure elastic stretching, $F^* \propto w^{*3}$ ($F \propto w^3h$) [22,24], but this was not observed in our data at $-30\text{ }^{\circ}\text{C}$, except perhaps for a portion of the curve for the thinnest plate. The plates are plastically deformed when wrapped around the hemispherical striker: The plate thickness h that can be elastically wrapped around a striker with radius S can be estimated [20] as

$$h < 2SY(1 - \nu^2)/E \quad (1)$$

where Y is the yield stress, ν is the Poisson's ratio and E is the elastic modulus. The ratio Y/E depends on the strain rate and the temperature, but with typical material data at room temperature the plate thickness must be below 0.2 mm, according to this expression based on linear elasticity.

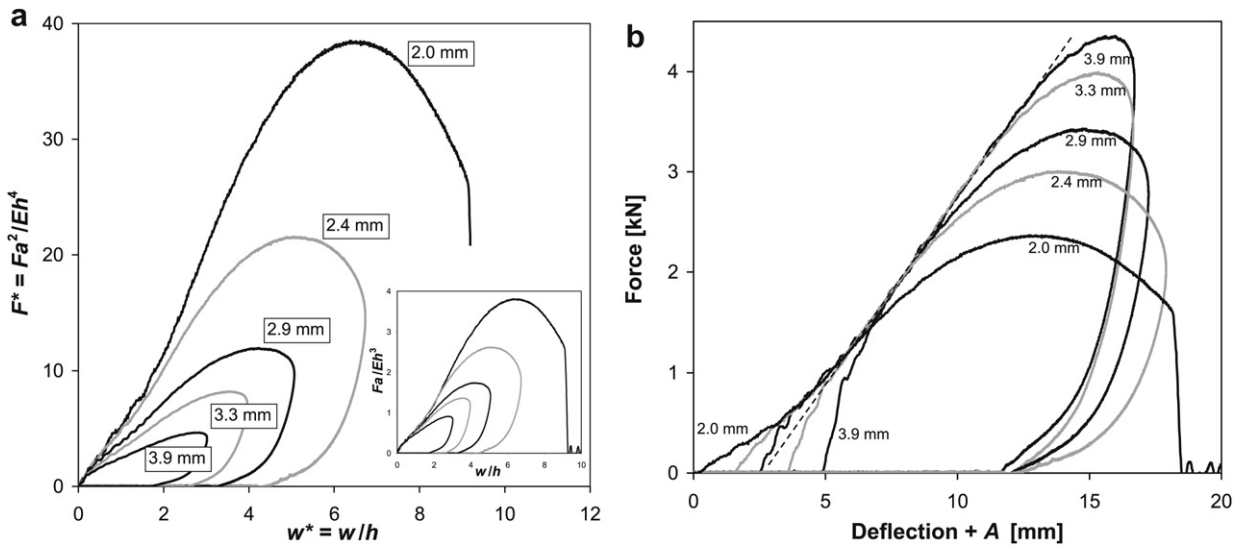


Fig. 6. Data as in Fig. 4a, but plotted with scaled axes. a) Dimensionless units F^* and w^* (F = force, a = plate radius (inside clamp), E = elastic modulus, h = initial plate thickness, w = central deflection of plate). In the insert the y axis unit is changed, so that the relation $F \propto wh^2$ is assessed. b) Curves shifted horizontally (see main text).

Note that large portions of the curves to the left of the peak force have almost the same slope for the different plate thicknesses, see for example the four thickest plates in Fig. 4a. If the curves in Fig. 4a are shifted horizontally so that the portions with the same slope coincide (Fig. 6b), the curve portions at the right of the peak force will also be brought closer to each other. Also note that, except in the initial and final stages of the unloading, the three thickest plates in Fig. 6b have almost the same effective unloading modulus.

The increase in peak force with increasing plate thickness is well described by a second order polynomial in this limited thickness range, see Fig. 7. In the plate impact puncture literature (with near constant striker velocity through the test), covering various polymers, the peak force is found to be proportional to h^n with n in the range 1.0–1.4 [19] or 1–2 [25].

Note that the slopes in Fig. 7 mainly depend on the impact velocity. The effect of impact velocity in Fig. 7 can be explained by considering the trends in Fig. 5. For thin plates (thinner than in Fig. 5), the peak force is about the same for both impact velocities in Fig. 7, because the load-deflection curves are close to the constant-velocity envelopes in both cases. For thicker plates (as in Fig. 5), the force-deflection curve obtained with impact velocity of 3.0 m/s deviates from this envelope, but not that obtained at 4.4 m/s. This explains the effect of impact velocity in Fig. 7.

The effect of plate thickness in Fig. 7 can be rationalised by considering Fig. 6b. For the thickest plates, the incident impact energy (the kinetic energy of the striker, which is the same for all plates) is close to the integrated force up to the peak force, while the effective slope (dashed line) and the (shifted) deflection at peak force are roughly independent of plate thickness. Hence, a higher peak force for a thicker plate is then mainly due to the lower energy absorption relative to that defined by the effective slope (dashed line) at small (shifted) deflections. For thinner plates, the difference between the deflection at peak force

and the maximum deflection is no longer small, so the energy to peak force is significantly lower than the incident energy. Hence, the energy to peak force increases with plate thickness.

Elastic rebound (springback) has been assessed theoretically for plates in general [20], and the unloading in uniaxial tensile tests and torsion tests has been studied and modelled for PP materials [26,27]. The main characteristics of the unloading curve for plates can be simulated with an effective unloading modulus, $E_{\text{eff}}(\epsilon_p)$, based on tests with unloading from different plastic strains ϵ_p [7,28].

The drawing of the plate after reaching the peak force, for plates in category II and III defined above, leads to localised

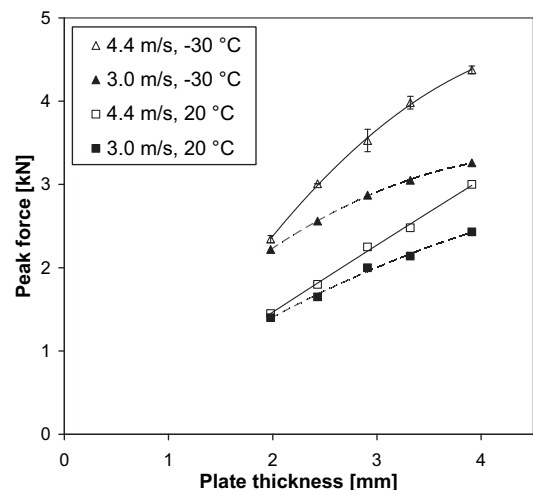


Fig. 7. Peak force vs. plate thickness for impact velocities and temperatures as given in the legend. The lines are fits with second order polynomials. The error bars for the upper data set represent two times the standard deviation of three repeated tests (some repeats were done several months after the first).

thinning (necking) under the striker, resulting in very thin “films” in the most ductile cases, see Fig. 8 (photos of plates after elastic rebound). In fact, this test and the related bulge test are used to obtain data at large strains, even for materials with little strain-hardening [29]. Note that a diffuse neck does not develop due to the striker exerting a geometrical constraint on the strain distribution [30].

3.2. Fracture patterns

Increasing the impact velocity or reducing the plate thickness increases the maximum stress in the plate, at least for deflections up to a certain value. For elastic bending of an unclamped plate, the radial and circumferential tensile stresses are highest and equal at the centre of the plate, on the surface opposite the striker [21] (Fig. 9, position a). Both stress components decrease radially, and outside the centre the circumferential component is higher than the radial component [21]. This explains the radial cracks starting at the centre in elastic (brittle) plates. For clamped plates, local tensile stress maxima can also occur in other regions: On the impacted side, in a circle with diameter similar to that of the of the striker (Fig. 9, position b), due to the bending of the plate by the striker (at least for some striker geometries and diameters), as well as around the circumference near the clamp on the impacted side (Fig. 9, position c), due to the bending of the plate near the clamp. The latter two stresses are uniaxial, while the stress under the striker is biaxial.

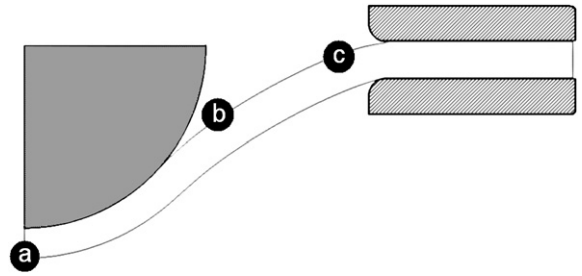


Fig. 9. Axisymmetric schematic drawing of a clamped deformed plate showing positions of local tensile stress maxima (see main text).

Also, for pure stretching, there is a maximum in (equi-biaxial) tensile stress at the pole of the deformed plate (Fig. 9, position a) if there is no friction between the striker and the plate. With friction, the maximum is shifted away from the pole [29]. Note that for elastic bending the stresses are proportional to h^{-2} where h is the plate thickness, while for pure stretching the membrane stresses are proportional to h^{-1} .

With an impact velocity of 3 m/s, fracture was not observed for any of the plate thicknesses, either at 20 °C or –30 °C. With an impact velocity of 4.4 m/s, the thinnest plates fractured: At –30 °C (Fig. 4a), 2.0 mm thick plates fractured in a brittle manner, while 2.4 mm plates showed brittle fracture in some of the repeated tests, i.e. it was a borderline case. Also at 20 °C (Fig. 4b), the two thinnest plates fractured, but with a different fracture pattern than at –30 °C. The macroscopic fracture patterns observed in this study can be categorised as follows:

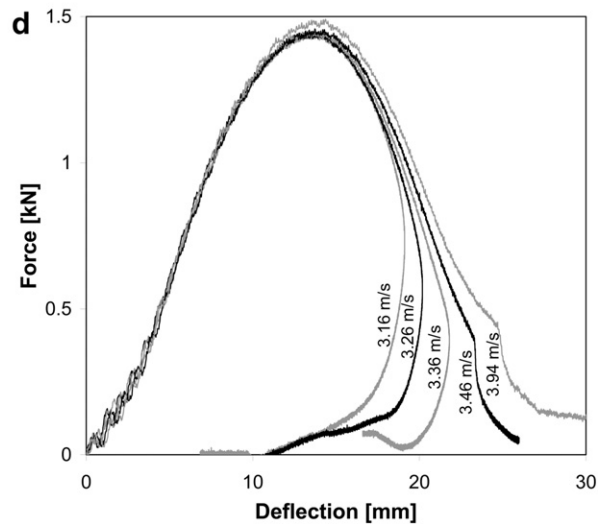
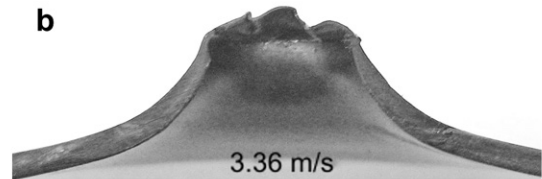
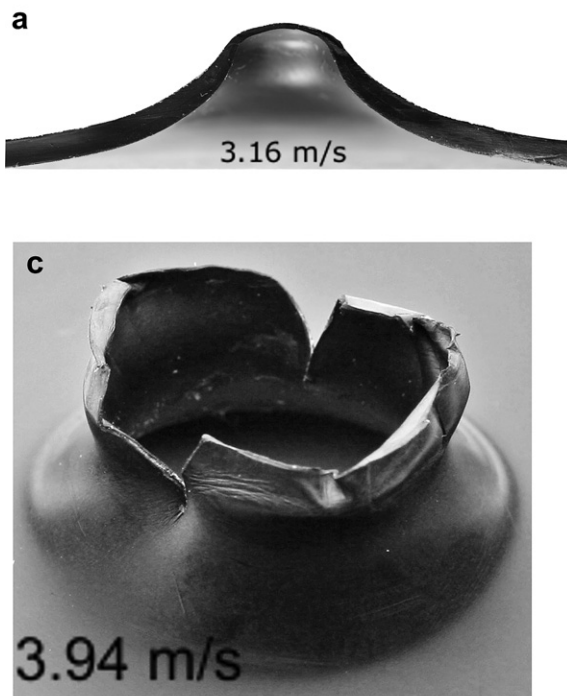


Fig. 8. Results for 2.0 mm thick plates tested at 20 °C with impact velocities as indicated (same impactor mass). a)–c) Photos of tested plates. Plates in a) and b) were cut through the centre to show the thickness profile. d) Force-deflection curves.

- A. For the most brittle cases (below ~ -45 °C with an impact velocity of 4.4 m/s, i.e. for force-deflection curves of type VI), a central crack runs parallel to the flow direction (Fig. 10). The number of fragments increases with decreasing temperature, but even for fractures at -60 °C a central crack parallel to the flow direction can be discerned (Fig. 10). A circumferential crack forms after the radial crack(s), see explanation for fracture type B below. In some tests at -60 °C more fragmented fractures are obtained than shown in Fig. 10. In some cases two concentric circumferential cracks appear, while there still are six radial cracks. Also, for this case the central crack is parallel to the flow direction.
- B. At -30 °C (force-deflection curves of type IV) a crack initiates at the centre and grows radially outwards in both directions perpendicular to the flow direction. After this, circumferential cracks form. The result is that two fragments are knocked out of the plate (Fig. 10). The circumferential cracks form as the maximum stress is transferred to this radial position (Fig. 9, near position c) when the central crack has reached a certain length. In addition, there will already be a local tensile stress maximum in this position, as mentioned above. Sometimes the central crack runs all the way out to the edge of the plate (outside the clamping).
- C. Similar to B, but the radial crack from the centre only grows in one direction from the centre and outwards. The reason could be that the maximum stress is shifted away from the pole. This crack pattern is less common than pattern B, and was only observed for 2.0 mm thick plates.
- D. At 20 °C, deep drawing and localised thinning under the striker (force-deflection curve type III) leads to a so-called petaling fracture (Fig. 10), which seems to start with a central radial crack nearly perpendicular to the (injection moulding) flow direction. Note that a similar puncture pattern, but without the central crack, was observed for almost isotropic extruded plates.
- E. In tests of 2.0 mm thick plates with very low loading rates (a few millimetres per second) at room temperature, deep drawing was followed by circumferential fracture around a small cap around the striker tip (Fig. 10). The fracture occurred for a relative deflection, w/h , around 10. Sometimes the cap fell off, sometimes a small hinge remained. This fracture could be associated with the maximum stress being shifted away from the pole, as mentioned earlier in this section. A shift in the maximum strain was observed directly by 3D digital image correlation. For low loading rates it is reported that friction cannot be neglected [19], and friction is the cause for the shift. The same fracture type was observed with and without lubrication on the striker. With lubrication, it was remarkable that the inside of the drawn cap was dry after testing. If the friction is high enough, the polymer film will effectively adhere to the striker hemisphere, and the deformation will only take place in the deep-drawn cylinder. In this case it is likely that the circumferential crack will start near the bend from the cylinder to the hemisphere.

For brittle fractures at low strains (fracture type A described above), cracks running parallel to the flow direction were expected, because the fracture resistance will be highest in the perpendicular direction due to the flow-induced orientation of polymer molecules and crystallites, as well as talc particles. Furthermore, the anisotropy is usually high near the surface where the tensile bending stress is highest. Brittle cracks propagating parallel to the flow direction in injection-moulded plates have been reported earlier [25,31–33], but many papers do not give any information about the crack direction. The effect of talc on the orientation and crystallinity of injection-moulded PP was recently studied [34].

On the other hand, a central crack running perpendicular to the flow direction was observed for fractures after rather deep drawing (fracture type B–D). In these cases, the semi-crystalline morphology is highly deformed, transformed and oriented by the stretching [35], and one may speculate that fracture occurs when an ultimate draw ratio is reached [36]. Polymer chain scission may also occur when the strain rate is high relative to the inverse relaxation time of the polymer chains. The ultimate draw ratio is perhaps first reached in the direction with some initial molecular orientation from the injection moulding process. Hence, the cracks would run perpendicular to the (injection moulding) flow direction. The stress state may also play a role, since there is biaxial tension under the striker, but uniaxial tension on the sides. Cracks propagating perpendicular to the flow direction have been observed for PC-ABS plates [37]. For aluminium sheets tested in biaxial tension, it is reported that central cracks can run either parallel or perpendicular to the processing (rolling) direction [38].

Circumferential cracks forming after one or more radial cracks (for fracture type A–C) have also been reported in the literature [32,39–42]. The competition between these two crack formations is affected by material characteristics and impact conditions: Karger-Kocsis et al. [41] reported that the probability of circumferential crack formation in PP increased with increasing β phase content (the β phase being more ductile than the α phase), increasing molecular weight, increasing test temperature and decreasing impact velocity. Furthermore, the fracture pattern shifts from a single radial crack to multiple radial cracks and splintering as the brittle character increases, e.g. with decreasing temperature (as observed in our study) or decreasing elastomer content [40,42]. Furthermore, material characteristics, such as elastomer content, affect whether the radial cracks propagate beyond the clamping or not [40,42].

Deep drawing ending with a cap being torn off (fracture type E, observed for low loading rates) has been reported for impact testing of PP [39,40,42], but the mechanism has not been discussed, as far as the authors are aware. Some similar observations for PE have been reported and discussed, including the effect of friction [43]. Our proposed mechanism, based on a friction-induced shift in maximum stress away from the pole, and for high friction even out of the hemisphere, was outlined above.

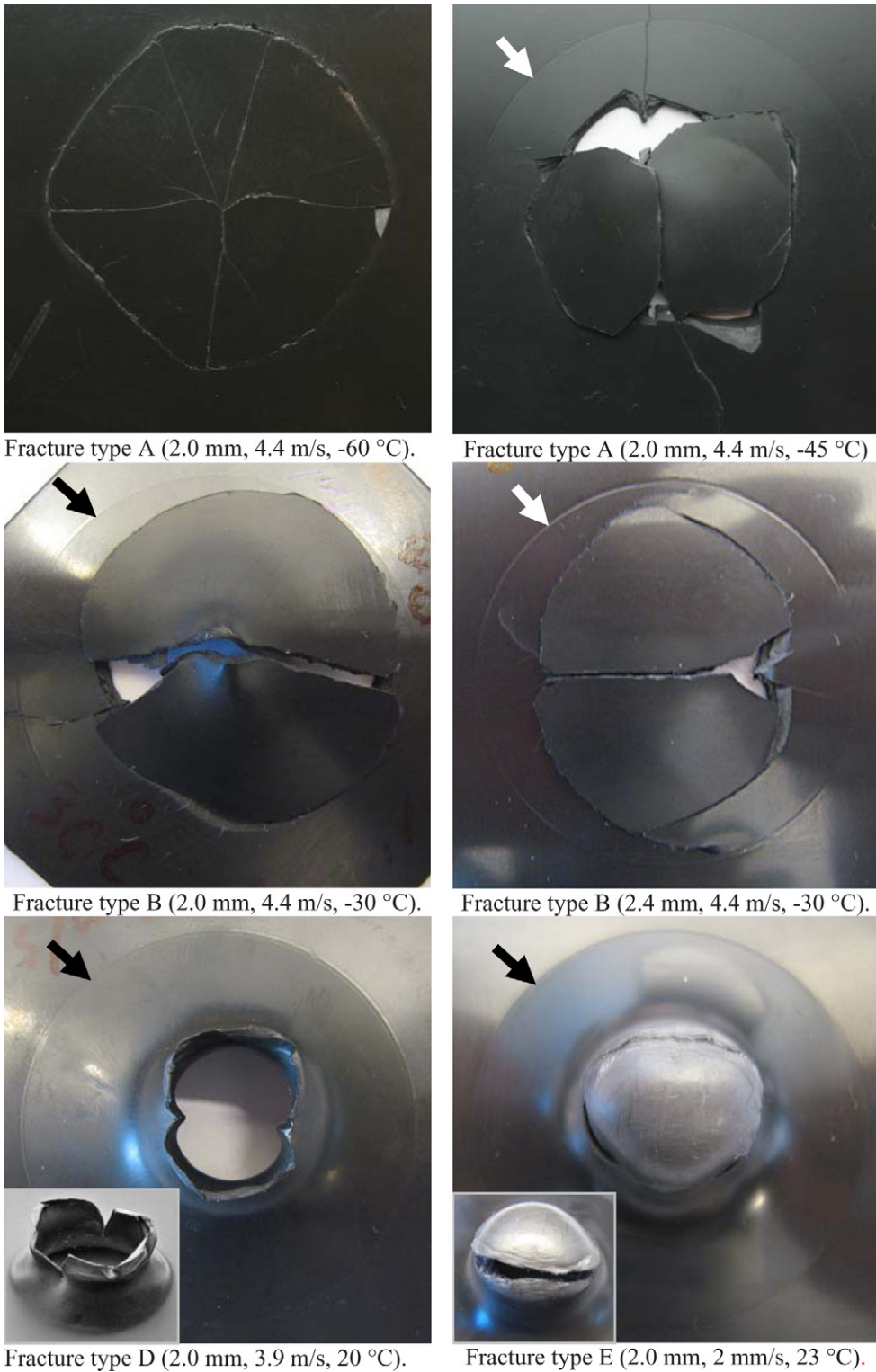


Fig. 10. Different fractures obtained with the \varnothing 20 mm hemispherical striker. The parameters given in parentheses below the photos are plate thickness, impact velocity and temperature, respectively. The melt flow direction is vertical in all photos (except the inserts). The indentation marks (rings) from the clamping are indicated with arrows. See main text for details.

4. Conclusions

We have presented and analysed the low-velocity impact response of an industrially important polymer material; mineral and elastomer modified polypropylene.

- The plate impact test was chosen due to its relevance for impact events commonly occurring during the service life of injection-moulded components.
- Plates with thicknesses from 2 to 4 mm were tested.
- The paper has emphasis on the performance at $-30\text{ }^{\circ}\text{C}$, but the measurements also span a wide temperature range (-60 to $20\text{ }^{\circ}\text{C}$).

Regarding the main findings, these are our conclusions:

- Force-deflection curves and fracture patterns have been categorised and analysed. The main trends can be explained in terms of the classical brittle-ductile picture and the anisotropy of the plates. Note that with typical impact velocity and energy values used in low-velocity impact tests, plates with thickness below a certain value fracture at both -30 to $20\text{ }^{\circ}\text{C}$, although with different mechanisms.
- The direction of the central radial crack was observed to change as the fracture changed from brittle to semi-ductile. In the former case the crack ran parallel to the melt flow direction. In the latter case it ran perpendicular to the flow direction. Radial cracks parallel to the flow direction for brittle fractures were expected. Radial cracks nearly perpendicular to the flow direction after deep drawing may be explained by an ultimate draw ratio being reached first in the flow direction.
- Regarding numerical simulation of the mechanical response, some of the observed features require further development of material models.

A forthcoming paper [5] based on the same study deals with effects of striker geometry, plate surface roughness, melt flow weld lines, and paint.

Acknowledgment

This work and the PhD studentship of Hamid Daiyan were funded by the Research Council of Norway (BIA programme) and Plastal AS.

References

- [1] N. Fanegas, M.A. Gomez, I. Jimenez, C. Marco, J.M. Garcia-Martinez, G. Ellis, Optimizing the balance between impact strength and stiffness in polypropylene/elastomer blends by incorporation of a nucleating agent. *Polym Eng Sci* 48 (1) (2008) 80.
- [2] C. Grein, Toughness of neat, rubber modified and filled beta-nucleated polypropylene: from fundamentals to applications. *Adv Polym Sci* 188 (-) (2005) 43.
- [3] C.J.G. Plummer, Microdeformation and fracture in bulk polyolefins. *Adv Polym Sci* 169 (-) (2004) 75.
- [4] Y. Cao, J. Feng, P. Wu, Simultaneously improving the toughness, flexural modulus and thermal performance of isotactic polypropylene by alpha-beta crystalline transition and inorganic whisker reinforcement. *Polym Eng Sci* 50 (2) (2010) 222.
- [5] H. Daiyan, E. Andreassen, F. Grytten, O.V. Lyngstad, T. Luksepp, H. Osnes. Low-velocity impact response of injection-moulded polypropylene plates – Part 2: effects of striker geometry, surface texture, weld lines and paint. *Polym Test*, in press.
- [6] E. Andreassen, H. Daiyan, F. Grytten, O.V. Lyngstad, R.H. Gaarder, E.L. Hinrichsen. In: Proceedings of the 24th Annual Meeting of the Polymer Processing Society, Salerno, Italy, 2008.
- [7] H. Daiyan, F. Grytten, E. Andreassen, O.V. Lyngstad, H. Osnes, R.H. Gaarder, E.L. Hinrichsen. In: Proceedings of the 7th European LSDYNA Conference, Salzburg, Austria, 2009.
- [8] C.M. Tai, R.K.Y. Li, C.N. Ng, Impact behaviour of polypropylene/polyethylene blends. *Polym Test* 19 (2) (2000) 143.
- [9] J.C. Viana, A.M. Cunha, N. Billon, Experimental characterization and computational simulations of the impact behavior of injection-molded polymers. *Polym Eng Sci* 47 (4) (2007) 337.
- [10] Y. Duan, A. Saigal, R. Greif, M.A. Zimmerman, Impact behavior and modeling of engineering polymers. *Polym Eng Sci* 43 (1) (2003) 112.
- [11] Y. Duan, A. Saigal, R. Greif, M.A. Zimmerman, Analysis of multi-axial impact behavior of polymers. *Polym Eng Sci* 42 (2) (2002) 395.
- [12] G. Dean, L. Wright, An evaluation of the use of finite element analysis for predicting the deformation of plastics under impact loading. *Polym Test* 22 (6) (2003) 625.
- [13] Y. Duan, A. Saigal, R. Greif, M.A. Zimmerman, Modeling multi-axial impact behavior of a glassy polymer. *Mater Res Innov* 7 (1) (2003) 10.
- [14] O. Schang, N. Billon, J.M. Muracciole, F. Fernagut, Mechanical behavior of a ductile polyamide 12 during impact. *Polym Eng Sci* 36 (4) (1996) 541.
- [15] L. Crocker, G. Dean, Prediction of impact performance of plastics mouldings, part 2: finite element simulations. *Plast Rubber Compos* 36 (1) (2007) 14.
- [16] R. Singh, A. Mattoo, A. Saigal, Optimizing the design and impact behavior of a polymeric enclosure. *Mater Design* 27 (10) (2006) 955.
- [17] G.G. Trantina, R. Nimmer, Structural Analysis of Thermoplastic Components. McGraw-Hill, 1994.
- [18] F. Grytten, H. Daiyan, M. Polanco-Loria, S. Dumoulin, Use of digital image correlation to measure large-strain tensile properties of ductile thermoplastics. *Polym Test* 28 (6) (2009) 653.
- [19] ISO 6603-2, 2000. Plastics–Determination of Puncture Impact Behaviour of Rigid Plastics–Part 2: Instrumented Impact Testing.
- [20] T.X. Yu, L.C. Zhang, Plastic Bending – Theory and Applications. World Scientific, 1996, Ch 7.
- [21] P.E. Reed, Elastic analysis of the flexed plate impact test. *J Strain Anal Eng* 25 (4) (1990) 207.
- [22] K.T. Wan, S.C. Lim, The bending to stretching transition of a pressurized blister test. *Int J Fracture* 92 (4) (1998) L43.
- [23] J. Chakrabarty, Large deflections of a clamped circular plate pressed by a hemispherical-headed punch. *Met Mater Int* 4 (4) (1998) 680.
- [24] K.T. Wan, K. Liao, Measuring mechanical properties of thin flexible films by a shaft-loaded blister test. *Thin Solid Films* 352 (1–2) (1999) 167.
- [25] D.R. Moore, S. Turner, Mechanical Evaluation Strategies for Plastics. CRC Press, 2001, Ch 11.
- [26] M. Zrida, H. Laurent, G. Rio, S. Pimbert, V. Grolleau, N. Masmoudi, C. Bradai, Experimental and numerical study of polypropylene behavior using an hyper-visco-hysteresis constitutive law. *Comp Mater Sci* 45 (2) (2009) 516.
- [27] K. Hizoum, Y. Remond, N. Bahlouli, V. Oshmyan, S. Patlazhan, S. Ahzi, Non linear strain rate dependency and unloading behavior of semi-crystalline polymers. *Oil Gas Sci Technol* 61 (6) (2006) 743.
- [28] P.A. Du Bois, S. Kolling, M. Koesters, T. Frank, Material behaviour of polymers under impact loading. *Int J Impact Eng* 32 (5) (2006) 725.
- [29] Z. Marciniak, J.L. Duncan, S.J. Hu, Mechanics of Sheet Metal Forming, 2nd. Butterworth-Heinemann, 2002, Ch 9.
- [30] Z. Marciniak, J.L. Duncan, S.J. Hu, Mechanics of Sheet Metal Forming, 2nd. Butterworth-Heinemann, 2002, Ch 5.
- [31] S. Turner. Failure of plastics. *RAPRA Review Reports*. Vol 5, No 4 (Report 41), 1991.
- [32] J. Karger-Kocsis, D.E. Mouzakis, G.W. Ehrenstein, J. Varga, Instrumented tensile and falling weight impact response of injection-molded alpha- and beta-phase polypropylene homopolymers with various melt flow indices. *J Appl Polym Sci* 73 (7) (1999) 1205.
- [33] T.R. Crompton, Polymer Reference Book. Smithers Rapra Technology, 2006, Ch 18.
- [34] M.C. Branciforti, C.A. Oliveira, J.A.d. Sousa. Molecular orientation, crystallinity, and flexural modulus correlations in injection molded polypropylene/talc composites. *Polym Adv Technol*, in press.
- [35] J.C. Viana, Structural interpretation of the strain-rate, temperature and morphology dependence of the yield stress of injection molded semicrystalline polymers. *Polymer* 46 (25) (2005) 11773.

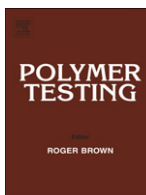
- [36] R. Seguela, On the natural draw ratio of semi-crystalline polymers: review of the mechanical, physical and molecular aspects. *Macromol Mater Eng* 292 (3) (2007) 235.
- [37] F. Huberth, S. Hiermaier. In: *Proceedings of the International Conference on Impact Loading of Lightweight Structures*, Trondheim, Norway, 2008.
- [38] D.V. Wilson, P.M.B. Rodrigues, On the directionality of strain localization when stretching aluminium alloy sheets in biaxial tension. *Metall Trans A* 17 (2) (1986) 367.
- [39] D.P. Jones, D.C. Leach, D.R. Moore, *Plast Rubber Process Appl* 6 (1) (1986) 67.
- [40] W.Y. Tam, T. Cheung, R.K.Y. Li, An investigation on the impact fracture characteristics of EPR toughened polypropylene. *Polym Test* 15 (4) (1996) 363.
- [41] J. Karger-Kocsis, E. Moos, I. Mudra, J. Varga, Effects of molecular weight on the perforation impact behavior of injection-molded plaques of alpha- and beta-phase isotactic polypropylenes. *J Macromol Sci-Phys B* 38 (5–6) (1999) 647.
- [42] W.Y. Tam, T.Y.H. Cheung, R.K.Y. Li, Impact properties of glass fibre/impact modifier/polypropylene hybrid composites. *J Mater Sci* 35(6)(2000) 1525.
- [43] P.E. Reed, Falling weight impact testing and design. *Plast Rubber Comp Process Appl* 17 (3) (1992) 157.

Paper 2

H. Daiyan, E. Andreassen, F. Grytten, O.V. Lyngstad, T. Luksepp, H. Osnes

Low-velocity impact response of injection-moulded polypropylene plates – Part 2: Effects of moulding conditions, striker geometry, clamping, surface texture, weld line and paint

Polymer Testing, Volume 29, Issue 7, 2010



Material Performance

Low-velocity impact response of injection-moulded polypropylene plates – Part 2: Effects of moulding conditions, striker geometry, clamping, surface texture, weld line and paint

H. Daiyan^a, E. Andreassen^{a,*}, F. Grytten^a, O.V. Lyngstad^{b,1}, T. Luksepp^{b,2}, H. Osnes^c

^a SINTEF, Box 124 Blindern, NO-0314 Oslo, Norway

^b Plastal AS, Box 94, NO-2831 Raufoss, Norway

^c Department of Mathematics, University of Oslo, Box 1053 Blindern, NO-0316 Oslo, Norway

ARTICLE INFO

Article history:

Received 30 April 2010

Accepted 5 June 2010

Keywords:

Polypropylene

Impact

Plate

Low temperature

Fracture

Weld line

Paint

Surface roughness

ABSTRACT

The low-velocity, low-energy impact response of a mineral and elastomer modified polypropylene was characterised by instrumented falling-weight impact testing of plates with annular clamping. Most of the impact tests were performed at $-30\text{ }^{\circ}\text{C}$ with incident impact velocities in the range 1.0–4.4 m/s, and with plate thicknesses in the range 2.0–3.9 mm. The following factors were investigated: moulding conditions (mould temperature, melt temperature, holding pressure), striker geometry, clamping, plate surface texture, melt flow weld lines and paint. The occurrence of brittle fracture was affected by all these factors, except the moulding conditions. Reducing the striker hemisphere diameter or changing to a flat striker induced brittle fracture. Removing the annular clamping led to a more brittle response. Plates with a weld line were more brittle than standard plates. The surface texture caused brittle fracture when the textured side was in tension under the striker. The paint induced brittle fracture at $-30\text{ }^{\circ}\text{C}$, but no adverse effect of the paint was observed at $20\text{ }^{\circ}\text{C}$.

© 2010 Elsevier Ltd. All rights reserved.

1. Introduction

The impact resistance of thermoplastic polymer materials is important for many applications. The automotive industry and their suppliers are important driving forces in this field. The polypropylene (PP) compound studied in this paper is optimised for automotive exterior parts such as bumper covers (the bumper cover is the outer part of the bumper, with or without paint).

The study reported in this paper was initiated to improve the understanding of factors influencing the low-

velocity, low-energy impact response, especially at low temperatures. In cold winter conditions, minor impacts on the bumper cover should not result in brittle fracture.

With a given polypropylene compound, the apparent brittleness of a bumper cover, when impacted with a striking object, is related to several coupled factors: 1) Loading conditions (temperature, velocity, energy, striker tip geometry). 2) Bumper cover details (thickness, paint, surface roughness, local constraints due to cover geometry and assembly). 3) Injection moulding process (morphology including inhomogeneity and anisotropy, residual stresses, weld lines).

This paper addresses some of these effects with an idealised test: an annularly clamped plate struck with a hemispherical striker perpendicular to the plate. Note that with this test the fracture is in most cases initiated in a biaxial stress state (at the center of the plate).

Part 1 of this study [1] dealt with the effects of plate thickness, impact speed and temperature on the impact

* Corresponding author. Tel.: +47 98282492.

E-mail address: erik.andreassen@sintef.no (E. Andreassen).

¹ Present affiliation: SINTEF Raufoss Manufacturing, Box 163, NO-2831 Raufoss, Norway.

² Present affiliation: Norwegian Composite Center, Box 163, NO-2831 Raufoss, Norway.

Table 1
Selected material properties.

Melt flow rate (ISO 1133) (230 °C, 2.16 kg) (dg/min)	Density (ISO 1183) (kg/m ³)	Flexural modulus (ISO 178) (2 mm/min) (GPa)	Tensile stress at yield (ISO 527-2) (50 mm/min) (MPa)	Flexural strength (ISO 178) (MPa)	Charpy impact strength, notched (ISO 179/1eA) at $T = -30, -20$ and 23 °C (kJ/m ²)
13	1050	1.6	16	22	5, 6 and 58

response. The reader should also refer to Part 1 for a summary of literature on impact testing of PP plates.

2. Experimental

2.1. Material and standard mechanical properties

The material in this study is a 20% mineral (talc) and elastomer modified polypropylene compound (ISO code PP+EPDM-TD20) for automotive exterior parts. This material was also used in an earlier study [2]. Some selected properties from the material data sheet are given in Table 1. Note that unnotched specimens of this material do not break in Charpy impact tests (ISO 179/1eU) at -20 °C and 23 °C . The material has a melting point at 163 °C (injection-moulded plate characterised by differential scanning calorimetry, peak of endotherm during first heating, 10 K/min).

Note that the focus in this article is on the typical trends for this class of materials, not the details of this specific material.

2.2. Preparation of test specimens

Plates with thicknesses of 2.0, 2.4, 2.9, 3.3 and 3.9 mm were injection moulded using fan-gated cavities with polished surfaces, see Fig. 1a. Details of the injection moulding equipment and conditions were given in Part 1 [1]. Furthermore, for a set of 2.4 mm thick plates, some of the moulding conditions were varied, see details in Section 3.

All plates measured $60 \times 60\text{ mm}^2$ and were used directly in the test, except the 3.9 mm thick plates which were milled to $\varnothing 60\text{ mm}$ plates from $80 \times 80\text{ mm}^2$ moulded plates.

Mould inserts were used to make plates with weld lines (Fig. 1b) and plates with textured surfaces. For the latter, the mould insert was photoetched with one of the coarsest patterns used for unpainted bumper covers. The peak-to-valley distance of this pattern is $\sim 85\text{ }\mu\text{m}$ and the average root radius of the humps is $\sim 0.1\text{ mm}$; however, there are some sharper “pre-cracks” in this texture, see Fig. 2.

Some plates were painted on one side with a commercial paint system for bumper covers in PP compounds. This paint system consists of an adhesion promoter (based on a chlorinated polyolefin), a basecoat and a clearcoat (based on polyurethane).

2.3. Mechanical testing

The tests were performed with an instrumented falling-weight impact tester (Rosand type 4, modified by Imatek) fitted with a 20-kN piezoelectric force transducer (Kistler

9331B). The plates were pneumatically clamped by a serrated ring with inner diameter 40 mm (Figs. 3 and 4). The clamping force was 3 kN. The plate impact test in this study is similar to the standard instrumented puncture impact test [3], but a lower drop mass was used, typical for low-energy impact tests in the automotive industry. The drop mass was 3.5 kg in all tests. The (incident) impact velocities were in the range 1.0–4.4 m/s. A comparison with constant-velocity tests, using a servo-hydraulic machine, was reported in Part 1 [1].



Fig. 1. (a) Injection-moulded plates ($60 \times 60\text{ mm}^2$) with fan gates produced in a two-cavity mould, and (b) a plate ($80 \times 80\text{ mm}^2$) filled from two adjacent corners, resulting in a weld line where the flow fronts from the two gates meet.

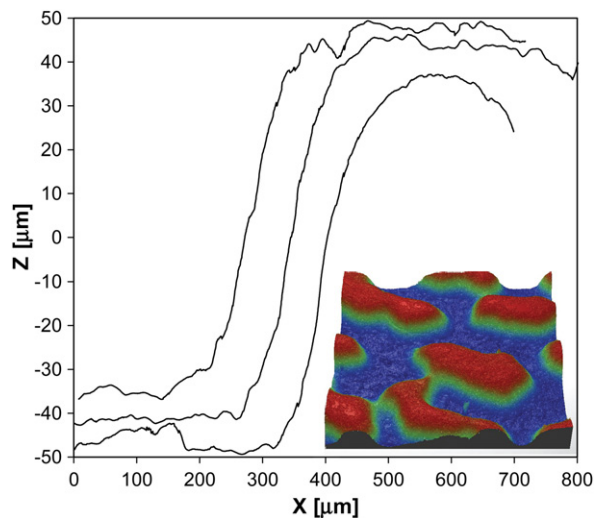


Fig. 2. Surface topography of textured plate characterised by scanning white light interferometry. Three typical height profiles for the surface “humps” are shown (shifted horizontally for clarity), taken from the 3D topography in the insert at the bottom right, covering an area of $1.5 \times 1.5 \text{ mm}^2$.

A hemispherical $\varnothing 20 \text{ mm}$ striker was used if nothing else is stated. In addition, some results obtained with a hemispherical $\varnothing 12.7 \text{ mm}$ striker and flat $\varnothing 20 \text{ mm}$ striker (with 45° chamfer) are reported. The strikers were lubricated with silicone grease in order to avoid some of the scatter and complexities associated with friction effects [1,3]. Most of the tests reported below were performed at -30°C . The procedure for conditioning the specimens at this temperature was described in Part 1 [1].

3. Results and discussion

3.1. Effects of injection moulding process conditions

The mechanical properties of injection-moulded (IM) parts are in general affected by the moulding conditions via the morphology and residual stresses. In this study, some processing parameters were varied for the 2.4 mm thick plates. As reported in Part 1 [1], this plate thickness was

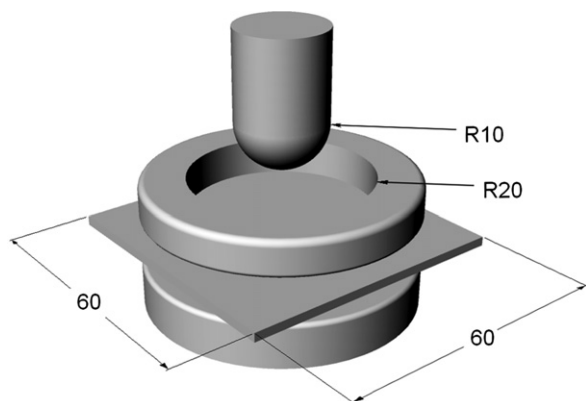


Fig. 3. Schematic drawing of striker, annular clamping device and test specimen ($60 \times 60 \text{ mm}^2$ plate).

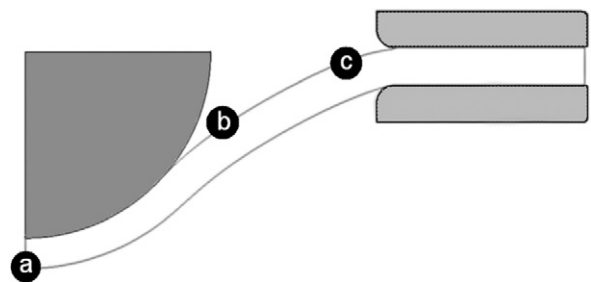


Fig. 4. Axisymmetric schematic drawing of clamped deformed plate showing positions of local tensile stress maxima.

a borderline case regarding fracture when testing with impact velocity of 4.4 m/s at -30°C , i.e. thicker plates did not fracture at these test conditions.

The following parameters were varied (standard values italicized): mould temperature (*14, 40 and 65°C*), melt temperature (*200 and 240°C*) and holding pressure (maximum pressure in profile: *23 and 53 MPa*). Testing at -30°C with impact velocity 4.4 m/s did not show any strong effects of these moulding parameters on the probability of plate fracture. The low mould temperature seemed to reduce the probability, but the statistics are too limited (~ 10 repeated tests for each condition) for a definite conclusion. The injection speed (mould filling time) was not varied for this plate. However, in earlier studies of IM specimens of similar materials [4], applying tensile testing and three-point bending at high loading rates ($1\text{--}2 \text{ m/s}$), it was observed that specimens moulded with high injection speed had a lower strain at break.

Contrary to our findings, Crompton [5] reported a large effect of melt temperature on the falling-weight impact strength (energy corresponding to 50% failure) of IM plates of various PP copolymers at room temperature. IM plates made with high melt temperatures (typically 240°C and above) had impact resistance similar to compression-moulded (CM) plates, and the lower impact resistance of IM plates made with lower melt temperatures was attributed to residual stress and orientation. One reason for the rather low impact strength of Crompton's IM specimens (compared to CM specimens) could be that they were obtained from center-gated parts and struck ca 19 mm from the gate.

Viana et al. [6] also reported significant effects of processing on the peak force and the energy to peak force for a PP copolymer subjected to out-of-plane plate impact testing. Their results were analysed in terms of morphological parameters weighted by factors related to the skin ratio. The peak force increased with increasing molecular orientation and decreasing crystallinity.

On the other hand, Karger-Kocsis et al. [7] reported that the plate impact response of various PP homopolymers was not significantly influenced by the process-induced skin-core morphology, compared to, for example, the impact response for uniaxial tension. Almost the same plate impact results were obtained for as-moulded specimens and specimens with the skin removed by polishing [8].

Note that the microstructure of the skin layer is more complicated in PP compounds, as used in this study, than in PP without fillers and elastomer. In PP compounds, there

are usually separate near-surface concentration profiles for the PP, the mineral filler and the elastomer [9–11].

There is some literature on the effects of injection moulding processing conditions on the uniaxial impact resistance of PP using notched specimens in Charpy, Izod or fracture mechanics tests. Schrauwen et al. [12] measured the Izod impact strength of notched specimens, cut from 1 mm thick IM PP plates, parallel and perpendicular to the flow. The impact resistance was higher for crack propagation perpendicular to the flow, and this resistance increased with increasing thickness of the oriented skin layer (thickest for low injection speed and low melt temperature). Yu et al. [13] reported that the impact properties of IM PP varied along the flow direction, due to variations in skin layer thickness and characteristics, and residual stresses. Van der Meer et al. [14] documented that the lamellar thickness in PP influences the impact resistance, and the lamellar thickness is affected by injection moulding conditions, as well as part geometry and thickness.

3.2. Effect of striker geometry and clamping

In addition to the standard \varnothing 20 mm hemispherical striker, two other striker geometries were also used in some tests at $-30\text{ }^{\circ}\text{C}$ (Fig. 5). With a smaller hemispherical striker (\varnothing 12.7 mm) and an impact velocity of 4.4 m/s, all plates except the thickest (3.9 mm) fractured. The 3.3 mm thick plate was a borderline case, i.e. these plates fractured in some of the repeated tests, but not in all (Fig. 6). With the standard hemispherical striker (\varnothing 20 mm), the 2.4 mm thick plate was the borderline case (Fig. 5, see also Part 1 [1]). The deflection at break was about the same with these two striker diameters. This seems to agree with elastic analysis: If we assume that the fracture criterion is the maximum stress at the center, and apply the approximate elastic bending analysis for an unclamped plate [15], the deflection at break would only be a few percent lower with the \varnothing 12.7 mm striker.

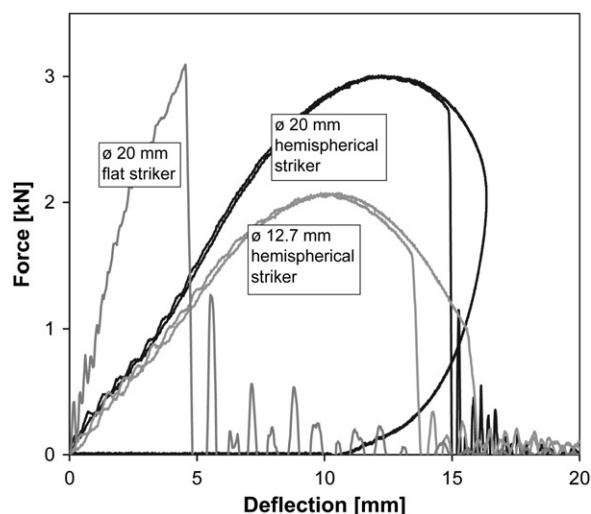


Fig. 5. Effect of striker geometry: Force–deflection curves for 2.4 mm thick plates tested with impact velocity of 4.4 m/s at $-30\text{ }^{\circ}\text{C}$. Data from two repeated tests are shown for the hemispherical strikers.

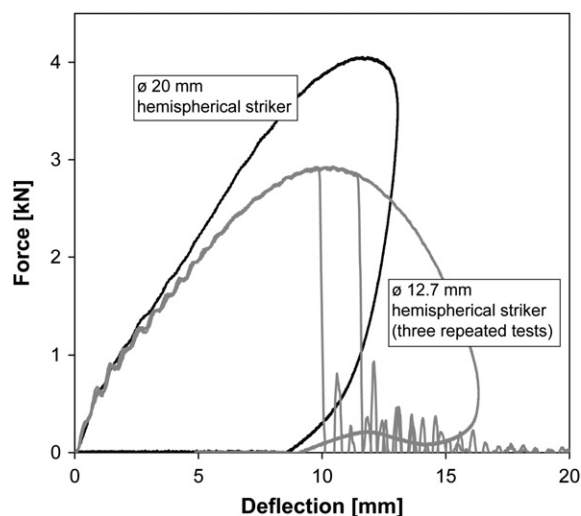


Fig. 6. Effect of striker geometry: Force–deflection curves for 3.3 mm thick plates tested with impact velocity 4.4 m/s at $-30\text{ }^{\circ}\text{C}$. Data from three repeated tests are shown for the smallest striker.

A flat \varnothing 20 mm striker was also used in some tests on 2.9 and 2.4 mm thick plates. With this striker, the plates fractured at quite low deflections (Fig. 5). The fracture was plug-like, and a roughly circular segment was knocked out. The segment area was almost twice the striker area. The segment perimeter followed the striker perimeter on one side, and the clamping perimeter on the other side (the side near the gate, see Fig. 1a). For both plate thicknesses, the maximum force with the flat striker was about the same as with the hemispherical striker with the same diameter.

Some 2.0 mm thick plates were also impacted without being clamped, with impact velocity of 4.4 m/s at $-30\text{ }^{\circ}\text{C}$. The force–deflection curve was close to that of the clamped plate up to a deflection of ~ 5 mm, but had stronger dynamic oscillations. At higher deflections, the force was higher for the unclamped plate, and the peak force was ca 10% higher. The unclamped plates fractured at a lower deflection, so the energy to break was about the same as that of the clamped plate. We attribute the higher force for the unclamped plate to the delocalisation of the deformation. The deformation is more dominated by non-localised elastic and plastic bending than concentrated drawing and yielding under the striker. Two main types of fracture patterns were observed in a series of repeated tests. In about half of the tests, the central crack ran *parallel* to the flow direction (type A, as defined in Part 1 [1]), while in the other tests the central crack ran *perpendicular* to the flow direction (type B [1]). The occurrence of both type A and type B fractures (A–B crossover) indicates that removing the clamping has a similar embrittling effect as reducing the temperature by $\sim 10\text{ }^{\circ}\text{C}$ for the clamped plate (see the description of fracture types and the temperature effect in Part 1 [1]).

3.3. Effect of weld line

By using an exchangeable mould insert, some 3.9 mm thick plates were also filled from two adjacent corners, giving a weld line along the centre of the plate (Fig. 1b).

Some plates were impacted directly on the weld line, and some were impacted ca 10 mm from the weld line. When testing these plates at -30°C with an impact velocity of 4.4 m/s, the weld line caused brittle fracture, and the absorbed energy was significantly reduced compared to the plates without a weld line, see Fig. 7.

Plates struck directly on the weld line (Fig. 8a) had a radial crack along the weld line, but also radial cracks in other directions. The latter cracks probably formed along weak lines perpendicular to local flow-induced orientation. As for the brittle fractures in (thinner) plates without a weld line, there was also a circumferential crack, which was nearly circular in this case. Plates struck ca 10 mm from the weld line (Fig. 8b) only had the circumferential crack. In this case, the maximum stress under the center of the striker did not coincide with a local weak point in the plate. Instead, the fracture initiated where the local stress maximum near the clamp (Fig. 4, position c) met the weld line weakness.

Adverse effects of weld lines have been reported in many studies, mainly based on quasi-static uniaxial tensile testing. Crompton [5] reported a large reduction in the falling-weight impact strength of PP copolymer plates, and the strength reduction was more pronounced for thin plates ($h < \sim 2.5$ mm). Morelli et al. [16] showed that the talc orientation in the weld line plane had a large effect on the tensile-impact resistance of PP/talc. In a study of glass-fiber reinforced PP, Gamba et al. [17] found that a plate impact test was more sensitive to the presence of weld lines than a uniaxial tensile-impact test.

Note that the weld line strength can be somewhat improved by optimising the moulding conditions. There are also special processing and mould technologies (some patented) that can improve the weld line strength further [18].

3.4. Effect of surface texture

By using an exchangeable mould insert, 2.4 mm thick plates were also made with one side having a surface

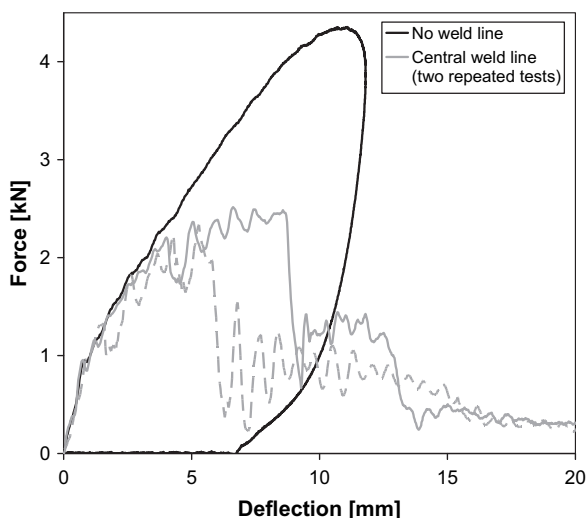


Fig. 7. Effect of weld line: Force–deflection curves for 3.9 mm thick plates tested with impact velocity of 4.4 m/s at -30°C . Data from two repeated tests are shown for plates impacted directly on the weld line.

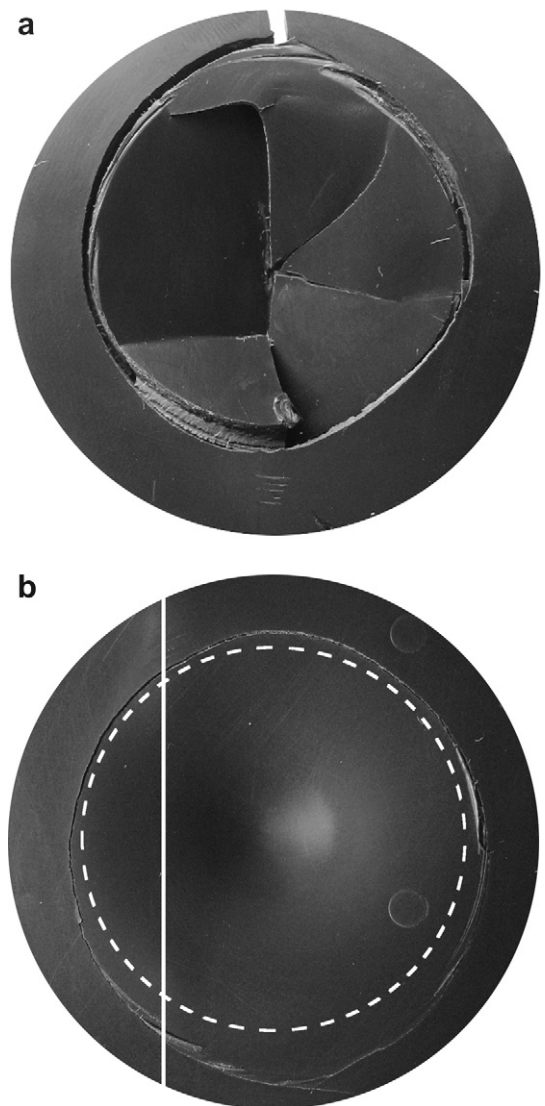


Fig. 8. Photos of 3.9 mm thick plates with weld line after testing with impact velocity of 4.4 m/s at -30°C . (a) Plate struck directly on the weld line (weld line vertical in the photo). (b) Plate struck ca 10 mm from the weld line. The weld line is indicated by the solid line, while the annular clamping is indicated by the dashed line.

texture. This texture is one of the coarsest types used for bumper covers (Fig. 2). Textured plates were tested at -30°C .

When striking the textured side, the force–deflection curve was almost the same as for the standard plates. However, when striking the untextured side (textured side in tension under the striker), the plates showed a brittle response with lowered impact energy, both at 3.0 and 4.4 m/s, see Fig. 9. Note that the absorbed energy (energy to break) was lower at 4.4 m/s than at 3.0 m/s, indicating that there is a maximum in absorbed energy as a function of impact velocity. For the standard plates, the absorbed energy was higher at 4.4 m/s than at 3.0 m/s, even when the plate fractured at 4.4 m/s (as in one of the repeated tests in Fig. 5)

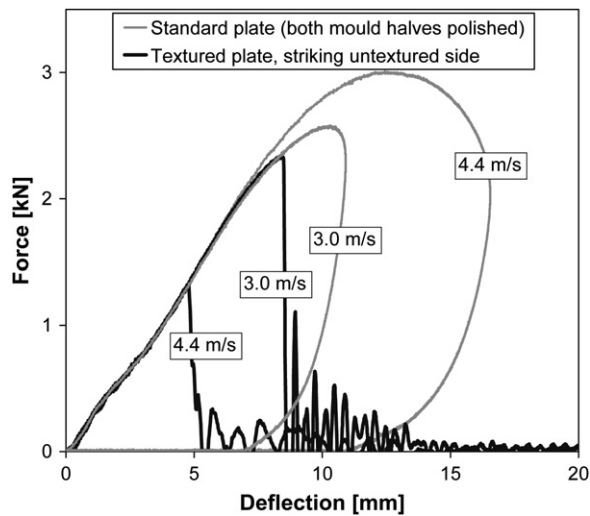


Fig. 9. Effect of surface texture: Force–deflection curves for 2.4 mm thick plates tested with indicated impact velocities at -30°C .

When striking the untextured side, a central crack formed and propagated parallel to the flow direction, as for the type A fracture mentioned at the end of Section 3.2. When striking the textured side, a shallow circumferential crack formed on the textured side near the clamp (Fig. 4, position c), but no discontinuity was observed in the force–deflection curve. In both cases, the cracks were probably initiated by stress concentrations in the surface texture (Fig. 2).

Crompton [5] reported the effect of different surface textures on the falling-weight plate impact strength for three different PP grades at room temperature. The impact strength was greatly reduced when striking the untextured side, especially for the sharpest textures, and there were some differences between the materials. Moore and Turner [19] tested a plate with (moulded) grooves in one direction and varied the groove direction relative to the flow direction in the plate. The grooves induced brittleness, but an unexpected trend was observed; the absorbed energy was highest with the flow direction along the grooves.

3.5. Effect of paint

Some 2.9 mm thick plates were painted with a commercial paint system on one side (see Section 2) and struck against the painted side with different impact velocities. The paint induced brittle fracture at -30°C , but no adverse effect of the paint was observed at 20°C .

With low impact velocities (1 m/s) at -30°C no effect of the paint was observed. However, with impact velocities of 2 and 3 m/s, circumferential cracks with diameter 40–45 mm formed on the impacted side (Fig. 4, position c), but stopped at a certain depth. With even higher impact velocity (4.4 m/s) this circumferential crack ran through the plate. The force–deflection curves are shown in Fig. 10.

When a crack in the paint layer reaches the coating/substrate interface, it has several alternative failure

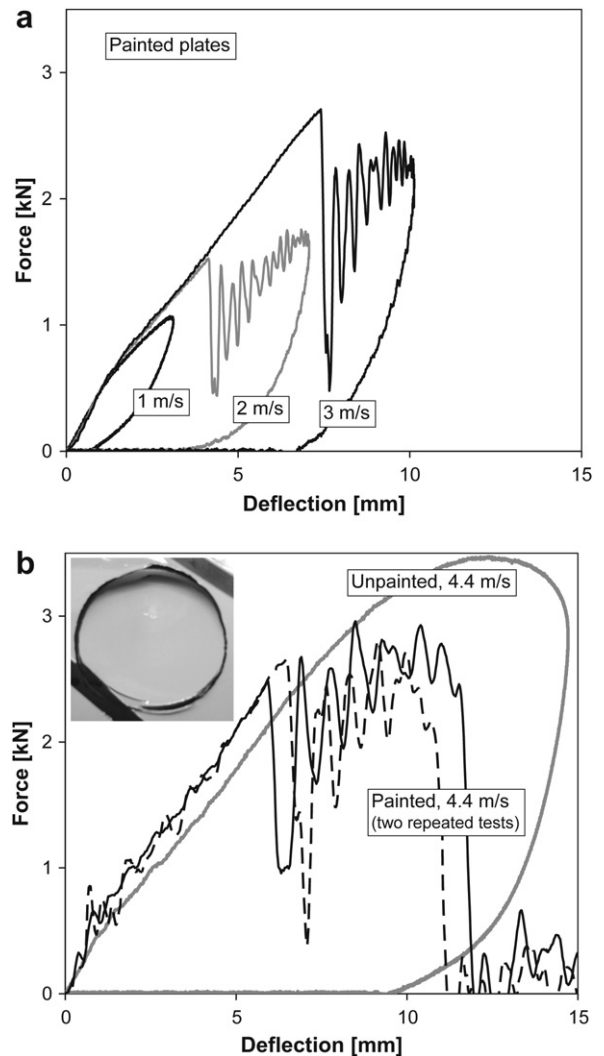


Fig. 10. Effects of paint: Force–deflection curves for 2.9 mm thick plates tested with indicated impact velocities at -30°C . The inset shows a fractured painted plate tested with impact velocity of 4.4 m/s (the radius of the circumferential crack is 22 mm).

modes [20], and one possibility is entering the substrate, causing substrate failure. This embrittlement effect is, for example, commonly observed for polymers with strongly bonded hard (scratch resistant) coatings and, in these cases, the polymer toughness and the coating toughness, as well as the interface properties, must be optimised [21]. Different mechanisms have been proposed for the embrittlement [22], and recent fracture mechanics modelling studies have explained some of the features [22,23]. The brittle–ductile transition of the coating itself can be related to the plastic zone radius of the coating (r_p) relative to the coating thickness (h_c) [19]. The former increases with temperature, and the coating is ductile for $r_p/h_c > \sim 1$.

The cracks in our study probably initiate in the clearcoat (the top layer), which is the hardest paint layer. The clearcoat material, a polyurethane thermoset, is optimised with

regard to hardness vs. flexibility. The adhesion promoter is responsible for the adhesion between the injection-moulded surface and the basecoat and could, therefore, have a role as the crack enters the injection-moulded substrate. The adhesion between the adhesion promoter (chlorinated polyolefin) and the injection-moulded PP compound is reported to be related to the elastomer content at or near the surface of the latter, and this content is influenced by processing conditions, and varies along the flow path [9]. Finally, it should be noted that the paint system used in this study is considered to be one of the best on the market and painted parts pass standard quasi-static bending tests at -30°C .

With a similar plate impact test, Jones et al. [24] reported results for two paint systems on PP. A “traditional” paint system increased the ductile–brittle transition temperature, but not a system with a polyurethane top coat. Woods et al. [25] compared two paint systems on plates of different undisclosed thermoplastic materials. One of the paint systems caused embrittlement at -30°C . The failure behaviour was modelled with finite element analysis using a failure criterion based on maximum principal stress.

4. Conclusions

We have studied some aspects of the low-velocity, low-energy impact response of an industrially important polymer; mineral and elastomer modified polypropylene. The plate impact test was chosen due to its relevance for impact events commonly occurring during the service life of injection-moulded components.

In this paper we have investigated the effects of moulding conditions, striker geometry, clamping, plate surface roughness, melt flow weld lines and paint. We have focused on the impact performance at -30°C with impact velocities in the range 1.0–4.4 m/s. Our main findings are summarized below:

- The occurrence of brittle fracture in plate impact tests was affected by load distribution (via striker geometry and clamping), surface texture, weld lines and paint. Brittle fracture was induced to varying degrees by these factors.
- In general, plates with thickness below a certain critical thickness showed brittle fracture [1]. There was also a critical impact velocity above which brittle fracture occurred. The factors studied in this paper affected the critical thickness and the critical impact velocity.
- Reducing the striker hemisphere diameter, or changing to a flat striker, induced brittle fracture.
- Removing the annular clamping led to a more brittle response. The deformation was more dominated by non-localised elastic and plastic bending than concentrated drawing and yielding under the striker.
- Plates with a weld line were more brittle than standard plates. The distance between the impact point and the weld line is an important factor.
- The surface texture caused brittle fracture when impacting the untextured side (textured side in tension under the striker). The reduction in absorbed energy

(compared to the standard plate) was sensitive to the impact velocity.

- The paint induced brittle fracture at -30°C , but no adverse effect of the paint was observed at 20°C .
- The injection moulding processing conditions assessed in this study did not have a strong influence on the plate impact response.

Acknowledgment

This study and the PhD studentship of Hamid Daiyan were funded by the Research Council of Norway (BIA programme) and Plastal AS.

References

- [1] H. Daiyan, E. Andreassen, F. Grytten, O.V. Lyngstad, T. Luksepp, H. Osnes, Low-velocity impact response of injection-moulded polypropylene plates – part 1: effects of plate thickness, impact velocity and temperature, *Polym. Test.* 29 (6) (2010) 648.
- [2] F. Grytten, H. Daiyan, M. Polanco-Loria, S. Dumoulin, Use of digital image correlation to measure large-strain tensile properties of ductile thermoplastics. *Polym. Test.* 28 (6) (2009) 653.
- [3] ISO 6603-2, Plastics – Determination of Puncture Impact Behaviour of Rigid Plastics – Part 2: Instrumented Impact Testing, International Organization for Standardization; 2000.
- [4] E. Andreassen, H. Daiyan, F. Grytten, O.V. Lyngstad, R.H. Gaarder, E.L. Hinrichsen, in: Proceedings of the 24th Annual Meeting of the Polymer Processing Society, Salerno, Italy, Polymer Processing Society; 2008.
- [5] T.R. Crompton, *Polymer Reference Book*. Smithers Rapra Technology, 2006, (Chapter 18).
- [6] J.C. Viana, A.M. Cunha, N. Billon, Experimental characterization and computational simulations of the impact behavior of injection-molded polymers. *Polym. Eng. Sci.* 47 (4) (2007) 337.
- [7] J. Karger-Kocsis, D.E. Mouzakis, G.W. Ehrenstein, J. Varga, Instrumented tensile and falling weight impact response of injection-molded alpha- and beta-phase polypropylene homopolymers with various melt flow indices. *J. Appl. Polym. Sci.* 73 (7) (1999) 1205.
- [8] J. Karger-Kocsis, E. Moos, I. Mudra, J. Varga, Effects of molecular weight on the perforation impact behavior of injection-molded plaques of alpha- and beta-phase isotactic polypropylenes. *J. Macromol. Sci., Phys.* B38 (5–6) (1999) 647.
- [9] K.Q. Deng, N. Felorzabih, M.A. Winnik, Z.H. Jiang, Z.H. Yin, Y.Q. Liu, P.V. Yaneff, R.A. Ryntz, Influence of position and composition on adhesion to injection-molded TPO plaques as model automotive parts. *Polymer* 50 (21) (2009) 5084.
- [10] H. Tang, D.C. Martin, Microstructural studies of interfacial deformation in painted thermoplastic polyolefins (TPOs). *J. Mater. Sci.* 37 (22) (2002) 4783.
- [11] B.D. Pennington, R.A. Ryntz, M.W. Urban, Stratification in thermoplastic olefins (TPO); photoacoustic FT-IR depth profiling studies. *Polymer* 40 (17) (1999) 4795.
- [12] B.A.G. Schrauwen, L.C.A. Von Breemen, A.B. Spoelstra, L.E. Govaert, G.W.M. Peters, H.E.H. Meijer, Structure, deformation, and failure of flow-oriented semicrystalline polymers. *Macromolecules* 37 (23) (2004) 8618.
- [13] X.F. Yu, H. Wu, J. Li, S.Y. Guo, J.H. Qiu, Structure and property of injection-molded polypropylene along the flow direction. *Polym. Eng. Sci.* 49 (4) (2009) 703.
- [14] D.W. van der Meer, B. Pukanszky, G.J. Vancso, On the dependence of impact behavior on the crystalline morphology in polypropylenes. *J. Macromol. Sci., Phys.* B41 (4–6) (2002) 1105.
- [15] P.E. Reed, Elastic analysis of the flexed plate impact test. *J. Strain Anal. Eng.* 25 (4) (1990) 207.
- [16] C.L. Morelli, J.A. de Sousa, A.S. Pouzadla, Assessment of weld line performance of PP/talc moldings produced in hot runner injection molds. *J. Vinyl Add. Technol.* 13 (3) (2007) 159.
- [17] M.M. Gamba, A.S. Pouzada, P.M. Frontini, Impact properties and microhardness of double-gated glass-reinforced polypropylene injection moldings. *Polym. Eng. Sci.* 49 (9) (2009) 1688.
- [18] B. Fisa, A. Meddad, *Weldlines*. in: J. Karger-Kocsis (Ed.), *Polypropylene: An A–Z Reference*. Kluwer Publisher, 1999.
- [19] D.R. Moore, S. Turner, *Mechanical Evaluation Strategies for Plastics*. CRC Press, 2001, (Chapter 11).

- [20] S.-R. Kim, J.A. Nairn, Fracture mechanics analysis of coating/substrate systems: part i: analysis of tensile and bending experiments. *Eng. Fract. Mech.* 65 (5) (2000) 573.
- [21] F. Ramsteiner, T. Jaworek, M. Weber, S. Forster, Scratch resistance and embrittlement of coated polymers. *Polym. Test.* 22 (4) (2003) 439.
- [22] M.-A. Godart, P. Leever, Effect of skin fracture on failure of a bilayer polymer structure. *Int. J. Fracture* 148 (4) (2007) 315.
- [23] P.S. Leever, L. Moreno, Surface layer stiffness effects on fracture of polymer multilayers: a linear elastic model. *Eng. Fract. Mech.* 72 (6) (2005) 947.
- [24] D.P. Jones, D.C. Leach, D.R. Moore, *Plast. Rubber Process Appl.* 6 (1) (1986) 67.
- [25] J. Woods, S. Patterson, C. Roberts, Predicting impact performance of painted thermoplastic exterior body panels. *SAE Trans.* 110 (5) (2001) 541.

Paper 3

F. Grytten, H. Daiyan, M. Polanco-Loria, S. Dumoulin

Use of digital image correlation to measure large-strain tensile properties of ductile thermoplastics

Polymer Testing, Volume 28, Issue 6, 2009



Test Method

Use of digital image correlation to measure large-strain tensile properties of ductile thermoplastics

F. Grytten^{a,*}, H. Daiyan^a, M. Polanco-Loria^b, S. Dumoulin^b^aSINTEF Materials and Chemistry, Department of Synthesis and Properties, PB 124 Blindern, NO-0314 Oslo, Norway^bSINTEF Materials and Chemistry, Department of Applied Mechanics and Corrosion, NO-7465 Trondheim, Norway

ARTICLE INFO

Article history:

Received 2 April 2009

Accepted 13 May 2009

Keywords:

Polypropylene

Digital image correlation

Plasticity

Volumetric strain

ABSTRACT

This paper presents an experimental investigation of the mechanical behaviour of a talc and elastomer modified polypropylene compound subjected to large strains. 3D digital image correlation with two cameras and stereo-vision was used to determine full-field displacements during uniaxial tensile tests on specimens with rectangular cross-section. Local strains were derived from the displacement field and used to calculate the current cross-sectional area of the specimen during the whole loading process. Points on the true stress–strain curve (Cauchy stress versus logarithmic strain) were then calculated from the data. Volume dilatation was separated into elastic and plastic parts through tests where the specimens were unloaded after varying degree of stretching. The unloading events were also used to investigate damage evolution as function of plastic straining.

© 2009 Elsevier Ltd. All rights reserved.

1. Introduction

Ductile thermoplastics are increasingly being used in automotive components to reduce weight and enhance passenger and pedestrian safety. A detailed knowledge about the behaviour of these materials under severe deformation (e.g. crash accidents) is required in order to fully utilize their energy absorbing capabilities in a robust and crashworthy design.

The static uniaxial tension test is probably the simplest and most widely used mechanical test today. This test is used to determine Young's modulus, Poisson's ratio, yield and tensile strength of the material, work hardening curve, shape of yield locus, parameters of ductile failure criteria, etc. Since plastic deformation and ductile fracture of thermoplastics are depending on hydrostatic pressure, the tensile tests are needed for a complete understanding of the material behaviour and cannot simply be replaced by e.g. compression tests. Thus, the challenges associated with

measurements of the true tensile stress–strain relation of the material must be overcome.

During a uniaxial tension test, many engineering polymers start to neck at relatively small strains and have a significant energy absorbing capacity after necking. The onset of necking renders conventional extensometers inadequate since the stress and strain fields become heterogeneous. Further, the volumetric strain can be significant for ductile thermoplastics. Thus, calculations of true stress (Cauchy stress) based on the approximation of constant volume yields overestimated results for these materials. Therefore, numerous attempts have been made over the years to measure both the longitudinal and transverse strain locally.

Different video-based techniques have been used in many of the reported attempts to measure the true stress–strain relation of polymers. G'Sell et al. [1] developed an optical technique where seven dots on one side of a rectangular bar were tracked. In order to localize the strains, G'Sell et al. introduced a slight reduction of the cross sectional area in the zone where the markers were applied. The displacement of these dots was used to calculate the true axial and transverse strain. True stress was calculated

* Corresponding author. Tel.: +47 93012077; fax: +47 22067350.

E-mail address: frode.grytten@sintef.no (F. Grytten).

using the measured transverse strain and assuming transverse isotropy. In this way they omitted the assumption of constant volume. Mohanraj et al. [2] applied the same technique with a smaller reduction of the cross sectional area. Gloaguen and Lefebvre [3] measured the separation of ink marks on a dumbbell-shaped specimen. They used two cameras to measure strains on two faces simultaneously. This procedure did not require any assumption of constant volume or transversal isotropy.

The spatial resolution of the aforementioned procedures is relatively poor. Digital image correlation (DIC) has improved the spatial resolution of optical full-field strain measurements. Parsons et al. [4,5] obtained strain fields on two sides of rectangular tensile specimens with this technique using one camera and a right-angle prism. De Almeida et al. [6] recently used one camera and a mirror to measure strain fields on both the front and the lateral side of a specimen simultaneously, while Fang et al. [7] used two cameras watching one side each. No isochoric or isotropic assumptions are needed with these latter three setups. However, all the methods mentioned above are based on the assumption that the strains measured on the surface of the specimen are representative of the strains throughout the thickness of the specimen, i.e. the reduction of width measured on the front surface is representative for the width reduction throughout the thickness.

A novel methodology including 3D DIC with two cameras and stereo-vision has been developed in the present study in order to determine full-field displacements during uniaxial tensile tests on specimens with rectangular cross-section. Single camera DIC systems are limited to planar specimens that experience little or no out-of-plane motion. By the use of a second camera observing the surface from a different direction, the three-dimensional coordinate of any point can be found by triangulation. Then, by comparing the changes between an initial set of images and a set taken after load is applied, full-field three-dimensional displacements can be measured.

The aim of the current work is to establish a methodology to determine the large-strain tensile behaviour of ductile thermoplastic materials. For this purpose, a talc and elastomer modified polypropylene compound is used to demonstrate the applicability of the proposed techniques.

2. Experimental

2.1. Material and sample preparation

The material investigated in this study is a commercial impact-modified polypropylene used for injection moulded automotive exterior parts. Namely a 20% mineral (talc) filled and elastomer modified polypropylene compound. Tensile test specimens (type 1A of the ISO 527-2:1993 standard) were injection moulded with processing conditions based on ISO 294-1:1996 and ISO 1873-2:2007. The thickness of the specimens was 4 mm. A random black and white speckle pattern was applied to both the front and lateral side of the specimen prior to testing using mat spray paint.

2.2. Experimental procedure

Tensile tests were carried out in a Zwick Z250 universal test machine at 23 °C using constant cross-head speeds of 10 and 100 mm/min. The length of the narrow portion of the specimen was 80 mm, resulting in nominal strain rates of 0.0021 and 0.021 s⁻¹, respectively. The load was measured with a 2.5 kN load cell and the signal was logged using a 12 bit National Instruments DAQCard 6062E.

A commercial Vic3D digital image correlation (DIC) system from Limes [8] and Correlated Solutions [9] was used to measure the displacement field during loading. Two high resolution cameras (2452 × 2052 pixels) with Pentax 75 mm f/2.8 lenses were used. The cameras were mounted on a tripod and arranged so that two adjacent faces of the specimen were visible to both cameras simultaneously, as illustrated in Fig. 1. This arrangement of the cameras allows measurement of out-of-plane displacement in addition to in-plane strains on the specimen surface. However, it results in a slightly lower spatial resolution in the transverse directions than in the longitudinal direction due to the acute angle between the optical axis and the surfaces. Further, cross sections in the specimen will in general not be aligned with rows of pixels in the captured images (see Fig. 2). Thus, points in a certain cross section have to be identified based on their 3D coordinate in the object coordinate system and not based on the pixel coordinates in the image coordinate system. These points are

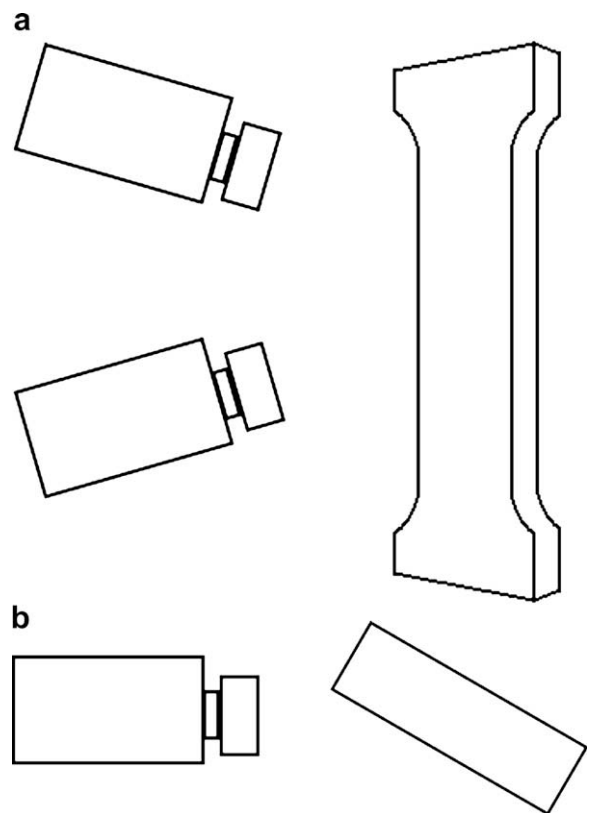


Fig. 1. Placement of cameras relative to specimen, side view (a) and top view (b).

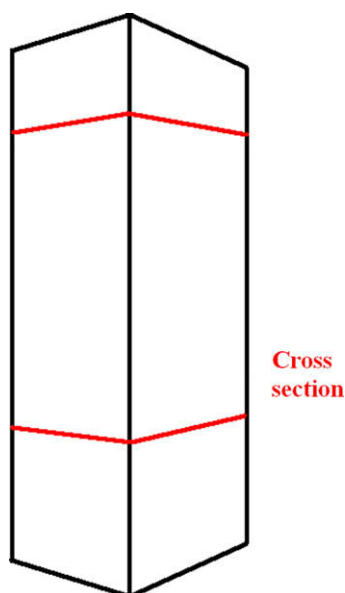


Fig. 2. Cross-sections are generally not aligned with rows of pixels, i.e. they do not form horizontal lines in the image.

required to calculate the current cross sectional area and the true stress.

Unlike 2D DIC systems which don't require any calibration for strain calculations, 3D DIC systems require a system calibration for both strain and displacement calculations [10]. A complete system calibration was run before each experiment to ensure accurate results. A plate with a pre-defined pattern of circular dots was moved around (translated and rotated) in the measurement area while several synchronized calibration images were acquired by both cameras (see Fig. 3). Since the spacing between the dots on the calibration target was known, all key parameters of the pin-hole projection based stereo-vision model could be determined, see Fig. 4. These

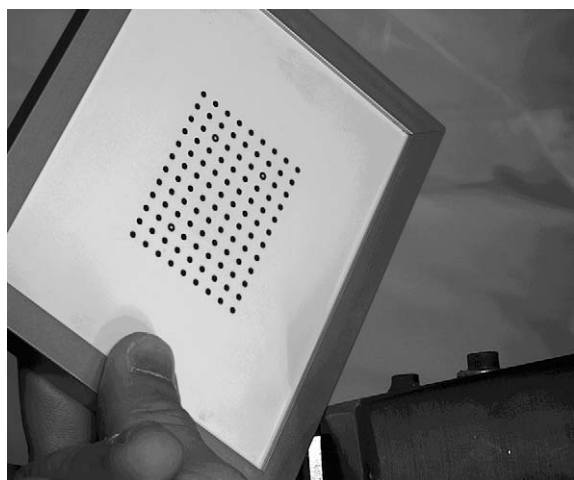


Fig. 3. Calibration target with grid of circular dots.

parameters include the distance from the projection centre to the sensor plane for both cameras, the coordinates of the point where the optical axis intersects the sensor for both cameras, the scale factors relating pixel coordinates to metric distances in both principal direction of the sensor coordinate system and, finally, the relative placement and orientation of the two cameras. A more detailed description of the calibration procedure can be found in e.g. Tiwari et al. [11].

Digital image correlation was carried out using Vic3D 2007, a commercial 3D DIC software developed by Correlated Solutions. An "area of interest" (AOI) was defined for each of the two faces visible to both cameras, see Fig. 5. A subset size of 25 by 25 pixels and a step size of one pixel were used for the correlation. A coordinate transformation was performed (see Fig. 5 for definition) before data on initial coordinates for each pixel in the AOIs, displacement of each point and local in-plane Green–Lagrange strain components were exported to ASCII-files. Further post-processing of the crude data was carried out using in-house MatLab [12] scripts and will be explained in the following section.

2.3. Preliminary tests and results

Preliminary tests where the two cameras only recorded images of the front of the specimen revealed that the cross section of the specimen was not perfectly rectangular, but in fact concave as seen in Fig. 6. However, the deviation was relatively small (the thickness in the centre was about 2% smaller than the thickness near the side of the specimen). The tests further showed that the deformation during loading was not only inhomogeneous in the length direction, but also varied along the width and thickness directions. The displacement in the direction perpendicular to the surface could be as much as 40% larger for points at the centre than for points near the edge (see Fig. 6). This seems to contradict the assumptions that the surface strains are representative for the strains throughout the cross section and that the strain and stress are homogeneous throughout the cross section. However, the material will still be treated as an "equivalent homogeneous polymer" in the following investigation of the macroscopic behaviour.

2.4. Calculating true stress

While the local strains can be measured, there is no way to determine the local stress. An averaged, or macroscopic, Cauchy stress for the whole cross section must therefore be calculated from the total load and the current cross-sectional area. The current cross sectional area was calculated in two different ways in the present study. The first approach was to use the transverse strain measured by DIC on the surface of the specimen, which is equivalent to what was done by e.g. Parsons et al. [4,5], De Almeida et al. [6] and Fang et al. [7]. The second approach was to use the normal displacement of points on the two visible surfaces. Both algorithms were implemented as MatLab scripts and will be described in the following.

The data exported as ASCII files from Vic3D was ordered by pixel coordinates but, as shown in Fig. 2, it is impossible

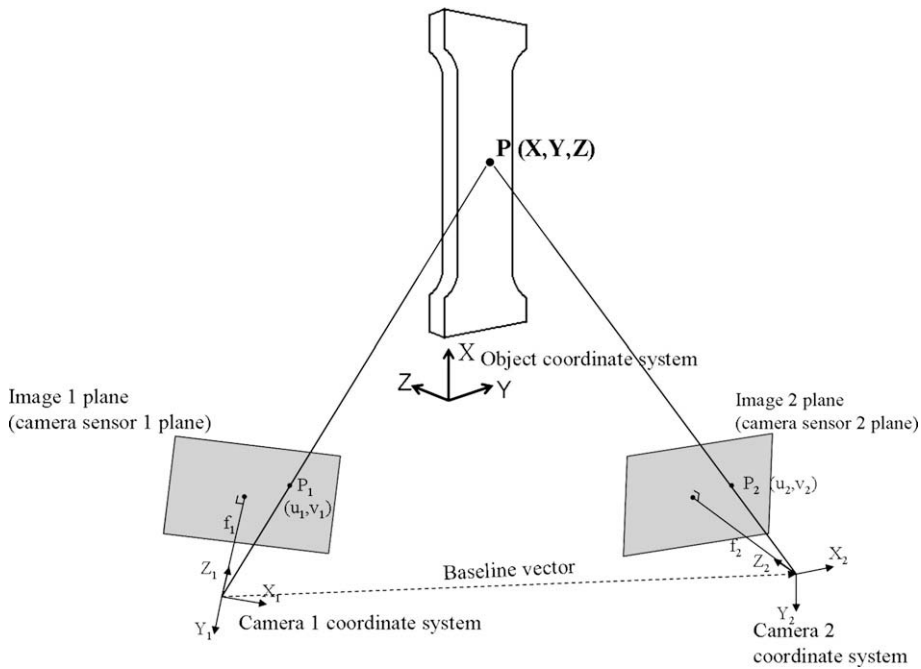


Fig. 4. Schematic of a two-camera stereo-vision system based on the pinhole projection model.

to align all cross sections of the sample with rows of pixels. Therefore, pixels within the same cross section first had to be identified. This was done by searching for all pixels with a certain x-coordinate ± 0.5 mm (according to the coordinate system shown in Fig. 5, where x , y and z are principal directions of strain). The average logarithmic strain in the longitudinal direction in any cross section can be calculated from the average Green–Lagrange strain as

$$\epsilon_{xx} = \frac{1}{2} \ln(1 + 2\bar{E}_{xx}) \quad (1)$$

Assuming that the transverse strains measured on the surface are representative of the strains throughout the cross section, the macroscopic Cauchy stress in the longitudinal direction can be calculated in any cross section as

$$\sigma_{xx} = \frac{F}{A} = \frac{F A_0}{A_0 A} = \frac{F w_0 t_0}{A_0 w t} = \frac{F}{A_0} \frac{1}{\sqrt{1 + 2\bar{E}_{yy}} \sqrt{1 + 2\bar{E}_{zz}}} \quad (2)$$

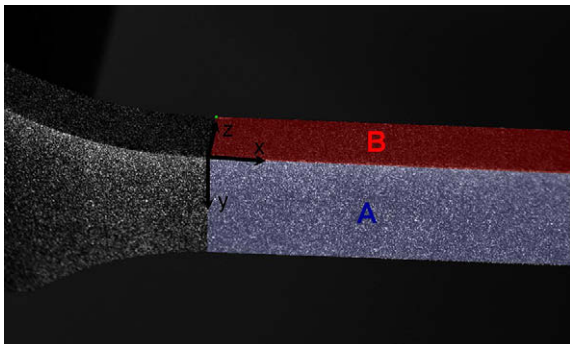


Fig. 5. AOIs for digital image correlation and coordinate system used in post-processing.

where σ_{xx} is the Cauchy stress, F is the current force, A and A_0 are the current and initial cross sectional area, w and w_0 are the current and initial width, t and t_0 are the current and initial thickness and \bar{E}_{yy} and \bar{E}_{zz} are the average Green–Lagrange strain in the transverse directions for all points in the current cross section on face A and B, respectively. Curve A + B in Fig. 7 was calculated using data from the most strained cross section and Eq. (2) directly. Curve A was calculated assuming isotropy and only using transverse strains measured on face A (see Fig. 5), i.e. $\bar{E}_{zz} = \bar{E}_{yy}$. Similarly, Curve B was calculated from transverse strains measured on face B. As can be seen, the three curves are in good agreement. The maximum difference in stress between the two curves obtained assuming isotropy is about 10%. Note that the end of the stress-curves presented in this paper does not imply failure as tests were stopped at arbitrary strains.

As an alternative to using the transverse strains measured on the two faces, the average normal displacement of the two faces can be used to calculate the Cauchy stress as

$$\sigma_{xx} = \frac{F}{A} = \frac{F}{(w_0 - 2\bar{V})(t_0 - 2\bar{W})} \quad (3)$$

where \bar{V} is the average normal displacement of points in the current cross section on face B and \bar{W} is the average normal displacement of points on surface A. Fig. 8 shows the stress–strain relation calculated using Eq. (3). Again, curves A + B, A and B are calculated based on data from both sides, face A and face B, respectively. A greater difference between the curves (approximately 40%) was observed when using this latter approach than when using the strain based procedure. Note that this method can be sensitive to play in the fixtures and rigid body movement.

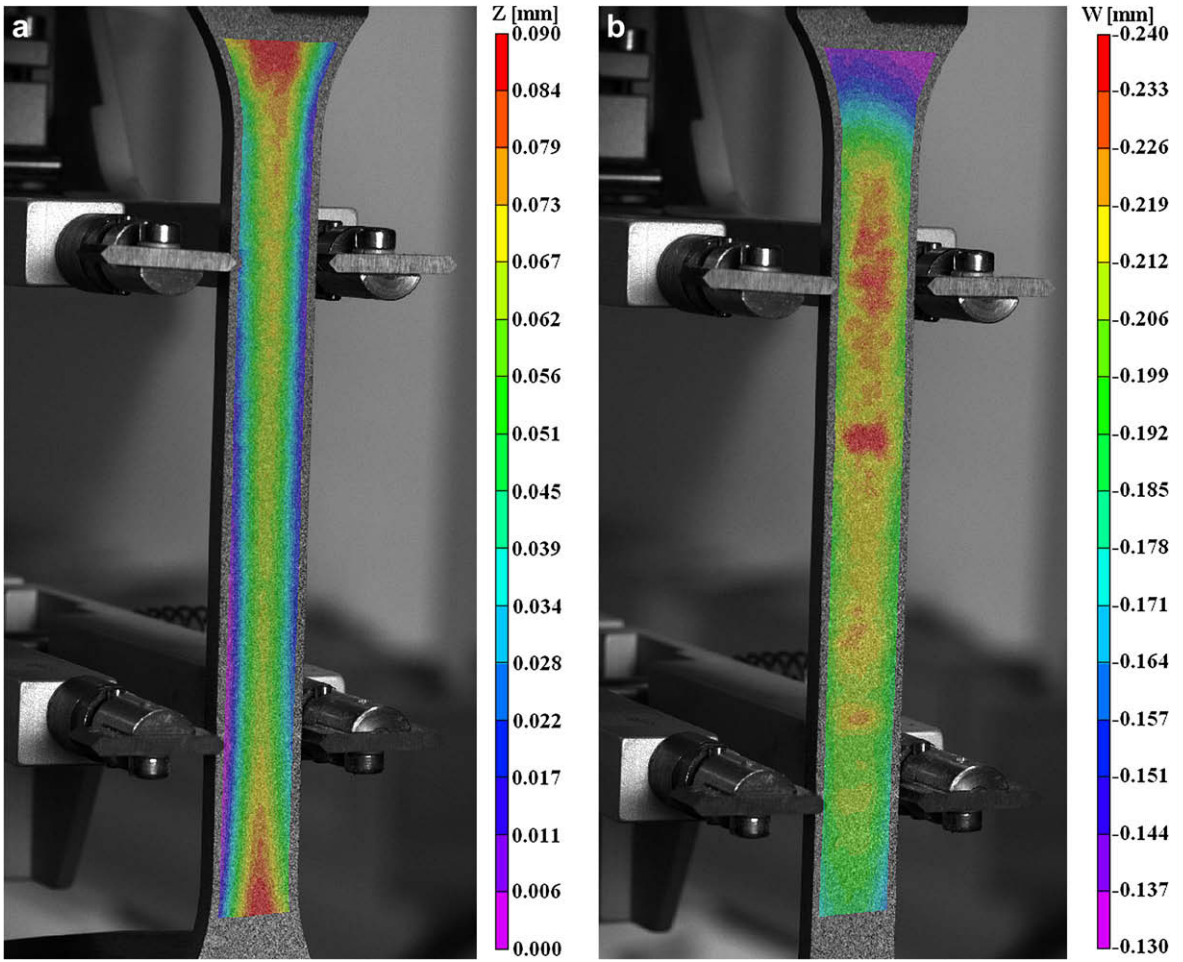


Fig. 6. Preliminary tests showed that the injection moulded specimens initially had concave cross sections (a), and that during testing the normal displacement was not homogeneous throughout the width of the sample (b).

In theory, the rigid body movement could be calculated and subtracted from all the calculated displacements so that the remaining displacements must be caused by deformation. This was not attempted in the present study, but the rigid

body movements were checked and found to be small compared to the specimen dimensions.

The two approaches described above (using data from both faces) are compared in Fig. 9, and a very good agreement is observed. The maximum difference in stress level is

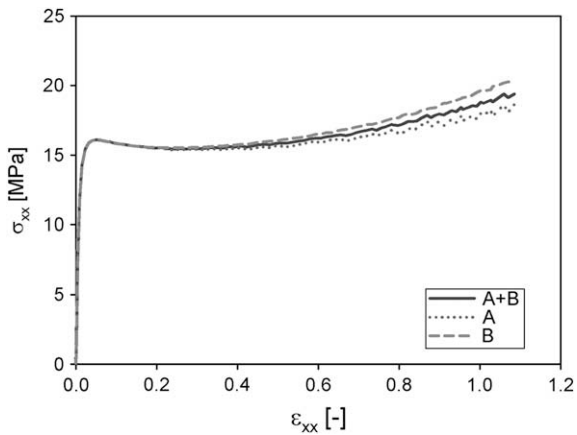


Fig. 7. True stress-strain curves calculated based on measured transverse strains.

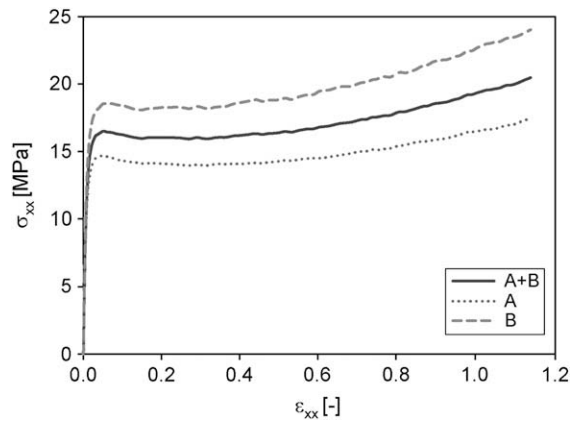


Fig. 8. True stress-strain curves calculated based on measured normal displacements.

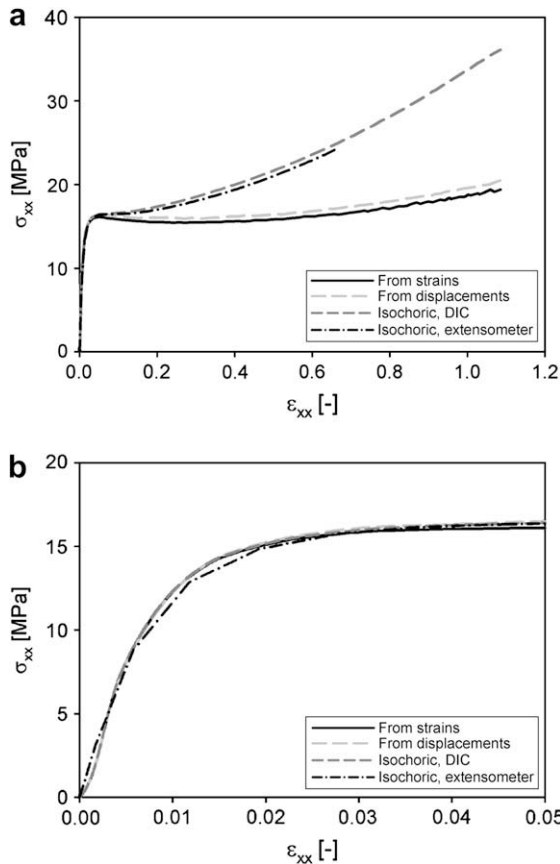


Fig. 9. Comparison of various methods to calculate the true stress–strain relation to large strains (a) and close-up at small strains (b).

approximately 6%. As can be seen, the initial loading is approximately linear until the onset of plastic yielding. Then, a maximum is reached at a strain level of about 5%, and the material exhibits softening until 30% strain, after which work hardening is observed again. Stress–strain curves based on the isochoric assumption and longitudinal strains from DIC and a conventional extensometer are also shown in the figure. When comparing the curve based on longitudinal strain measured locally to the two curves calculated with the true cross sectional area, it becomes evident that volumetric strains are significant and that the isochoric assumption is invalid. The curve based on extensometer data was expected to deviate from the other curves after the onset of necking. However, Fig. 9 shows that the extensometer based curve follows the curve based on DIC measurements and isochoric assumption quite well even after Considère's criterion [13] is met. Fig. 10 shows that the strains are inhomogeneous. Therefore, the most likely reason for the seemingly good agreement between the curves obtained with the isochoric assumptions is that the material behaviour is close to “perfectly plastic”, i.e. the force is almost constant during the plastic straining. If a material is “perfectly plastic”, then the nominal flow stress will be constant, and even an incorrect measured strain would give a point on the real stress–strain curve.

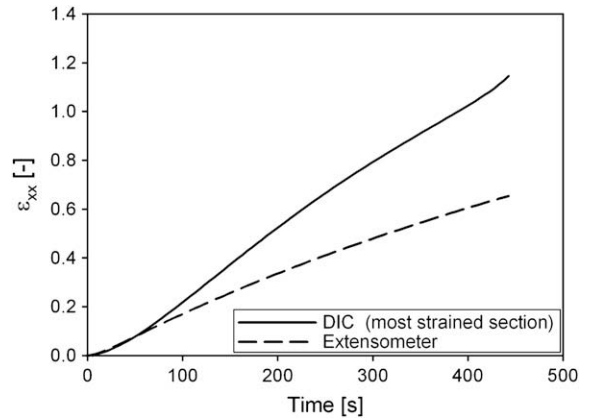


Fig. 10. Strain versus time from extensometer and DIC.

The good agreement between the two isochoric curves in Fig. 9 (a) must therefore be regarded as a coincidence.

2.5. Effects of strain-rate and unloading

Tests with increased crosshead velocity were conducted to assess the effect of strain rate. Fig. 11 shows a comparison of the stress–strain curves obtained with crosshead velocities 10 and 100 mm/min (note that the end of a curve does not imply fracture). The material seems to be linearly elastic (the viscoelastic effect is small in the current range of strain rates). However, the material is clearly viscoplastic. The flow stress increases by approximately 15% when the strain-rate is increased from 0.002 to 0.02.

Some tests were carried out with unloading after various degrees of loading, using a constant crosshead velocity of 10 mm/min. Fig. 12 shows three stress–strain curves with unloading after 21%, 56% and 84% total logarithmic strain, respectively. It can be seen that the unloading is non-linear, and that the non-linearity is more pronounced after higher degrees of stretching before unloading. A test with loading, unloading and reloading revealed elastic hysteresis (see Fig. 13), i.e. the material

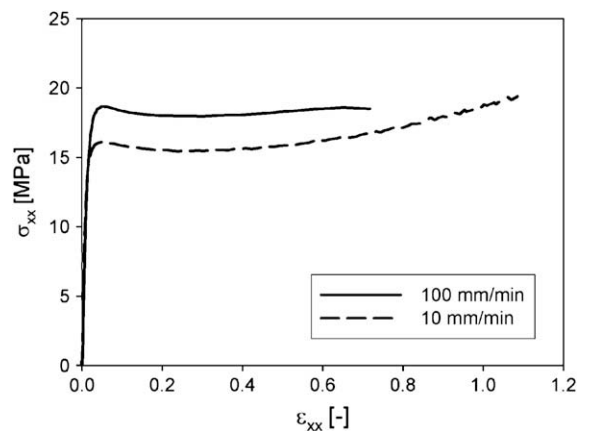


Fig. 11. The current material exhibits viscoplastic behaviour.

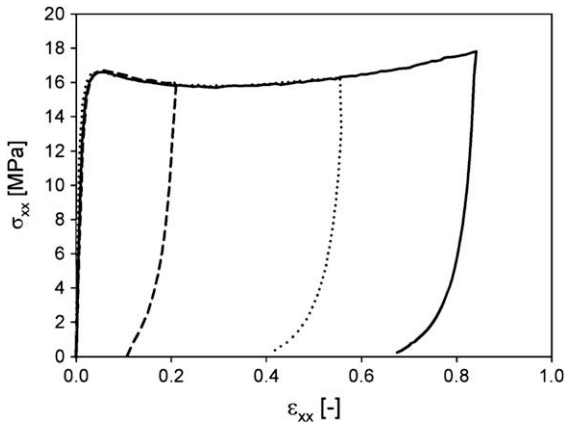


Fig. 12. Tests with unloading after various degrees of loading.

exhibits viscoelastic behaviour. This is in contrast to what was seen during the initial loading at different rates.

2.6. Measurements of transverse and volumetric strains

Fig. 14 (a) shows “Poisson’s ratio” calculated from the total contraction (elastic and inelastic) on the two faces as function of the total longitudinal strain. Inelastic volumetric strains were calculated from the tests with loading followed by unloading. By comparing the volume at maximum load to the volume in the unloaded state, the volumetric strains could be separated into elastic and inelastic parts. The volumetric strains are shown as function of permanent longitudinal strain in Fig. 14 (b). As can be seen, the change in volume is significant and a large part of it is inelastic. The ratio between the plastic strain in the transverse directions and the longitudinal direction can provide valuable information about the plastic potential function if non-associated flow is assumed, or about the yield function itself if associated flow is assumed. This information is especially important when formulating and calibrating yield functions and plastic potentials where plastic volumetric strains or anisotropy is included.

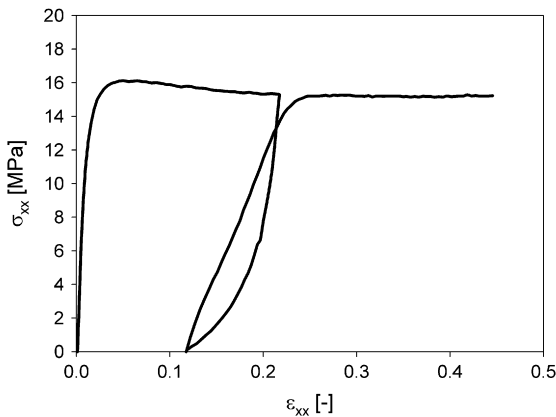


Fig. 13. Stress–strain curve from a test with loading, unloading and reloading.

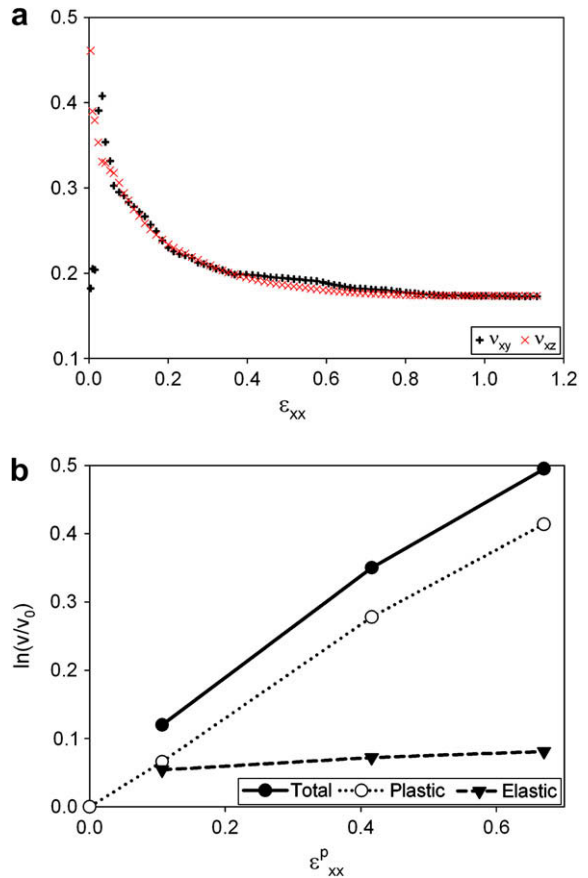


Fig. 14. “Poisson’s ratio” as function of the total longitudinal strain (elastic and plastic) (a) and volumetric strains as function of permanent longitudinal strain (b).

3. Discussion

The close agreement seen in Fig. 9 (b) between small strains measured using a conventional extensometer and strains measured using DIC suggest that the accuracy achievable by DIC is quite good. Further, the good correlation between curves produced using Eqs. (2) and (3), and the fact that they are based partly on different assumptions, strengthen the confidence in both approaches. The repeatability seen in Fig. 12 also shows that the method gives consistent results. The maximum difference between the stresses calculated by the two equations was approximately 6%. Even though the difference is small, it may have a significant impact on e.g. strain localization phenomena. It is therefore advisable to use the most accurate method to calculate the current cross sectional area, which is believed to be the method based on lateral displacements.

Quite large differences in stress were observed when calculating the true stress based on the assumption of transverse isotropy and measurements from one face only. This is especially the case for the displacement based calculations (40% difference), but also the strain based (10% difference). Further, Zhang et al. [14] showed that even for isotropic materials the area reduction may not be

proportional to the thickness reduction. It is therefore recommended to measure the transverse contraction on more than one face.

The two aforementioned methods to calculate the true stress have some assumptions in common, namely that the cross section is rectangular and stresses are constant throughout the cross section. It is well known that the latter assumption does not hold in the neck area, where the stress distribution has been the subject of numerous investigations [14–17].

It should be noted that the curves extracted by the methods described in this paper represent the average axial stress in the cross section versus the total longitudinal strain. After the onset of necking, the stress becomes three dimensional and the effective stress and the stress in the axial direction will no longer coincide (but the deviation may be small). Further, Hooke's law does not apply to the current material after some stretching. Since also the elastic strains proved to be quite large for the current material, the plastic strain cannot be approximated by the total strain and is, therefore, unknown unless some tests including unloading are carried out. After necking, the equivalent plastic strain will not be equal to the plastic strain component in the longitudinal direction. It is, therefore, evident that the effective stress versus equivalent plastic strain curves are not readily extracted from the data obtained through the described experiments. A possible solution may be to use inverse modelling to identify the parameters of the constitutive models. In any case, the current measurement techniques give valuable data.

4. Conclusion

A novel experimental methodology has been developed and successfully used to determine the true stress–strain curve for an impact modified polypropylene. It has been shown that the isochoric assumption is invalid for the present material, and that the transverse contraction has to be measured to obtain the true stress. It has further been shown that 3D DIC is a useful tool for doing this.

Two procedures to calculate the true stress–strain relation were tested and found to give almost identical results for the present material. The method where surface strains measured directly by DIC were used to calculate the current cross-sectional area is essentially identical to the procedures reported by Parsons et al. [4,5] De Almeida et al. [6] and Fang et al. [7]. The current investigation, therefore, confirms the applicability of those methods for the present material. However, the difference in remaining thickness between the centre and the side of the specimen may be larger for other materials and specimen geometries. Then, the assumption that surface strains are representative for the strains throughout the cross section may not be valid, and the method based on normal displacements may give more accurate results.

It has also been shown that the transverse contraction should be measured on more than one face, as quite large discrepancies were observed when assuming transverse isotropy and calculating the current cross sectional area based on measurements on only one face.

Acknowledgements

The present work was carried out with financial support from SINTEF Materials and Chemistry. The PhD-scholarship of Hamid Daiyan is funded by an industrial consortium and The Research Council of Norway via the BIA programme.

References

- [1] C. G'Sell, J.M. Hiver, A. Dahoun, Experimental characterization of deformation damage in solid polymers under tension, and its interrelation with necking, *International Journal of Solids and Structures* 39 (13–14) (2002) 3857–3872.
- [2] J. Mohanraj, D.C. Barton, I.M. Ward, A. Dahoun, J.M. Hiver, C. G'Sell, Plastic deformation and damage of polyoxymethylene in the large strain range at elevated temperatures, *Polymer* 47 (16) (2006) 5852–5861.
- [3] J.M. Gloaguen, J.M. Lefebvre, Plastic deformation behaviour of thermoplastic/clay nanocomposites, *Polymer* 42 (13) (2001) 5841–5847.
- [4] E. Parsons, M.C. Boyce, D.M. Parks, An experimental investigation of the large-strain tensile behavior of neat and rubber-toughened polycarbonate, *Polymer* 45 (8) (2004) 2665–2684.
- [5] E.M. Parsons, M.C. Boyce, D.M. Parks, M. Weinberg, Three-dimensional large-strain tensile deformation of neat and calcium carbonate-filled high-density polyethylene, *Polymer* 46 (7) (2005) 2257–2265.
- [6] O. De Almeida, F. Lagattu, J. Brillaud, Analysis by a 3D DIC technique of volumetric deformation gradients: application to polypropylene/EPR/talc composites, *Composites Part A: Applied Science and Manufacturing* 39 (8) (2008) 1210–1217.
- [7] Q.Z. Fang, T.J. Wang, H.G. Beom, H.P. Zhao, Rate-dependent large deformation behavior of PC/ABS, *Polymer* 50 (1) (2009) 296–304.
- [8] <www.limes.com>.
- [9] <www.correlatedsolutions.com>.
- [10] M. Sutton, S. McNeill, J. Helm, Y. Chao, Advances in two-dimensional and three-dimensional computer vision, *Photomechanics* (2000) 323–372.
- [11] V. Tiwari, M.A. Sutton, S.R. McNeill, S. Xu, X. Deng, W.L. Fourney, D. Bretall, Application of 3D image correlation for full-field transient plate deformation measurements during blast loading, *International Journal of Impact Engineering* 36 (6) (2009) 862–874.
- [12] <www.mathworks.com>.
- [13] A.G. Considère, Mémoire sur l'emploi du fer et de l'acier dans les constructions, *Annales des Ponts et Chaussées* 9 (6) (1885) 574–575.
- [14] Z.L. Zhang, M. Hauge, J. Ødegård, C. Thaulow, Determining material true stress–strain curve from tensile specimens with rectangular cross-section, *International Journal of Solids and Structures* 36 (23) (1999) 3497–3516.
- [15] P.W. Bridgman, *Studies in Large Plastic Flow and Fracture*, McGraw-Hill, New York, 1952.
- [16] Z.L. Zhang, J. Ødegård, O.P. Søvik, Determining true stress–strain curve for isotropic and anisotropic materials with rectangular tensile bars: method and verifications, *Computational Materials Science* 20 (1) (2001) 77–85.
- [17] Z.L. Zhang, J. Ødegård, O.P. Søvik, C. Thaulow, A study on determining true stress–strain curve for anisotropic materials with rectangular tensile bars, *International Journal of Solids and Structures* 38 (26–27) (2001) 4489–4505.

Paper 4

H. Daiyan, E. Andreassen, F. Grytten, H. Osnes, R. H. Gaarder

Shear testing of polypropylene materials analysed by digital image correlation and numerical simulations

Shear testing of polypropylene materials analysed by digital image correlation and numerical simulations

H. Daiyan¹, E. Andreassen^{1,*}, F. Grytten¹, H. Osnes², R. H. Gaarder¹

¹ SINTEF, Box 124 Blindern, NO-0314 Oslo, Norway

² Dept. of Mathematics, University of Oslo, Box 1053 Blindern, NO-0316 Oslo, Norway

Abstract

Three different polypropylene-based materials (two talc-filled compounds and one unfilled homopolymer) were tested with two different in-plane shear test methods (Iosipescu and V-notched rail). The three materials behaved differently in the shear tests. Most notably, cracks developed in tension near the notches for the particle-filled materials, while the unfilled homopolymer did not fracture. There were also differences between the materials regarding strain localisation between the notches, strain rates vs. strain level (for a given cross-head speed), thickness change in the sheared section, and triaxiality. The yield stresses in shear, uniaxial tension and uniaxial compression showed pressure sensitivity, as represented by e.g. the Drucker-Prager criterion. At least for equivalent strain rates below 1 s^{-1} , the strain rate sensitivity of the yield stress was approximately the same in these three stress states. The stress-strain curves obtained with the two methods were quite similar. There were some differences between the methods regarding ease of mounting and aligning specimens, complexity of specimen deformation patterns, and uniformity of the strain distribution between the notches. Digital image correlation (DIC) was used to assess shear strain distributions and triaxiality. Numerical simulations qualitatively predicted some of the experimental observations.

1. Introduction

This study was motivated by the need for reliable data for shear stress vs. strain in order to calibrate material models for numerical simulations with finite element codes. In order to simulate the loading of geometrically complex injection moulded components of ductile polymers, involving multiaxial stress states, the material model should be based on true stress-strain data obtained in uniform stress states up to large strains. Shear data of polymers are often considered to be unreliable for modelling purposes, since different test fixtures tend to give different results. The strain distribution may be quite non-uniform, and many polymers do not or cannot exhibit a shear fracture [1-3].

There are several fixtures available for shear testing, some defined in test standards and some developed and used only by certain research groups. Some of the tests have the advantage that

the test specimens have simple geometries with constant thickness, so that they can be easily machined from injection moulded plates with thickness within the typical range for injection moulding. This is the case for the two in-plane shear tests used in the present paper; the Iosipescu test and the V-notched rail test. The first version of the Iosipescu test was introduced in the 1960s and used for metals. Different versions of this test have been used in many studies of thermoset composites and wood. The Modified Wyoming Iosipescu (MWI) shear test used in the present paper was standardised for composites in 1993 [4-6]. The other shear test used in this paper, the V-Notched Rail (VNR) shear test, was standardised for composites in 2005 [7-8]. Compared to the MWI test, the VNR test has a larger gauge section (better suited for some composites) and the specimen is clamped along the sides, which is better for transferring high loads than the edge loading in the MWI test.

* Corresponding author. E-mail: erik.andreassen@sintef.no

The literature on shear testing of thermoplastic polymers is scarce, but there are some studies with variants of the Iosipescu fixture [1, 9-12] and other fixtures [11, 13-24]. Results relevant for this paper are referred to in the Discussion section. Experimental issues and specialities have also been treated or commented in some of these papers on thermoplastic polymers: G'Sell et al. [13] discussed how to minimise buckling and normal stresses. Pierron et al. [10] used finite element simulations to obtain a correction for non-uniform shear stress when determining the shear modulus. Dean and Crocker [22] used a purpose-built extensometer, and also corrected for non-uniform shear stress and for contributions from bending to the displacements. Delhaye et al. [24] performed shear testing at strain rates up to 300 s^{-1} , adapting the test specimen into a compression direct-impact Hopkinson bar. Digital image correlation has been used to record the shear strain distributions in some recent studies [12, 24]. Finally, it can be mentioned that some test fixtures can be used for testing in shear in combination with tension or compression [25-27].

The deformation mechanisms at the microscale are complex in semi-crystalline polymers, and there is a distinct difference between the structure development vs. equivalent strain in uniaxial tension and shear. The structure development in polypropylene submitted to shear deformation has been studied in-situ and ex-situ by various microscopy and diffraction techniques. The main mechanism starting at the yield point involves crystal (lamella) slip.

This paper compares two different shear test fixtures and three different polypropylene materials in terms of shear strain distributions, strain states (deviation from shear), strain rate variations (for constant cross-head speed) and crack initiation. Numerical simulations are also performed.

Earlier studies with similar materials by our group have dealt with tensile testing using digital image correlation [28], low-speed impact testing of plates [29-30], and calibration and verification of material models for numerical simulations [31].

2. Experimental

2.1 Materials and standard mechanical properties

Three different polypropylene (PP) materials were tested: An α -nucleated homopolymer (referred to as PPH), a 20% mineral-filled elastomer-modified PP (PP20) and a 40% mineral-filled PP (PP40). PP20 and PP40 are injection moulding grades for automotive exteriors and underhood applications, respectively. PPH is available as extruded plates (PP DWU AlphaPlus from Simona). Selected properties from the material data sheets are given in Table 1.

Table 1. Selected properties for the materials in this study (mechanical properties at 23 °C).

	PP40	PP20	PP H
Melt flow rate (ISO 1133) (230 °C, 2.16 kg) [dg/min]	2	13	-
Density (ISO 1183) [kg/m ³]	1222	1050	915
Tensile modulus (ISO 527) (2 mm/min) [GPa]	3.8	1.4	1.7
Tensile stress at yield (ISO 527-2) (50 mm/min) [MPa]	31	16	33
Ratio of yield stress to modulus (both in tension)	8.2	11.4	19.4
Charpy impact strength, notched (ISO 179/1eA) [kJ/m ²]	5	58	9

2.2 Preparation of test specimens

The two shear test methods used in this paper are based on the V-Notched Rail standard (ASTM D 7078 [7]) and the V-Notched Beam standard (ASTM D 5379 [4]), both addressing composite materials. (The latter is usually referred to as the Iosipescu test, but note that there are different Iosipescu fixtures in use.) Test specimens were machined according to these standards, either from 3.9 mm thick injection moulded plates (for the materials PP20 and PP40) or 4.0 mm thick extruded plates (PPH), see specimens mounted in the respective fixtures in Figure 1. If nothing else is stated, the notch root radius was 1.3 mm. To assess the effect of the notch root radius, some

specimens with notch root radius 0.65 mm and 2.6 mm were also prepared. Depending on the notch

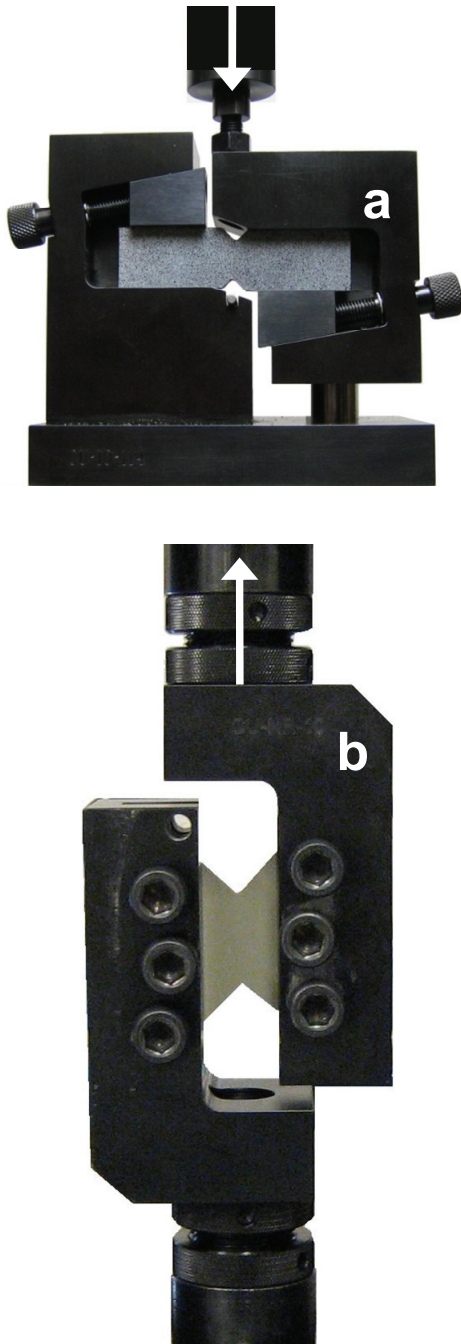


Figure 1. a) Test specimens mounted in the modified Wyoming Iosipescu (MWI) fixture. b) V-Notched Rail (VNR) fixture. The length between the notches was 13 mm for the MWI specimen and 32 mm for VNR specimen. The loading of the fixtures is indicated by arrows.

root radius, 1.3 mm or 2.0 mm diameter double-tooth milling tools were used.

The injection-moulded plates were rectangular ($80 \times 80 \text{ mm}^2$), and moulded using a fan-gated cavity (in order to obtain a roughly straight flow front). The injection moulding conditions were based on the standard ISO 1873-2:2007. The mould temperature was $40 \text{ }^\circ\text{C}$, the melt temperature was $200 \text{ }^\circ\text{C}$, the flow front speed was 0.2 m/s, and the maximum holding pressure was 40 MPa. The test specimens were machined with the ligament (the section between the notches) parallel to the flow direction in the plate. Initially a few specimens with the ligament perpendicular to the flow direction were also tested. The shear yield stress (based on nominal shear stress, see definition below) was only 2-3 % higher for these specimens.

2.3 Mechanical testing

The shear test fixtures in Figure 1 (from Wyoming Test Fixtures) were mounted in a universal test machine fitted with a 5 kN load cell. The force was logged (with a DAQCard 6062E from National Instruments) in synchronisation with the image acquisition of a digital image correlation (DIC) system (Vic3D from Limes/Correlated Solutions). The 3D DIC system measured the 3D displacement field of the specimen surface during loading, based on images from two cameras (2452×2052 pixels, 75 mm f/2.8 lenses) with overlapping views of the specimen front side from two angles. In order to utilise the DIC technique, a matt random black and white speckle pattern was sprayed on the front side of the specimen prior to testing, as seen in Figure 1a.

In the modified Wyoming Iosipescu (MWI) shear fixture (according to ASTM D 5379, Figure 1a) the force is transferred to the specimen by edge loading. The right part of the fixture is pressed down, sliding on a bearing post. The V-notched rail (VNR) test fixture (according to ASTM D 7078, Figure 1b) consists of two separate halves connected to each side of the test specimen. In each half of the fixture, the specimen is fastened between two blocks, which are clamped by three bolts. The specimen is aligned (the line between the notches aligned in loading direction) in the mounting step by using two spacer blocks.

Twisting, buckling and other unwanted effects may occur in such tests, see e.g. [32]. Initial testing of 2.4 mm thick PP20 specimens in the VNR fixture showed the onset of a (reproducible) buckling pattern at shear strains above ca 0.1. In order to avoid this, 4 mm thick specimens were chosen for all tests. Still, it was difficult to avoid some twisting (a few tens of a millimetre) of the (low-modulus) PP20 specimens in the VNR fixture. This was probably partly due to slightly uneven tightening of the bolts, and partly due to some twisting when mounting the fixture in the testing machine, although the specimen was supported by the stop blocks until the loading started. The bolts were tightened with a torque just high enough to avoid slip between specimen and fixture. The scatter between repeated tests was reduced as experience was gained with the VNR mounting procedure. However, with PP20 the scatter was still somewhat higher with the VNR fixture than with the MWI fixture.

With the MWI fixture there was some in-plane bending of the specimen between the supports. We will return to this in Sect. 3.7. Furthermore, there was local out-of-plane displacement (thickening) due to the compression/indentation near the end of the edge support facing the notch, see also Sect. 3.2.

The cross-head speed was 2 mm/min with the VNR fixture and 1 mm/min with the MWI fixture if nothing else is stated. As discussed in Sect. 3.3, different cross-head speeds were used with the two fixtures in order to have roughly similar strain rates at the centre of the specimen (i.e. at the midpoint between the notches) at the yield point.

2.4 Stress and strain calculated from experiments

The experimental shear stress-strain curves in this paper are based on the total (elastic and plastic) shear strain at the centre of the specimen (i.e. at the midpoint between the notches) and the nominal shear stress. The yield stress in this paper is defined as the (first) maximum of the stress vs. strain curve, as is customary for polymers (ISO 527-1).

The shear strain was measured by DIC, and the strain at the centre was taken as an average over a circle with radius equal to 1-2% of the distance between the notches. With the shear strain distributions in this study, the error is small when using average for the strain at the centre. (The ISO standards for these shear tests on composites, specify strain gauges for measuring the strain at the centre. Some calculate a correction factor to obtain the local strain at the centre from the strain gauge data [10]).

The nominal shear stress referred to in this paper is the axial force recorded by the load cell divided by the initial cross-section (distance between notches multiplied by specimen thickness). Correction factors relating the nominal stress to the shear stress at the centre are discussed in Sect. 3.7.

The strains in this paper (except Table 1) are logarithmic strains (Hencky strains) calculated from the DIC measurements of the specimen surface. The logarithmic strain tensor is given by

$$\boldsymbol{\varepsilon} = \frac{1}{2} \log(\mathbf{F}^T \mathbf{F}), \text{ with } \mathbf{F} = \mathbf{I} + \nabla \mathbf{u} \quad (1)$$

where \mathbf{F} is the deformation gradient tensor, $\nabla \mathbf{u}$ is the displacement gradient tensor and \mathbf{I} is the identity tensor.

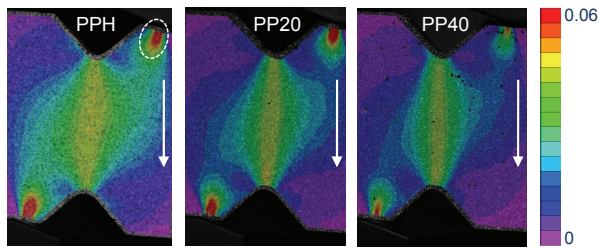
3. Results

Results from DIC measurements are given in Sect. 3.1 to 3.4. The following topics are addressed for the three materials and the two fixtures: Shear strain distributions, strain states (deviation from shear), strain rate variations and crack initiation. Shear stress-strain curves are reported in Sect. 3.6. Finally, some results from numerical simulations are presented in Sect. 3.7.

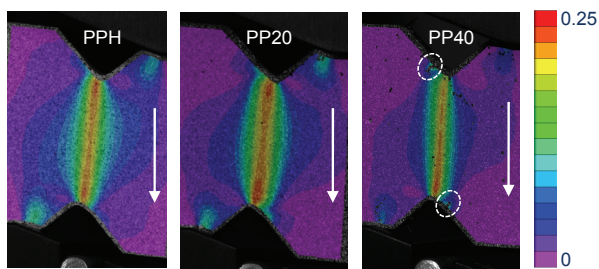
3.1 Shear strain distributions

The shear strain distributions obtained with the MWI fixture are shown in Figure 2. At small strains (Figure 2a), the strain is less localised along the line between the notches for PPH than for the other two materials. This is probably due to the high ratio of yield stress to modulus for PPH. At large strains (Figure 2b) PP20 shows somewhat less

strain localisation, which may be due to its low modulus. At this strain level, the PP40 specimen fractured on the side of the notch in tension, at some distance from the notch root (the fracture is encircled in Figure 2b).



(a) Strain at centre ~ 0.045



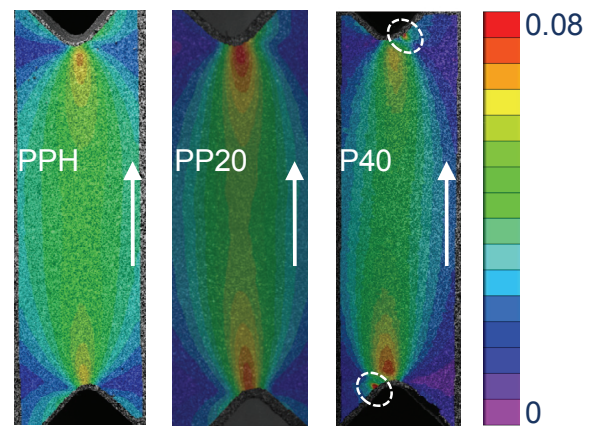
(b) Strain at centre ~ 0.2

Figure 2 Shear strain distributions for the three materials in the MWI fixture, as measured by DIC. Moving side indicated by arrow. Low strain level in upper row (a) and high strain level in lower row (b). The dashed circle in the upper row shows the maximum associated with the deformation of the specimen near the angled section of the support. The dashed circles in the lower row show the positions of cracks.

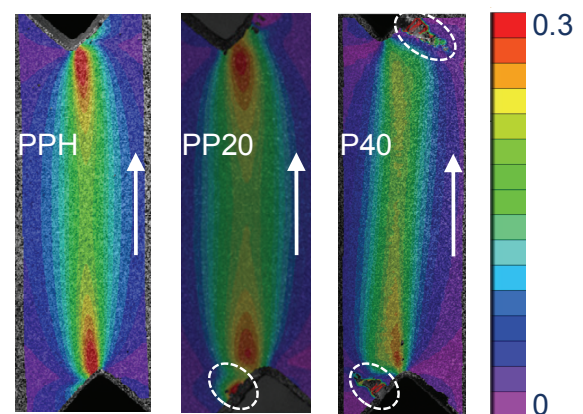
In order to reach larger strains before the MWI fixture collides with the specimen (the unsupported area near the notch), a modified specimen with deeper notch (4.7 mm) and larger opening angle (115°) was used. With this modified specimen the shear strain distribution was somewhat broader horizontally. Furthermore, the edge effect near the notch will be more pronounced: The vertical distance from the notch root to the position where the shear strain is almost constant was slightly larger, and the contribution of this edge effect to the strain inhomogeneity will be higher. Different notch angles were also evaluated in an earlier study, which concluded that 90° gave the best compromise between strain homogeneity and shear strain range [12]. An

alternative way to reach larger strains without collision between fixture and specimen is of course to modify the fixture [1].

Shear strain distributions obtained with the VNR fixture are shown in Figure 3. Compared to the distributions with the MWI fixture, the variation along the vertical line from the centre to the notch root is higher, see Figure 4. This variation increases with increasing strain level. (This was also the case for the MWI fixture, but the variation was low in all cases.) Due to the higher strain localisation near the notch root, fracture occurs at a lower centre strain (fractures are encircled in Figure 3).



(a) Strain at centre ~ 0.045



(b) Strain at centre ~ 0.2

Figure 3. Shear strain distributions for the three materials in the VNR fixture, as measured by DIC. Moving side indicated by arrow. Low strain level in upper row (a) and high strain level in lower row (b). The circles show the positions of fractures.

Also note in Figure 2 and Figure 3 that the upper and lower notch move relative to each other

horizontally, i.e. they are not vertically aligned at large strains. For the MWI fixture the shear zone between the notches is rotated clock-wise (Figure 2b), but this effect is not so clear for the VNR fixture.

The effect of the notch root radius on the shear strain distribution was assessed for the VNR fixture. Specimens of PP20 were machined with three different notch root radii, 0.65 mm, 1.3 mm and 2.6 mm. All specimens had the same length between the notches (32 mm). The variation in shear strain along a vertical line from the centre to the notch root increased with decreasing notch root radius, and this effect increased with increasing strain level, see Figure 4.

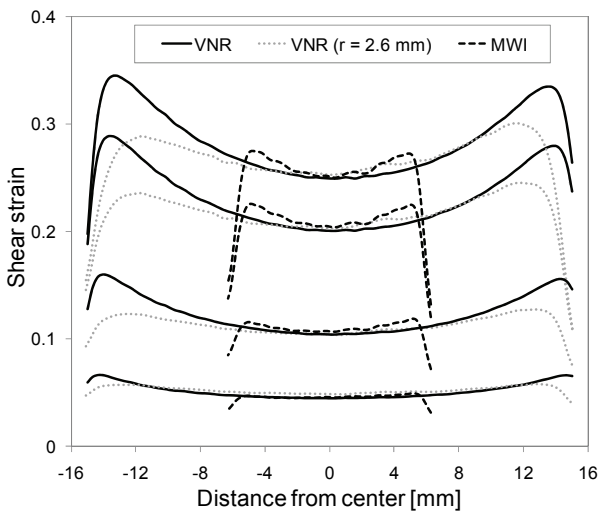


Figure 4. Shear strain distributions along the line between the notches, as measured by DIC. Data for PP20 in the two fixtures (VNR and MWI). Data for a VNR specimen with larger notch radius ($r = 2.6$ mm) are also included.

3.2 Strain states

With some assumptions, simple shear can be considered as a combination of pure shear and a rigid-body rotation. Our DIC data show that the principal strain axes rotate as a function of strain for both fixtures. In Figure 5, DIC data are compared to an analytical expression for simple shear. For PPH in the MWI fixture, the angle of the first principal strain vs. shear strain follows the analytical expression for strain up to almost 0.2. For all materials the slope of the angle vs. shear strain is steeper for the VNR fixture than for the

MWI fixture. Furthermore, the steepness increases in the sequence PPH-PP20-PP40.

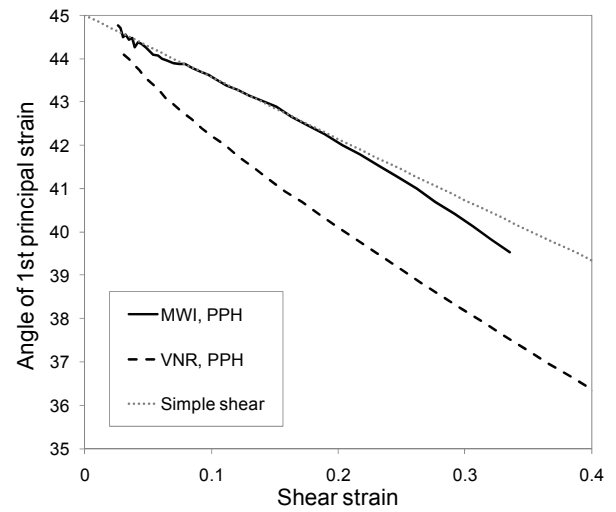


Figure 5. Direction of the first principal strain vs. shear strain, both taken at the centre of the test specimen. Data from DIC (solid and dashed lines) and from an analytical expression for simple shear [16] (dotted lines). The DIC data are shifted vertically (the slopes are reproducible, but there is some scatter in the starting point).

The two in-plane principal strains (from DIC) do not have equal absolute values as for pure or simple shear. This deviation from shear can be assessed by a strain-based triaxiality ratio as shown and defined in Figure 6. This ratio shows that, at the centre of the specimen, there is, in addition to shear, a transition from a compressive state (sum of principal in-plane strains is negative) to a tensile state, at a certain shear strain. This agrees with the vertical displacements measured by DIC, which initially show compression, then elongation of the section between the notches. When the centre shear strain is above ~ 0.05 , this triaxiality ratio is positive for all materials, and the VNR fixture shows a higher triaxiality than the MWI fixture. The triaxiality for centre shear strains above ~ 0.05 seems to increase in the sequence PPH-PP20-PP40.

Distributions of the triaxiality ratio over MWI specimen surfaces are shown in Figure 7. As expected, the triaxiality is positive and negative on the sides of the notch in tension and compression, respectively. The triaxiality factor is close to $1/3$ (corresponding to uniaxial tension for the standard

3D triaxiality ratio) near the cracks for PP40 (lower right image in Figure 7).

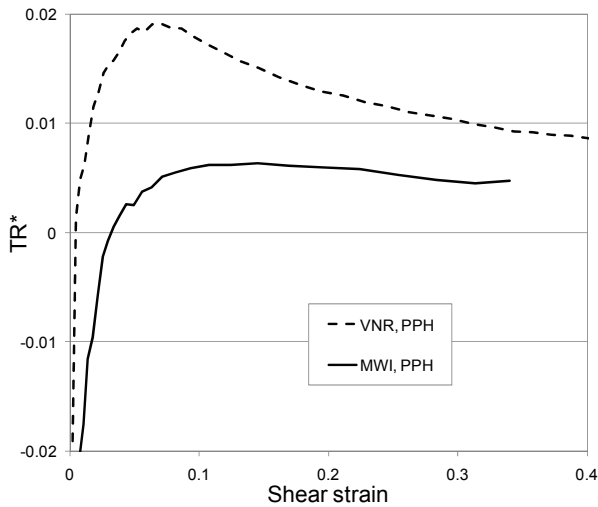


Figure 6. A triaxiality ratio (TR^*) calculated from in-plane principal strains vs. shear strain, from DIC measurements at the centre of PPH specimens. TR^* is the ratio of mean strain to von Mises equivalent strain, assuming plane strain, and normalised so that $+1/3$, 0 and $-1/3$ correspond to uniaxial tension, shear and uniaxial compression, respectively. If plane stress is assumed, the qualitative trend would be the same, but with somewhat higher absolute values for the triaxiality.

Figure 7 also shows that PPH has a lower maximum triaxiality than PP40. The actual values for the maximum triaxiality ratio are 0.14, 0.22 and 0.28 for PPH, PP20 and PP40, respectively, at a centre strain of 0.2. Only PP40 shows a significantly higher maximum triaxiality at a centre shear strain of 0.2 compared to 0.045. The compression/indentation of the specimen near the MWI fixture supports gives rise to a strain state with triaxiality ratios as low as -0.6 . These compressive regions start at the upper right and lower left of the images in Figure 7. Note that in these regions the DIC measurements show a significant positive out-of-plane displacement, and a thickening is clearly seen on the unloaded specimen. Hence, the value of the triaxiality ratio based on in-plane strains (as defined in Figure 6) should only be used as an indication of the strain state in this highly compressed region.

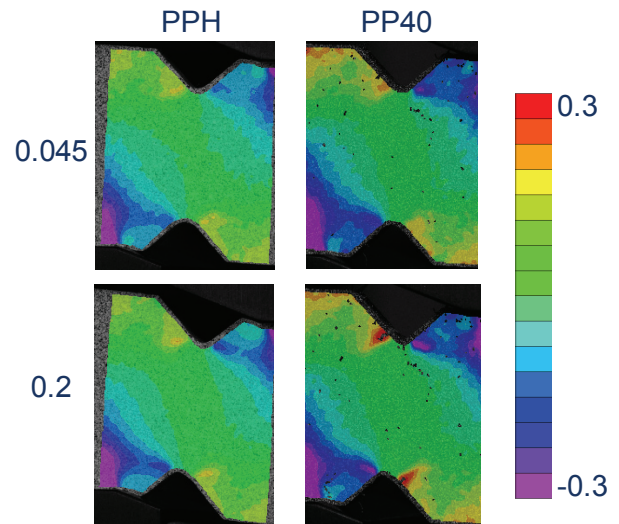


Figure 7. The triaxiality ratio (TR^*), as defined in Figure 6, for MWI specimens. Data for two materials (columns) and two centres shear strains (rows). The specimens and centre shear strains are the same as in Figure 2.

Similar triaxiality distributions for the VNR fixture are shown in Figure 8. Also for this fixture the maximum triaxiality is higher for PP40 than for PPH. The actual values for the maximum triaxiality ratio are 0.15, 0.26 and 0.32 for PPH, PP20 and PP40, respectively, at a centre strain of 0.2. These values are somewhat higher than for the MWI fixture at the same centre shear strain. With the VNR fixture, cracks had developed for both PP40 and PP20 at a centre shear strain of 0.2.

3.3 Shear strain rates

The shear tests were performed with a constant cross-head speed. The shear strain rate at the centre varies as exemplified in Figure 9. The centre shear strain rate increases from one level to another at the onset of yielding (the change in slope for the curves in Figure 9 at a shear strain around 0.05). At low centre shear strains, the centre shear strain rates are the same with the two fixtures when using the same cross-head speed (data sets for 2 mm/min in Figure 9). However, since the strain localisation at the centre is stronger for the MWI fixture, the centre shear strain rate will be higher with the MWI fixture, for shear strains above a certain value (around 0.04 in

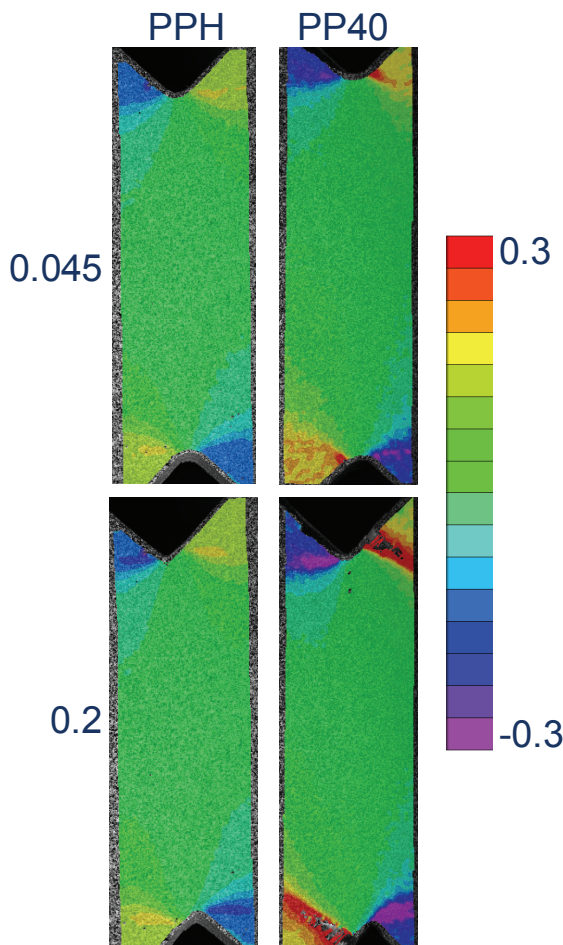


Figure 8. The triaxiality ratio (TR^*), as defined in Figure 6, for VNR specimens. Data for two materials (columns) and two centres shear strains (rows). The specimens and the centre shear strains are the same as in Figure 3.

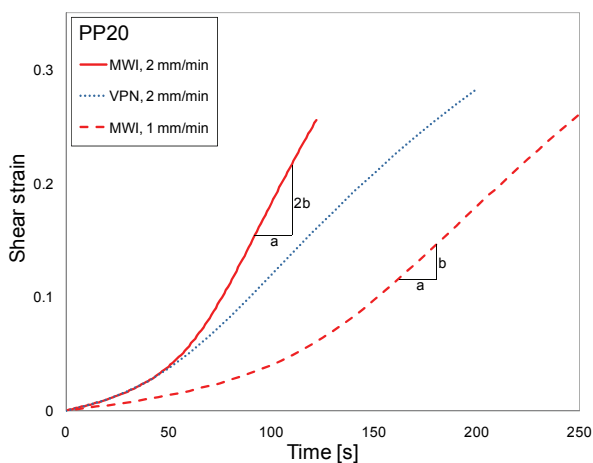


Figure 9. Shear strain at the centre of the specimen (from DIC measurements) vs. time. Data for PP20 with the two fixtures, and two cross-head speeds.

Figure 9). In order to have similar shear strain rates for strains above the yield point, different cross-head speeds were used with the two fixtures in this study (2 mm/min with the VNR fixture and 1 mm/min with the MWI fixture), if nothing else is stated.

Shear strain rate vs. shear strain for the three materials in the MWI fixture is plotted in Figure 10. In this plot the three materials display different curves reflecting their individual mechanical responses. The same relative trends are seen in a similar plot for the VNR fixture (not shown). Note the marked knee in the curve for PPH at small strains. This feature was also observed in the plot for the VNR fixture.

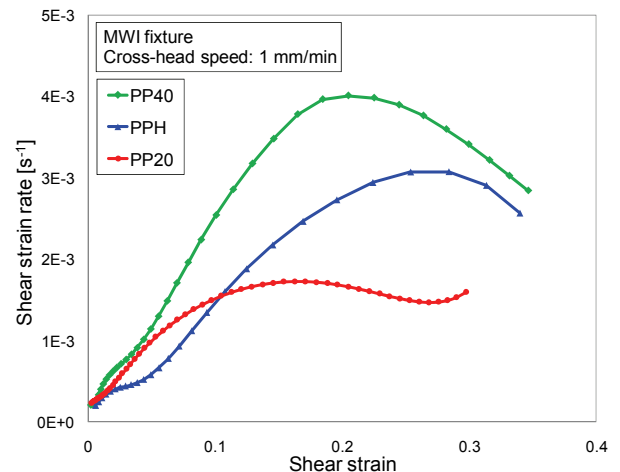


Figure 10. Shear strain rate vs. shear strain. Based on DIC measurements at the centre of MWI specimens.

3.4 Crack initiation

As mentioned above and shown in several figures for PP40 and PP20, a stable crack initiate at the side of the notch in tension, where the first principal strain is almost parallel to the specimen edge along the side of the notch. Hence, these materials/specimens display a mode I (opening) fracture.

The value of the first principal strain at the crack initiation can be assessed from the DIC results. It is difficult to calculate strains for pixels near the edge (meeting the thickness side). However, with optimised camera angles and speckle patterns, strains quite near the edge can be obtained, as shown in Figure 11. For PP20 the first

principal strain “at break” was about 0.25-0.30, and the value was about the same for both fixtures. For PP40 the first principal strain at break was below 0.06. For PPH no fracture was observed even at large strains (centre shear strain about 1).

Fracture surfaces of PP20 and PP40 are shown in Figure 12. The finer structure of the PP20 fracture surface is probably due to the rubber toughening mechanism.

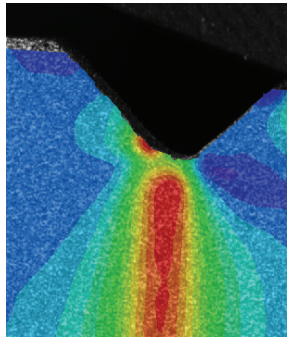


Figure 11. Distribution of first principal strain for an MWI specimen of PP20. An example of an image with data calculated from DIC near the edge of the specimen. The side in the thickness direction is seen as a shadow behind the left side of the notch.

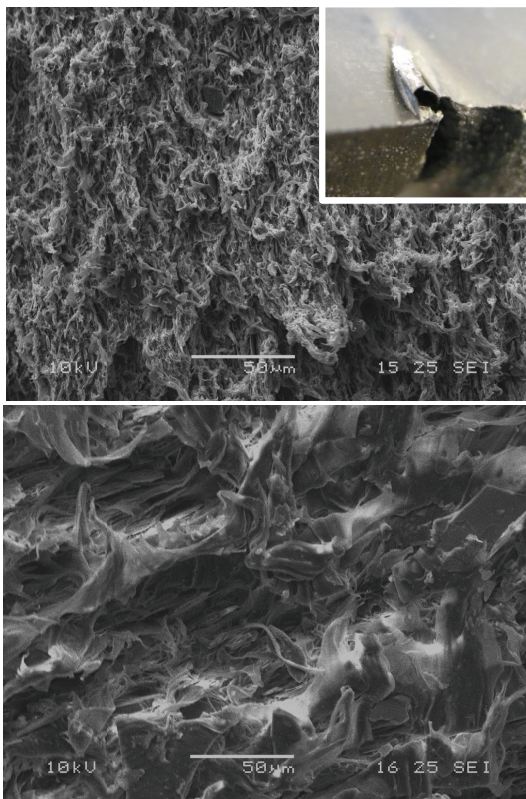


Figure 12. SEM micrographs of the fracture surfaces of VNR specimens of PP20 (upper) and PP40 (lower). The insert in the upper right corner shows that the skin layer of the specimen did not fracture.

3.5 Changes in the dimensions of the sheared section

PPH showed necking (a local decrease in specimen thickness) in the sheared section. This is shown in Figure 13 for a specimen subjected to a large shear strain. PP20 showed slight necking, while the specimen thickness increased for PP40. For PPH and PP40 the change in thickness when loaded to a strain at the centre of 0.2 was about -2% and 2%, respectively. A strong whitening effect along the sheared section was observed for PP40. Whitening was not observed for PP20 (at least not for the limited strains that could be reached before crack initiation), but the surface became dull (with a fine line pattern) in the sheared section. PP20 specimens were also cut perpendicular to the shearing line, but whitening was not seen. Nor did PPH show whitening, even at very large strains.

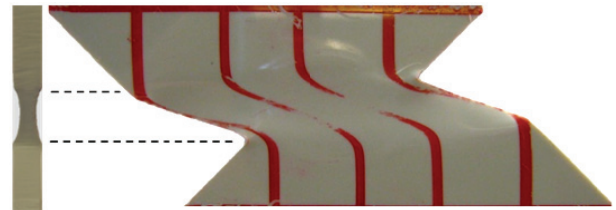


Figure 13. Necking of a PPH VNR specimen. The cross-section of test specimen is shown to the left.

The elongation of the sheared section was measured by DIC. Initially this section was shortened due to compression, and then it was elongated. However, the effects were small. For PP20/MWI the elongation of this section was less than 0.2% for a shear strain of about 0.2 at the centre.

In Sect. 3.6, the sheared cross-section is assumed to be constant, i.e. the nominal stress is calculated using the initial cross-section dimensions. Stress corrections are addressed in Sect. 3.7.

3.6 Shear stress as function of shear strain

This section is based on the nominal shear stress (recorded axial force divided by initial cross-section) and the shear strain at the centre of the specimen (measured by DIC).

Although the DIC technique as employed in this study has limited resolution at very small strains, shear moduli were calculated from the initial part of the shear stress-strain curves. The calculation was based on the MWI standard [4], typically for shear strains between 0.001 and 0.006. Table 2 shows the experimental shear moduli (G) and the shear moduli calculated from tensile data (G_T), assuming a linear-elastic isotropic material with a Poisson's ratio of 0.4 (measured for PP20). The agreement is good for PP20 and PPH.

Table 2. Measured material properties. Shear data obtained with the MWI fixture.

	PP40	PP20	PPH
Shear modulus (G) [GPa]	1.22	0.49	0.59
$G_T = E/2(1+\nu)$, with $\nu=0.4$ [GPa]	1.36	0.50	0.61
Yield stress in shear (σ_{YS}) [MPa]	22.3	10.8	23.1
Ratio of yield stresses in tension and shear (σ_{YT}/σ_{YS})	1.39	1.48	1.43

NB: Tensile yield stress (σ_{YT}) from data sheets with higher strain rate; ca 0.01 s^{-1} .

The shear yield stresses measured with the MWI fixture are given in Table 2. The ratio of yield stresses in tension and shear is also tabulated. The ratios do not obey the von Mises criterion, for which the ratio is equal to the square root of 3 (1.73). When considering the higher strain rate in the tensile tests (data reported in data sheets), the deviation is even larger. PP20 was also tested in uniaxial tension and compression in the authors' lab, using DIC and test specimens injection moulded with similar processing conditions as for the shear test specimens. When considering data at similar strain rates, the ratio of yield stresses in tension and shear (based on "first maximum" values) is 1.50, and the ratio of yield stresses in compression and shear is 2.09.

Shear stress-strain curves for the three materials and the two fixtures are shown in Figure 14. Curves obtained with the two fixtures are

similar at low strains, and the yield stresses are quite similar. Two characteristic differences are addressed below:

The post-yield reduction in nominal stress for PP40 (both fixtures) and PP20 (VNR fixture) in Figure 14 coincides with crack initiation at the tensile side of the notch. Due to the larger difference between the strain at the centre and near the notch for the VNR fixture, the crack initiates at a lower centre strain for this fixture. The weak apparent softening for PPH may, at least partly, be due to the necking.

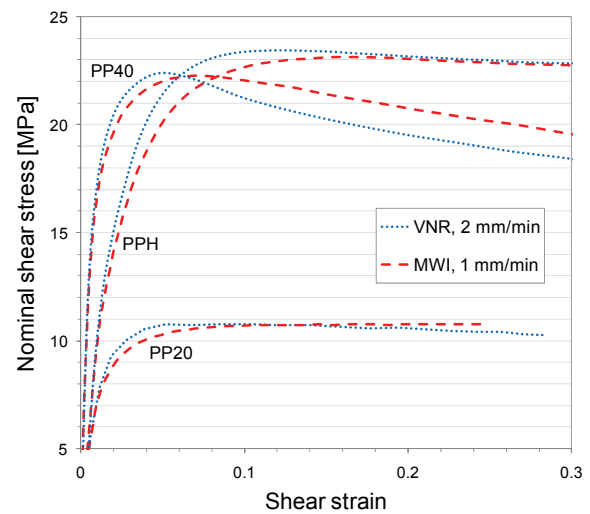


Figure 14. Stress-strain curves for the three materials (PP20, PP40 and PPH) with the two fixtures (VNR and MWI). Note that the stress axis starts at 5 MPa.

Figure 14 also clearly shows that the two fixtures give rise to different stress-strain curves near the yield point: A sharper knee is obtained with the VNR fixture. This is partly due to the different cross-head speeds used, and partly due to the geometries giving somewhat different stress distributions, see Sect. 3.7. The effect of cross-head speed is shown in Figure 15 (see also corresponding strain rates in Figure 9). Even when using the same cross-head speeds with the two fixtures the knee is sharper with the VNR fixture.

The effect of strain rate on the yield stress seems to be the same as in uniaxial compression and tension, at the low strain rates used in the shear tests, see Figure 16.

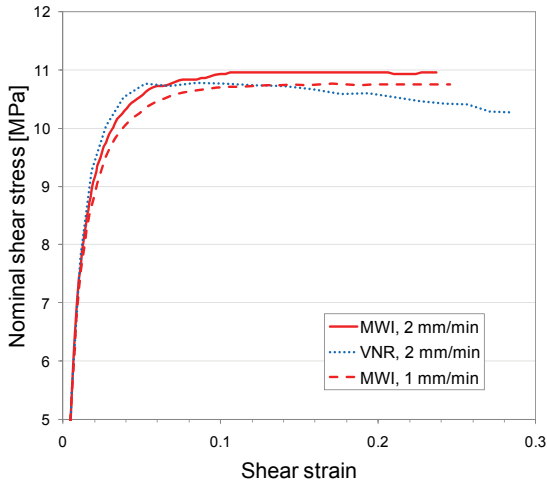


Figure 15. Stress-strain curves for PP20 with different fixtures (MWI and VNR) and cross-head speeds (1 and 2 mm/min). Note that the stress axis starts at 5 MPa.

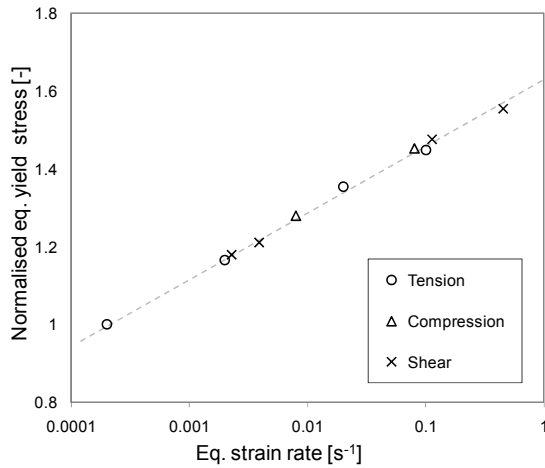


Figure 16. Strain rate sensitivity of PP20 tested in uniaxial tension, uniaxial compression and shear (MWI). Yield stresses are taken as “first maximum” values. Values for a given stress state are multiplied by a factor for normalisation to an arbitrary common level for all three stress states.

3.7 Numerical simulations

In order to gain more insight, the shear tests were simulated with the finite element code LS-DYNA. The test specimens were modelled with solid elements with one integration point, and there were four elements through the thickness of the specimens. Boundary conditions were implemented as follows (see also Figure 1): For the VNR specimen the clamped part of the specimen was omitted; the outer nodes on the stationary side were fixed, while those on the moving side were given a vertical displacement. A friction coefficient of 0.2 was used for the contact between the MWI specimen and the fixture. A

Drucker-Prager based elastic-plastic material model (with higher yield stress in compression than in tension) was used, calibrated with data for PP20 [28, 31].

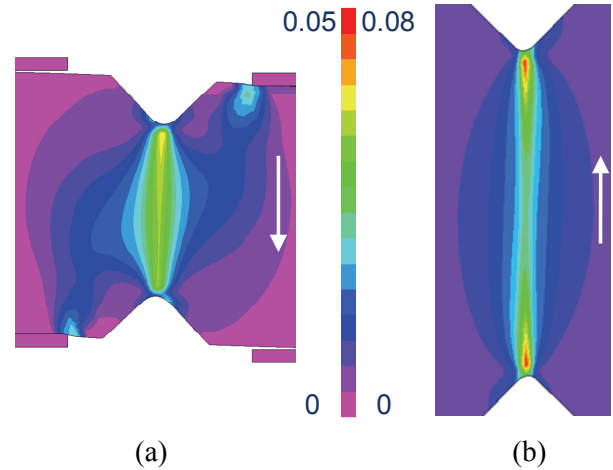


Figure 17. Simulated shear strain distributions for the MWI specimen (a) and the VNR specimen (b) (the full geometries are not shown). The strain is about 0.045 at the centre of the specimens, and the scales are about the same as in Figure 2 and Figure 3, respectively.

Simulated shear strain distributions (Figure 17) are qualitatively in agreement with those from DIC measurements (Figure 2 and Figure 3), although the strain localisation is overpredicted. Note the in-plane bending of the MWI specimen, and the higher shear strain near the upper notch than near the lower notch. The asymmetry in Figure 17a is somewhat lower with a pressure-independent material model (same yield stress in compression and tension). Careful examination of the (experimental) DIC data also shows a tendency for a higher shear strain near the upper notch at small strains, but the simulations overpredict this effect. Simulated distributions at different strain levels are shown in Figure 18. For the VNR specimen the distribution is quite flat at small strains, and the relative height of the maxima near the notches increases with increasing strain level. At large strains (> 0.2), the distribution transforms into an asymmetric convex shape. This was not observed experimentally, and it is probably partly due to the relative horizontal displacement of the notches, and partly due to numerical artefacts. For the MWI specimen the distribution is concave at small strains (this was

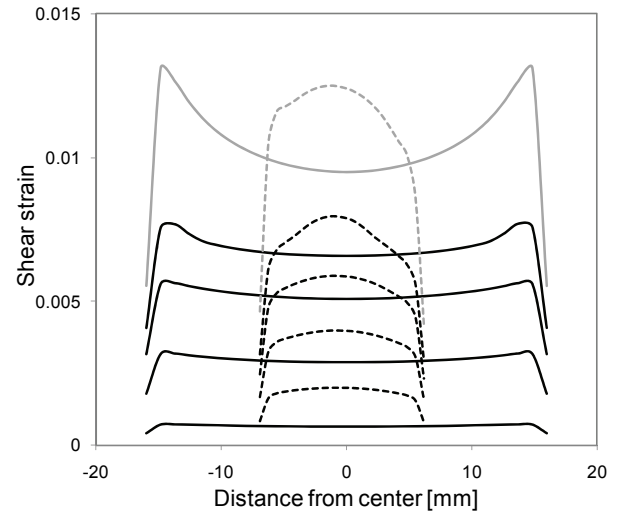
not observed experimentally). The asymmetry increases with increasing strain level, and at a certain strain level the distribution transforms to a convex shape. Hence, the simulated strain distributions for the MWI fixture in particular do not agree well with the experimental observations, and further work is needed to capture the rather complex behaviour in this fixture.

What about the shear stress distributions? When approaching the yield point, the shear stress does not localise between the notches as the shear strain does. The shear stress distributions between the notches (Figure 19) are more uniform than the shear strain distributions (Figure 18). Experimentally, we have used the nominal shear stress (recorded axial force divided by the area of the cross-section between the notches). A correction factor can be calculated from the simulations, as shown in Figure 20. The correction factor for the MWI fixture at a few percent strain is similar to the value in ref. [10]. However, our model needs to be refined for quantitative use. The simulated stress-strain curves are shown in Figure 21. The difference between the curves from the two fixtures (near the yield point) is qualitatively the same as observed experimentally (Figure 14).

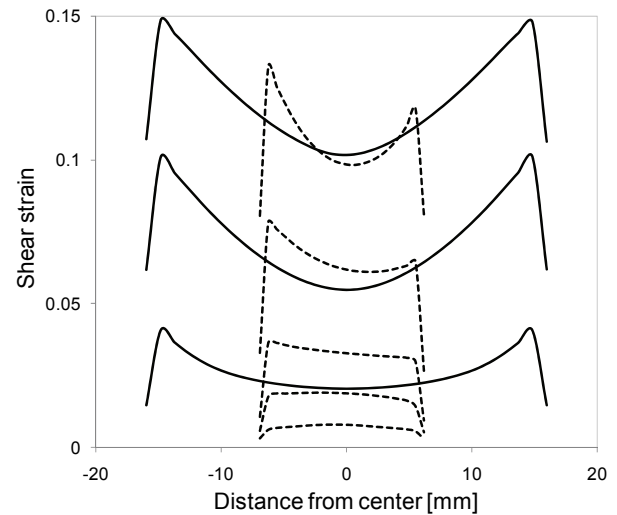
It can also be noted that this difference is the same in simulations with a material model without pressure dependent yield stress.

Finally, we will consider the stress triaxiality, i.e. the ratio of mean stress to von Mises equivalent stress. (This triaxiality measure equals $1/3$ and $-1/3$ for uniaxial tension and compression, respectively). For metals, some new in-plane shear test specimens have also been proposed recently [33-35], and some of these has been claimed to give low stress triaxiality. Simulated triaxiality distributions for the VNR and MWI specimens, and two specimens proposed in recent papers, are shown in Figure 22. The maximum values for the triaxiality near the edge by the notch are practically the same for these four specimens. The triaxiality values at the centre are lowest for the MWI and VNR fixtures. Triaxiality vs. shear strain at the centre is shown in

Figure 23. Note that the triaxiality with the Gao specimen [35] is lower when using the material model (for steel) in their paper.



(a)



(b)

Figure 18. Simulated shear strain distributions between the notches for the MWI specimen (dashed lines) and the VNR specimen (solid lines). Data for small (a) and medium (b) strains. The grey curves correspond to the same load steps as the grey curves in Figure 19.

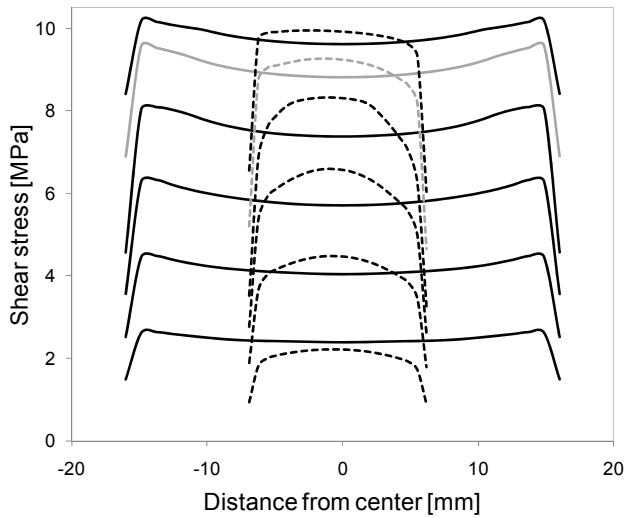


Figure 19. Simulated shear stress distributions between the notches for the MWI specimen (dashed lines) and the VNR specimen (solid lines). The grey curves correspond to the same load steps as the grey curves in Figure 18a.

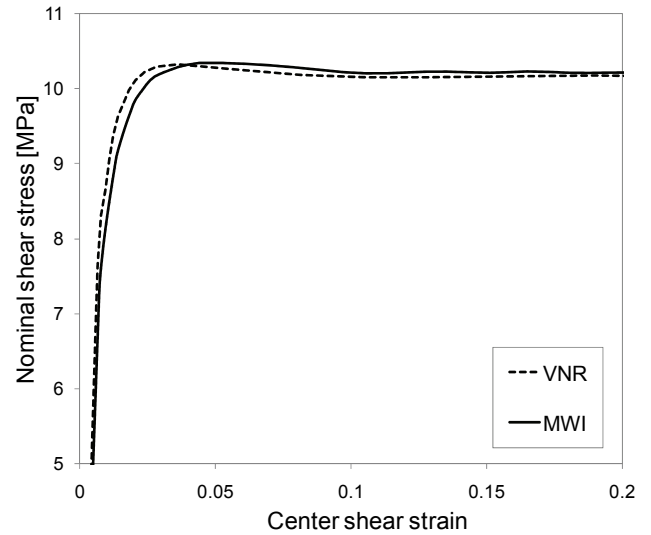


Figure 21. Simulated nominal shear stress vs. shear strain at the centre (between the notches). Note that the stress axis starts at 5 MPa.

4. Discussion

4.1 Strain state

A low triaxiality was measured at the centre of the specimen (midpoint between the notches) by DIC, and above a certain strain level this triaxiality was tensile. Deviation from pure shear at the centre of MWI specimens has been reported experimentally and in simulations for composite materials at small strains [6, 25, 36-37]. The stress state was compressive in these studies. With an aluminium specimen the deviation from pure shear was small [6]. With a special simple shear specimen and fixture [13], a compressive stress was measured perpendicular to the loading direction, when the specimen was constrained perpendicular to the loading direction, and also described the development of normal stresses for simple shear with finite strains. The qualitative trends for the triaxiality with the MWI and VNR fixtures were similar experimentally and in the simulations. Furthermore, the simulations indicate that these fixtures give low triaxialities compared with other fixtures, and that the triaxiality with a given fixture depends on the material.

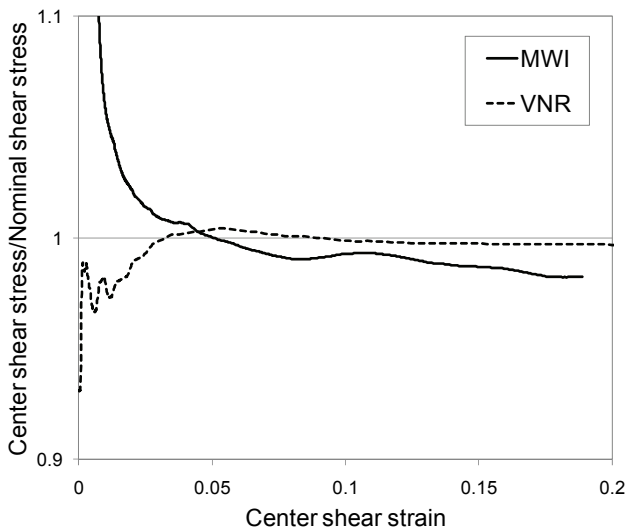


Figure 20. Simulated ratio of centre shear stress to nominal shear stress vs. centre shear strain for the two fixtures.

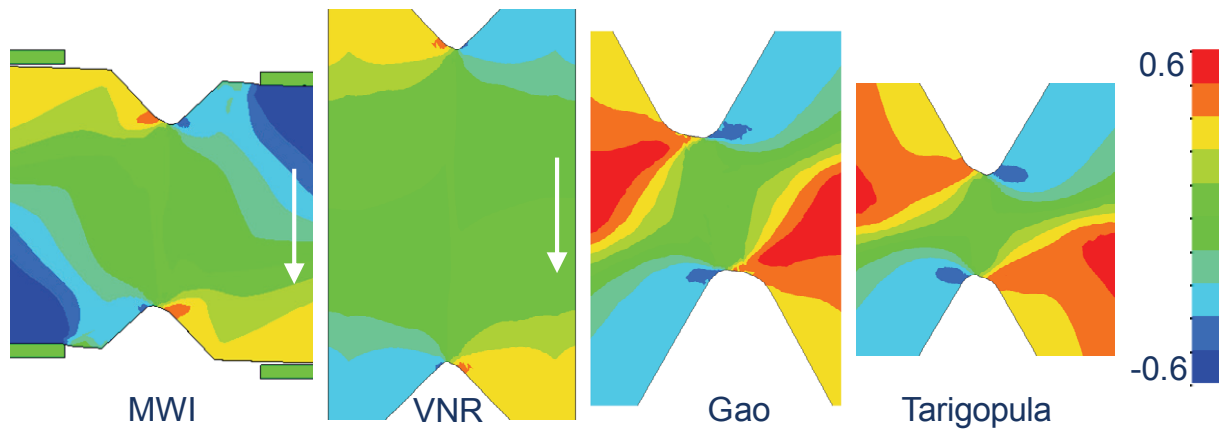


Figure 22. Simulated stress triaxiality distributions for the two fixtures/specimens used in this study, and for specimens introduced by Tarigopula et al. [34] and Gao et al. [35] (only the areas near the notches are shown). The distributions shown above correspond to a shear strain of ca 0.2 at the centre for all specimens. (NB: These four specimens are not shown at the same scale; the distances between the notches are 13, 32, 5 and 2.5 mm, respectively.) The maximum values for the triaxiality near the edge by the notch are practically the same for the four specimens (0.38-0.42). The triaxiality values at the centre vary somewhat, in two groups (MWI: 0.009, VNR: 0.012, Gao: 0.057, Tarigopula: 0.061).

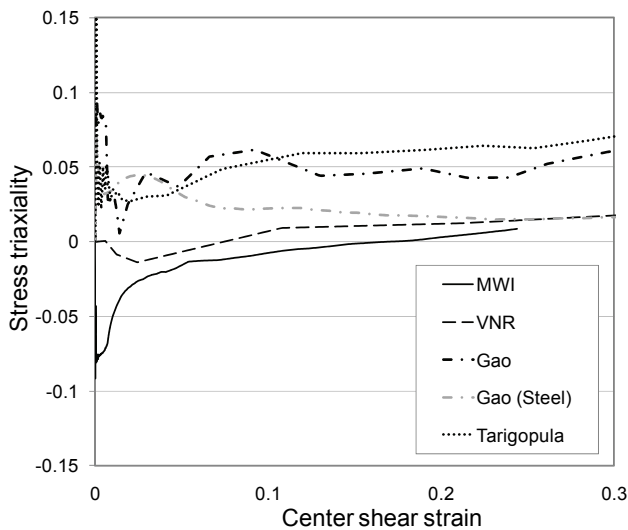


Figure 23. Simulated stress triaxiality at the centre vs. shear strain at the center.

4.2 True stress-strain

As mentioned in the experimental section, the nominal shear stress (force divided by cross-section) is most commonly used when reporting the shear stress from these test methods, while the shear strain is taken as the local value at the centre of the specimen. Hence, a uniform distribution of shear stress over the cross-section is assumed. Furthermore, force contributions from other stress states and positions (outside the sheared cross section) are included in the nominal stress.

Other issues are the variation in dimensions of the sheared cross-section, the variation in strain rate, temperature effects, and the possible variation in stress through the thickness of the specimen. An increase in the thickness of the sheared section, as observed for PP40, has been reported before for a mineral-filled PP [12]. Based on the measured variation in local strain rate for a constant cross-head speed (as in our study), a profiled cross-head speed could be programmed to achieve a quasi-constant strain rate or plastic strain rate, but there would still be variation over the specimen. Finally, it could be commented that the shear strain rates used in this study are probably low enough to avoid adiabatic heating [13].

These issues can, in principle, be corrected for by inverse modelling, aiming at predicting the strain distribution and the force vs. time, and maybe also thickness variation of the specimens during testing. However, this requires a model well calibrated in tension and compression. The non-uniform shear stress distribution can be corrected for by using the experimental shear strain distribution, as described for shear modulus determination [32].

4.3 Yield stresses in shear, tension and compression

As reported in the Sect. 3.6, the yield stresses in shear, tension and compression do not obey the

von Mises criterion, i.e. the ratio of the stress at yield in uniaxial tension to the stress at yield in shear (σ_{YT}/σ_{YS}) is not $\sqrt{3}$. Our values for this ratio are lower, as in other studies of PP and PP-based materials [1-2, 12, 23] and polymers in general. On the other hand, the ratio of yield stresses in uniaxial compression and shear is higher than $\sqrt{3}$. The main effects of stress state on the yield stress are related to pressure-dependence (molecular mobility reduced by pressure, and disentanglement of polymer chains depending on the stress state) and cavitation. Some comments to these effects are given below.

The pressure-dependence increases as the compressive component increases, when going from uniaxial tension to shear to uniaxial compression. Hence, for yield criteria with pressure-dependence, such as the Mises-Raghava criterion [38-39] or the linear Drucker-Prager criterion [23], the factor σ_{YT}/σ_{YS} is lower than $\sqrt{3}$, and the factor σ_{YC}/σ_{YS} is larger than $\sqrt{3}$. As an example, the Mises-Raghava criterion is often calibrated in tension and compression, and from this σ_{YT}/σ_{YS} is given by $\sqrt{3}/(\sigma_{YC}/\sigma_{YT})$. The yield surface of PP20, based on the yield stresses in shear, tension and compression, is well described by the Mises-Raghava and the linear Drucker-Prager criteria. Note that the stress state was not pure shear in our tests; i.e. the triaxiality ratio was not zero. Hence, the experiment will give a yield stress slightly different from that of pure shear. Depending on the criterion for determining the yield stress, the triaxiality may be negative (small strains) or positive. If the deformation at the micro level is shear is another question, see Sect. 4.4.

Cavitation may occur in stress states with tensile components, and it promotes local shear yielding between cavities [23]. Hence, the yield stress in uniaxial tension decreases with increasing cavity volume fraction (volume strain) as the plastic strain increases. On the other hand, the yield stress in shear remains essentially constant, as shown with the cavitation-modified criterion of Dean and Crocker calibrated with a PP material [23]. A further consequence of this is that the ratio

σ_{YT}/σ_{YS} may depend on the strain rate, because the strain rate affects the kinetics and degree of cavitation. Furthermore, cavitation is favoured by higher triaxiality, e.g. reducing the yield stress in biaxial tension relative to that in uniaxial tension.

The whitening observed for PP40 (only) in the shear tests is probably due to voiding related to debonding at the interface of mineral particles. This voiding will also reduce the yield stress as described above. For PP based materials in general, subjected to stress states with tensile components, cavitation occurs in soft domains (rubber particles and amorphous material).

In shear tests of PP materials with a MWI fixture, Xiang and Sue [1] observed that the deviation from the von Mises criterion regarding the ratio σ_{YT}/σ_{YS} varied with specimen thickness. The ratio σ_{YT}/σ_{YS} was clearly lower than $\sqrt{3}$ for 3.2 mm thick specimens. The ratio was higher for 2.0 mm thick specimens, and close to $\sqrt{3}$ for two of the materials. The lower ratio for the thick specimens could be due to higher triaxiality (transition towards plane strain). The larger deviation from pure shear, in combination with an associated higher degree of cavitation and a lower pressure effect, could explain the thickness effect.

4.4 Crack initiation

A stable mode I (opening) crack near the notch root appeared for the PP20 and PP40 specimens. This limits the maximum shear strain for which shear stress-strain data can be obtained. Furthermore, these tests cannot be used to measure the shear strengths of these materials.

Xiang and Sue [1] observed a macroscopic shear (mode II) fracture for a PP homopolymer tested in a MWI fixture, when the specimen had sharp pre-cracks in the notch roots. Microscopically, the fracture in the shear zone started as inclined microcracks, which became connected by further shearing. When adding ethylene-propylene rubber to this PP, the shear fracture was suppressed in favour of stretching in the shear zone.

Liu and Piggott [11] tested PP and seven other thermoplastic polymers with a Iosipescu fixture and with a punch test. With the Iosipescu

fixture, a PC and a PMMA showed mode I fracture, while the other thermoplastic polymers only showed tensile stretching of the section between the notches. Furthermore, based on punch shear tests, Liu and Piggott [2-3] claimed that most polymers fail in tension when tested in shear, but PE with short chains and PP were exceptions (no fracture in punch test).

For PP20 the cracks initiated at a local first principal strain around 0.25-0.30. This is much lower than the strain at break for uniaxial tensile testing of standard test bars (type 1A of the ISO 527-2 standard); for which the value 0.7 is given in the datasheet and a value near 1 was measured in our lab [28] (all Hencky strains). The lower (first principal) strain at break for the shear specimens seems to be partly due to the machined surface, and partly due to specimen processing: Small test bars for tensile testing were machined from the injection moulded plates used to make the shear specimens, and from the injection moulded standard (large) test bars. The small test bars machined from plates had a strain at break of 0.35, while the small test bars machined from standard test bars had a strain at break of 0.6. Hence, roughly speaking, the reduction from ca 1 to 0.6 is due to machining, while the reduction from 0.6 to 0.35 is due to different processing-induced properties. The plate and the standard tensile test bar had the same thickness (4 mm) and the same nominal injection moulding conditions. However, the test bar is more than twice the length of the plate. Therefore, a larger fraction of the cross-section of the test bars could have an advantageous flow-induced microstructure.

Hence, for a material such as PP20, shear stress-strain data up to larger strains could be obtained (without fracture initiation) with specimens having as-moulded notches, and a flow path typically 3 times longer than the specimen, as illustrated in Figure 24. For some materials the MWI specimen should be shifted further away from the gate than indicated in this figure, in order to have more homogeneous flow, giving a MWI specimen with better planarity and homogeneity. Flow-induced anisotropy may be higher with this specimen than those cut from plates in the present study, see Sect. 2.2.

5. Concluding remarks

These three PP-based materials behaved differently in the shear tests. Most notably, mode I cracks developed near the notches for the particle-filled PP20 and PP40, while the unfilled homopolymer PPH did not fracture for shear strains up to about 1. The occurrence of mode I cracks limits the strain range for testing these materials, and we have suggested a method for preparing test specimens which may increase this strain limit. There were also differences between the materials regarding strain localisation between the notches, strain rates (for a given cross-head speed), thickness change in the sheared section, and triaxiality. These differences reflect the individual mechanical responses of the materials, and the ratio of yield stress to elastic modulus can be used to explain some of the differences.

Both test methods in this study use flat v-notched specimens that are easily machined from plates. Furthermore, the stress-strain curves obtained with the two methods are quite similar. It is easier (and faster) to mount specimens of soft

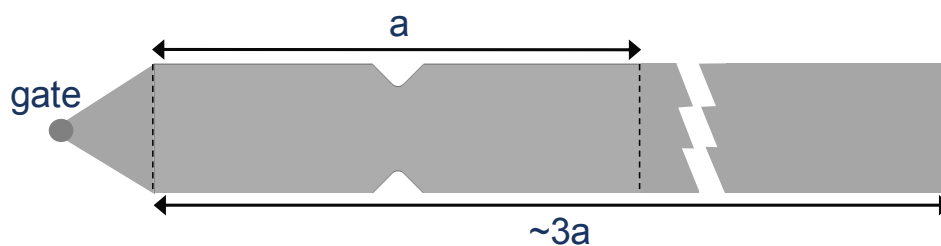


Figure 24. Schematic injection-moulded part containing a MWI specimen (machined out at dashed lines).

materials (such as PP20) in the MWI fixture without introducing misalignment or bending. The VNR fixture is better suited for stiffer materials, and it allows for larger strains. The VNR specimen also has a simpler deformation pattern, making it easier to perform inverse modelling. On the other hand, the MWI fixture showed a more uniform strain distribution between the notches, and somewhat lower triaxiality.

Digital image correlation (DIC) is an important tool, providing the experimentalist with strain distributions, and measures of triaxiality based on in-plane strains. DIC in combination with numerical simulations allows for inverse modelling. Simulations reported in this paper qualitatively predict some of the experimental observations, such as distributions of shear strain and triaxiality, and differences between stress-strain curves obtained with the two test methods. The simulations indicate that the MWI and VNR specimens are just as good as some shear specimens introduced recently [34-35] regarding the triaxiality at the centre and near the notches.

The yield stresses in shear, uniaxial tension and uniaxial compression did not obey the von Mises criterion. These yield stresses constitute a yield surface which can be represented by criteria with pressure sensitivity, such as Mises-Raghava or Drucker-Prager. In the interval of equivalent strain rates examined in this study, the strain rate sensitivity of the yield stress was approximately the same in shear, uniaxial compression and uniaxial tension.

Acknowledgement

This study was funded by the Research Council of Norway (BIA programme) and Plastal AS. The SEM analysis was performed by H. Amedro (SINTEF).

References

[1] C. Xiang, H.J. Sue, Iosipescu shear deformation and fracture in model thermoplastic polyolefins, *J. Appl. Polym. Sci.*, 82 (2001) 3201-3214.

[2] K. Liu, M.R. Piggott, Fracture failure processes in polymers. I: Mechanical tests and results, *Polym. Eng. Sci.*, 38 (1998) 60-68.

[3] K. Liu, M.R. Piggott, Fracture failure processes in polymers. II: Fractographic evidence, *Polym. Eng. Sci.*, 38 (1998) 69-78.

[4] ASTM D5379, Standard Test Method for Shear Properties of Composite Materials by the V-Notched Beam Method, 1993

[5] D.F. Adams, The Iosipescu shear test method as used for testing polymers and composite materials, *Polym. Compos.*, 11 (1990) 286-290.

[6] D.F. Adams, E.Q. Lewis, Experimental strain analysis of the Iosipescu shear test specimen, *Exp. Mech.*, 35 (1995) 352-360.

[7] ASTM D7078 Standard Test Method for Shear Properties of Composite Materials by V-Notched Rail Shear Method, 2005

[8] D.O. Adams, J.M. Moriarty, A.M. Gallegos, D.F. Adams, The V-notched rail shear test, *J. Compos. Mater.*, 41 (2007) 281-297.

[9] M. Weinberg, Shear testing of neat thermoplastic resins and their unidirectional graphite composites, *Composites*, 18 (1987) 386-392.

[10] F. Pierron, A. Vautrin, B. Harris, The Iosipescu in-plane shear test: Validation on an isotropic material, *Exp. Mech.*, 35 (1995) 130-136.

[11] K. Liu, M.R. Piggott, Shear strength of polymers and fibre composites: 1. Thermoplastic and thermoset polymers, *Composites*, 26 (1995) 829-840.

[12] N. Temimi-Maaref, A. Burr, N. Billon, Damaging processes in polypropylene compound: Experiment and modeling, *Polym. Sci. Ser. A*, 50 (2008) 558-567.

[13] C. G'Sell, S. Boni, S. Shrivastava, Application of the plane simple shear test for determination of the plastic behaviour of solid polymers at large strains, *J. Mater. Sci.*, 18 (1983) 903-918.

[14] C. G'Sell, A.J. Gopez, Plastic banding in glassy polycarbonate under plane simple shear, *J. Mater. Sci.*, 20 (1985) 3462-3478.

[15] G. Hedner, R. Seldén, P. Lagercrantz, Shear test for thermoplastic polymers, *Polym. Eng. Sci.*, 34 (1994) 513-518.

[16] C. G'Sell, A. Dahoun, Evolution of microstructure in semi-crystalline polymers under large plastic deformation, *Mater. Sci. Eng., A*, 175 (1994) 183-199.

[17] M.C. Boyce, E.M. Arruda, R. Jayachandran, The large strain strain compression, tension, and

simple shear of polycarbonate, *Polym. Eng. Sci.*, 34 (1994) 716-725.

[18] R. Quinson, J. Perez, M. Rink, A. Pavan, Yield criteria for amorphous glassy polymers, *J. Mater. Sci.*, 32 (1997) 1371-1379.

[19] C. G'Sell, V. Favier, J.M. Hiver, A. Dahoun, M.J. Philippe, G.R. Canova, Microstructure transformation and stress-strain behavior of isotactic polypropylene under large plastic deformation, *Polym. Eng. Sci.*, 37 (1997) 1702-1711.

[20] G. Castelein, G. Coulon, C. G'Sell, Polymers under mechanical stress: Deformation of the nanostructure of isotactic polypropylene revealed by scanning force microscopy, *Polym. Eng. Sci.*, 37 (1997) 1694-1701.

[21] G. Coulon, G. Castelein, C. G'Sell, Scanning force microscopic investigation of plasticity and damage mechanisms in polypropylene spherulites under simple shear, *Polymer*, 40 (1999) 95-110.

[22] G. Dean, L. Crocker, Prediction of the impact performance of plastics using finite element methods, Measurement Good Practice Guide No 87, National Physical Laboratory, UK, 2006

[23] G. Dean, L. Crocker, Prediction of impact performance of plastics mouldings. Part 1: Material models and determination of properties, *Plast. Rubber Compos.*, 36 (2007) 1-13.

[24] V. Delhaye, A.H. Clausen, F. Moussy, O.S. Hopperstad, R. Othman, Mechanical response and microstructure investigation of a mineral and rubber modified polypropylene, *Polym. Test.*, 29 (2010) 793-802.

[25] G. Odegard, K. Searles, M. Kumosa, Critical examination of the Iosipescu shear test as applied to 0 degrees unidirectional composite materials, *Mech. Comp. Mater. Struct.*, 6 (1999) 229-256.

[26] F. De Magistris, L. Salmen, Combined shear and compression analysis using the Iosipescu device: analytical and experimental studies of medium density fiberboard, *Wood Sci. Technol.*, 37 (2004) 509-521.

[27] R. El-Hajjar, R. Haj-Ali, In-plane shear testing of thick-section pultruded FRP composites using a modified Arcan fixture, *Compos. Part B: Eng.*, 35 (2004) 421-428.

[28] F. Grytten, H. Daiyan, M. Polanco-Loria, S. Dumoulin, Use of digital image correlation to measure large-strain tensile properties of ductile thermoplastics, *Polym. Test.*, 28 (2009) 653-660.

[29] H. Daiyan, E. Andreassen, F. Grytten, O.V. Lyngstad, T. Luksepp, H. Osnes, Low-velocity impact response of injection-moulded polypropylene plates - Part 1: Effects of plate thickness, impact velocity and temperature, *Polym. Test.*, 29 (2010) 648-657.

[30] H. Daiyan, E. Andreassen, F. Grytten, O.V. Lyngstad, T. Luksepp, H. Osnes, Low-velocity impact response of injection-moulded polypropylene plates - Part 2: Effects of moulding conditions, striker geometry, clamping, surface texture, weld line and paint, *Polym. Test.*, 29 (2010) 894-901.

[31] H. Daiyan, F. Grytten, E. Andreassen, O.V. Lyngstad, H. Osnes, R.H. Gaarder, E.L. Hinrichsen, Numerical simulation of low-velocity impact loading of polymeric materials, in: 7th European LS-DYNA Conference, DYNAmore, Salzburg, Austria, 2009.

[32] F. Pierron, Saint-Venant effects in the Iosipescu specimen, *J. Compos. Mater.*, 32 (1998) 1986-2015.

[33] Y. Bao, T. Wierzbicki, On fracture locus in the equivalent strain and stress triaxiality space, *Int. J. Mech. Sci.*, 46 (2004) 81-98.

[34] V. Tarigopula, O. Hopperstad, M. Langseth, A. Clausen, F. Hild, O.G. Lademo, M. Eriksson, A Study of Large Plastic Deformations in Dual Phase Steel Using Digital Image Correlation and FE Analysis, *Exp. Mech.*, 48 (2008) 181-196.

[35] F. Gao, L. Gui, Z. Fan, Experimental and Numerical Analysis of an In-Plane Shear Specimen Designed for Ductile Fracture Studies, *Exp. Mech.*, In press, DOI 10.1007/s11340-010-9385-8 (2010).

[36] G. Odegard, M. Kumosa, Determination of shear strength of unidirectional composite materials with the Iosipescu and 10 degrees off-axis shear tests, *Compos. Sci. Technol.*, 60 (2000) 2917-2943.

[37] M. Kumosa, Y. Han, Non-linear finite-element analysis of Iosipescu specimens, *Compos. Sci. Technol.*, 59 (1999) 561-573.

[38] R. Raghava, R.M. Caddell, G.S.Y. Yeh, The macroscopic yield behaviour of polymers, *J. Mater. Sci.*, 8 (1973) 225-232.

[39] R.S. Raghava, R.M. Caddell, A macroscopic yield criterion for crystalline polymers, *Int. J. Mech. Sci.*, 15 (1973) 967-974.

Paper 5

H. Daiyan, E. Andreassen, F. Grytten, H. Osnes, O.V. Lyngstad

Numerical simulation of low-velocity impact loading of a ductile thermoplastic material

Numerical simulation of low-velocity impact loading of a ductile thermoplastic material

H. Daiyan¹, F. Grytten¹, E. Andreassen¹, H. Osnes², O. V. Lyngstad^{3,4}

¹ SINTEF Materials and Chemistry, Box 124 Blindern, NO-0314 Oslo, Norway

² Dept. of Mathematics, University of Oslo, Box 1053 Blindern, NO-0316 Oslo, Norway

³Plastal AS, Box 94, NO-2831 Raufoss, Norway

⁴Present affiliation: SINTEF Raufoss Manufacturing, Box 163, NO-283 Raufoss, Norway

Abstract

Mechanical impact loading of injection-moulded components was simulated. The material was a talc-filled and elastomer-modified polypropylene used in automotive exterior parts. The material model was the linear-elastic–viscoplastic SAMP-1 model, which features pressure-dependent yield stress, plastic dilatation and a simple damage model. The model was calibrated with data from tests in uniaxial tension, shear and uniaxial compression, utilising 3D digital image correlation for full-field displacement measurements. With the calibrated model, two load cases were simulated; centrally loaded clamped plates and three-point bending of bars. The predictions of force vs. deflection were good to fair. The results are discussed in terms of the deficiencies of the calibration data, the heterogeneity and anisotropy of the injection-moulded components, and shortcomings of the model. In particular, the hardening curves at high strain rates are uncertain, and tests in biaxial tension would be useful.

1. Introduction

Numerical simulation of impact loading of polymer materials is of great industrial interest, as these materials are increasingly being used in critical applications and structures. The response to impact loads is of particular interest for automotive applications related to passenger and pedestrian safety. The constitutive models the industry typically uses for these materials today have shortcomings when it comes to predicting multiaxial loading, unloading response (rebound), and fracture.

Ductile polymeric materials show a complex behaviour in impact loading involving large strains [1-2]. The complexity applies to the micromechanical mechanisms as well as the macroscopic response. Therefore, more complex constitutive models are needed.

These require data which may be difficult to determine experimentally.

Several models for polymer materials have been developed and tested the last 30 years. To various degrees these models have described the key features of these materials, such as viscoelasticity, viscoplasticity, pressure-dependent yield stress, plastic dilatation (i.e. plastic Poisson's ratio < 0.5) and damage [3-9].

The present study is based on the phenomenological linear-elastic–viscoplastic model SAMP-1 [10] which is available in the finite-element code LS-DYNA. It features pressure-dependent yield stress, plastic dilatation and a simple damage model. Fracture is not considered in the present study.

2. Experimental

2.1 Material and sample preparation

A commercial 20% mineral and elastomer modified polypropylene compound (ISO code PP+EPDM-TD20) was used in this study. This material is developed for injection-moulded automotive exterior parts.

Dogbones (ISO 527-2, type 1A) and 2 and 4 mm thick plates were injection moulded with processing parameters based on ISO 294-1 and ISO 1873-2.

The anisotropy and inhomogeneity of injection moulded parts can be a challenge when trying to predict their mechanical response [11]. Quasi-static three-point bending tests were performed on bars machined from injection-moulded dogbones and from plates ($4 \times 80 \times 80 \text{ mm}^3$). Bars were cut in directions parallel and perpendicular to the flow direction in the plates. All the bars had the same nominal dimensions ($4 \times 10 \times 80 \text{ mm}^3$, where 4 mm is the original thickness of the injection moulded parts). As shown in Figure 1, the plate is anisotropic in the plane, As often reported [12-13], the stiffness is higher in the flow direction. Bars cut from the dogbone and from the flow direction in the plate have almost the same stiffness, but different post-yield responses. This difference could be due to material anisotropy, but also heterogeneous mechanical properties [14].

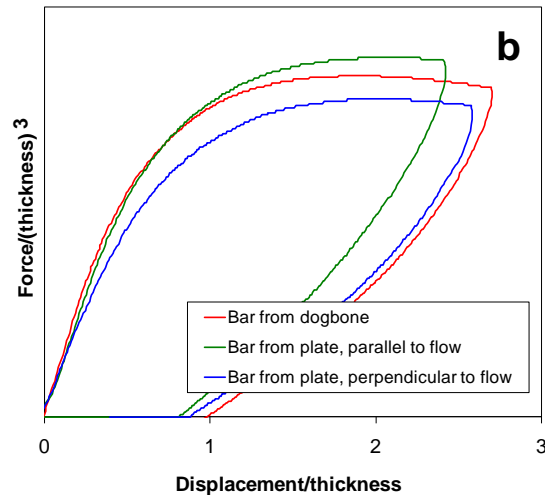
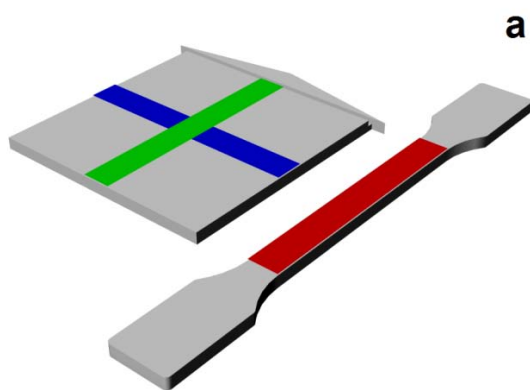


Figure 1 a) Injection-moulded plate and dogbone and illustration of bars machined from these parts. b) Experimental results for three-point bending of the bars illustrated above. The thickness of the bars was around 4 mm and the loading rate was 10 mm/min.

2.2 Calibration tests

Injection-moulded specimens were tested in uniaxial tension, shear and uniaxial compression in order to calibrate the constitutive model. All tests were performed at 23 °C. 3D digital image correlation (DIC) was used for full-field displacement measurements.

2.2.1 Uniaxial tension

Tensile testing was carried out as described in ref. [15], in order to obtain true stress (Cauchy stress) as function of true strain (logarithmic strain), both as average values over the cross-section, see Figure 2a. The effect of necking on the stress state (triaxiality) was not considered.

The actual cross-section was measured using 3D DIC during the test, revealing large plastic volumetric strains, i.e. the constant volume assumption (von Mises yielding) was not valid. Poisson's ratio versus total strain is shown in Figure 3. It was calculated from transverse and longitudinal strains measured with DIC.

DIC was not used at high strain rates (above 0.1 s^{-1}). The hardening curves of the

model at these rates were based on the curve obtained with DIC at low strain rates, and scaled according to the measured yield stresses shown in Figure 2b.

The yield stress can be defined in different ways. The values shown in Figure 2b are the “first maximum” values (first point on the stress-strain curve with a zero gradient). These were used for the scaling, since they were the only reliable yield stress values at high strain rates. However, for the material model, the yield stress was determined from loading-unloading tests described in the paragraph below; the yield stress was defined as the stress when the plastic strain exceeded zero. This yield stress definition was compared to other definitions, and it corresponded to a 0.2% strain offset criterion. Furthermore, the elastic modulus in the model (1.40 GPa) was taken as the effective slope between origo and this yield stress-strain. This modulus was lower than the modulus determined according to ISO 527 (1.79 GPa).

2.2.2 Tensile loading-unloading

In order to characterise the unloading response and the damage development [16], loading-unloading tests were performed in uniaxial tension. All tests were done at 10 mm/min (nominal strain rate 0.002 s^{-1}) and the cross-head speed was kept constant during loading and unloading (the effect of strain rate was low up to the highest rate tested, ca 0.2 s^{-1}). A scalar damage parameter can be defined from the reduction in stiffness when comparing the effective modulus during unloading with the initial modulus during loading:

$$D = 1 - \frac{E_{\text{unloading}}}{E_0} \quad (1)$$

Figure 4 shows the loading-unloading curves, as well as the damage parameter D vs. plastic strain determined from these curves.

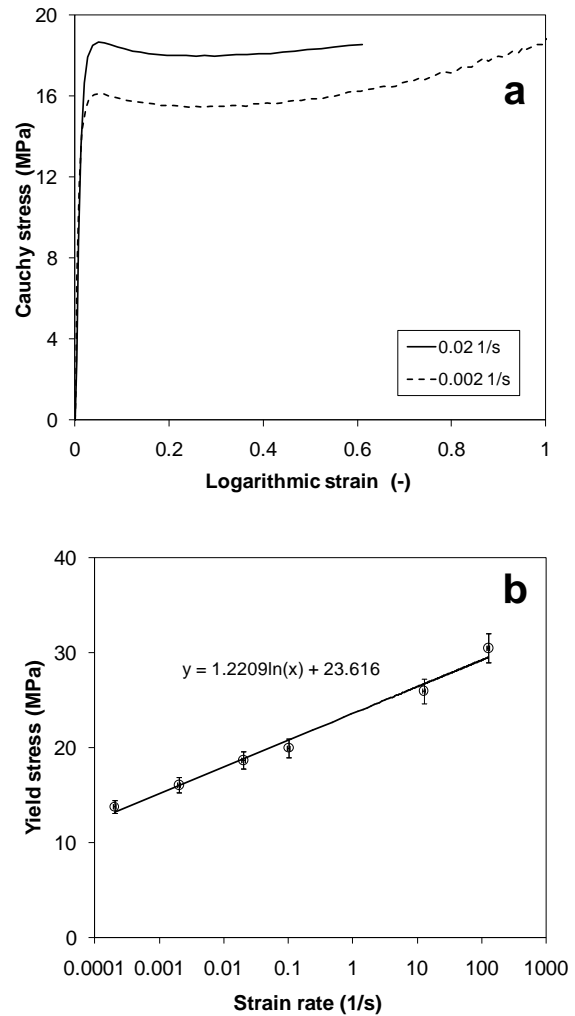


Figure 2 a) True tensile strain-stress curves for two different nominal strain rates. b) Tensile yield stress versus strain rate.

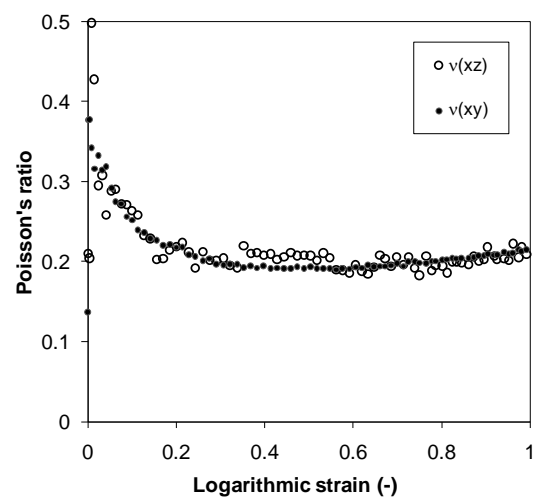


Figure 3 Poisson's ratio versus total strain in the two transverse directions of the tensile test specimen. The cross-head speed was 10 mm/min.

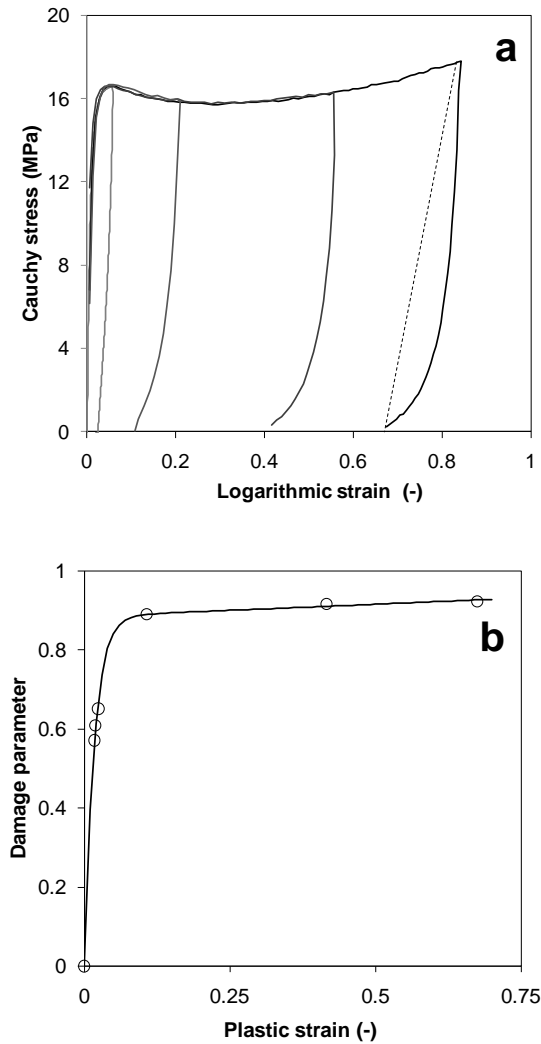


Figure 4 a) Uniaxial tensile loading-unloading curves. The dotted line shows the effective unloading modulus (it could also be defined in alternative ways) b) Damage parameter D versus plastic strain (circles) and two-term exponential fitted curve (line).

2.2.3 Uniaxial compression

Different specimen geometries were evaluated, with the aim to measure the true yield stress and true stress-strain up to large strains. All the specimens were loaded parallel to the flow direction of the injection-moulded part (dogbone or plate). Specimens with dimensions recommended by ISO 604 for compressive strength measurements (10 mm high, cross-section $4 \times 10 \text{ mm}^2$), machined from dogbones and tested without lubrication, gave the highest yield stress value (probably closest

to the true value), but buckling occurred at a nominal strain of ca 0.25. Specimens with dimensions $4 \times 4 \times 4 \text{ mm}^3$ gave only slightly lower yield stress (but much lower apparent modulus). These specimens were lubricated to reduce barrelling and associated inhomogeneous stress states. The contact surfaces were covered with PTFE tape and lubricated with soap water as in ref. [17]. With this lubrication, there was no significant barrelling at a nominal strain of 0.5, see Figure 5.

It should be noted that such small specimens behaved differently whether they were machined from dogbones or plates. In both cases two of the coplanar surfaces with normals perpendicular to the loading direction were the original as-moulded surfaces. However, for the specimens machined from dogbones the as-moulded surfaces barrelled considerably at a nominal strain of 0.5, while there was no significant barrelling for the other pair of surfaces (and not for the surfaces of specimens machined from plates, as mentioned above).

Hence, $4 \times 4 \times 4 \text{ mm}^3$ specimens machined from the middle of plates were used in the calibration tests. The true stress was calculated based on the actual cross-section in the midplane between the compression plates, as measured by DIC. The strain was measured by DIC at the centre points of two adjacent surfaces. As for the tensile tests, the two DIC cameras were adjusted so that both recorded both sides of the specimen, see Figure 5.

However, due to edge effects and imperfect specimen geometries (relative to the specimen size), causing inhomogeneous stress fields and stress states, the initial part of the recorded stress-strain curve was less steep than the true response (evidenced by comparing with data for specimens with higher aspect ratio). Also, the apparent modulus was lower than that obtained in tensile testing (it should be higher [18]). Hence, the compressive stress-strain used in the model calibration was scaled in order to have the same modulus as the

tensile data (the model has a pressure-independent modulus). The original and scaled curves are shown in Figure 6.

For larger strains, the use of DIC to measure the actual strains on the surface of the specimen, showed a considerable improvement compared to nominal strains based on cross-head displacement. There was also an improvement compared with strains based on longitudinal extensometry, because the constant volume assumption was not valid (the Poisson's ratio was lower than 0.5 after the yield point). However, the lateral strains were anisotropic, probably due to the restraining effect of the outer layers of the as-moulded surface, see Figure 7.

Finally, it should be mentioned that the scatter between repeated tests was relatively high. It was difficult to obtain coplanar and smooth surfaces when machining such small specimens of this rather soft material.

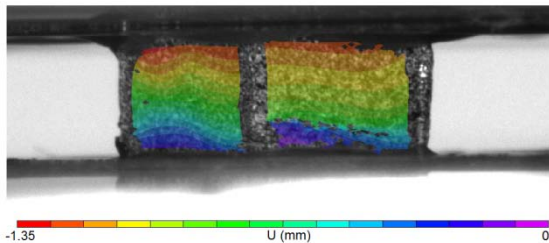


Figure 5 Deformation of a $4 \times 4 \times 4 \text{ mm}^3$ specimen (machined from a plate) at a nominal compressive strain of ca 0.5.

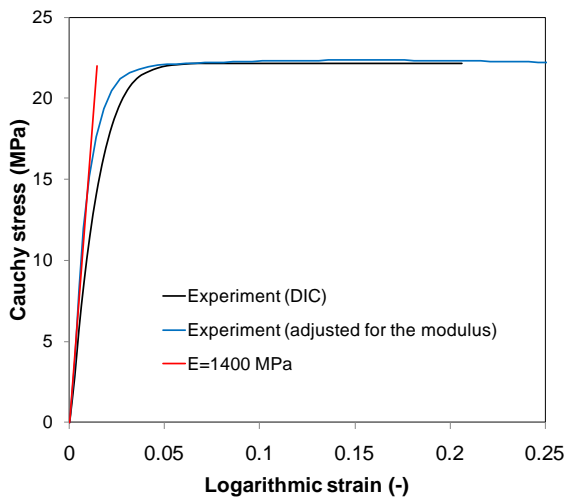


Figure 6 Original and scaled (corrected) stress vs. strain for compression testing at a strain rate of 0.002 s^{-1} .

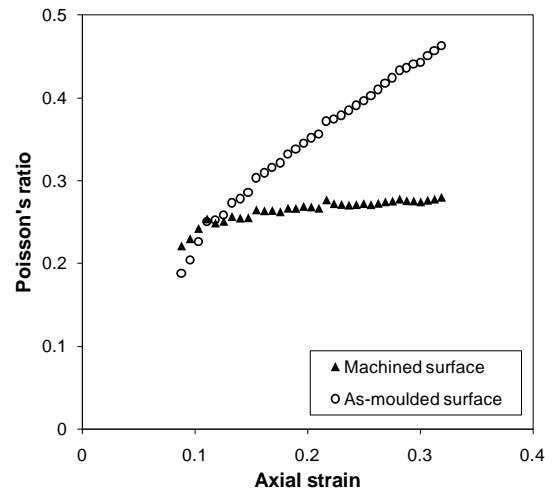


Figure 7 DIC measurements of Poisson's ratios of compressed $4 \times 4 \times 4 \text{ mm}^3$ specimen machined from a plate.

2.2.4 Shear

The in-plane shear response of injection-moulded plates of this material and two other PP materials was studied by the authors. Two common test methods were used: Iosipescu (ASTM D 5379) and V-Notched Rail (ASTM D 7078). The V-Notched Rail method gave slightly higher yield stress than the Iosipescu method at small strains. For the present paper the material model was calibrated with data obtained with the V-Notched Rail method. The stress was derived by assuming that the sheared cross-section remained constant during the test. The logarithmic shear strain was measured directly using DIC, see Figure 8.

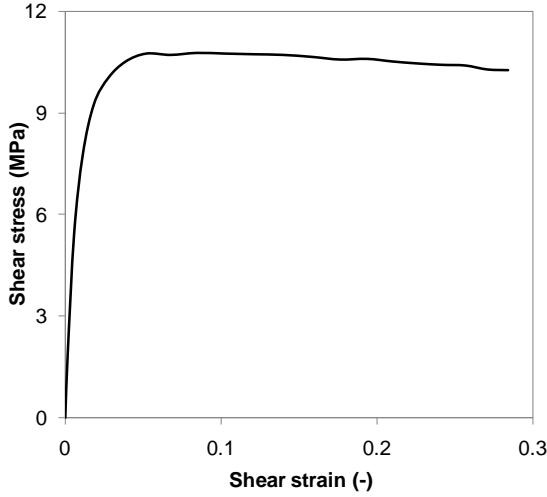


Figure 8 Shear stress vs. shear strain obtained with the V-Notched Rail method with a strain rate about 0.002 s^{-1} .

2.3 Verification tests

Two series of tests were performed for comparison with numerical simulations. Effects of strain rate, stress triaxiality and damage were assessed.

Centrally loaded clamped plates (falling-weight impact): Fully clamped 2 and 4 mm thick plates were subjected to impact loading based on the standard ISO 6603-2. The diameter of the plate inside the clamping was 40 mm. A hemispherical striker with diameter 20 mm was used. The striker was lubricated with silicone grease. The impact speeds were in the range 1–4.4 m/s and the drop mass was 3.5 kg. The force was logged at 100 kHz with a piezoelectric sensor. More details are given in refs. [1-2].

Three-point bending of bars (quasi-static and falling-weight impact): The test fixtures were according to ISO 178 (quasi-static tests at constant cross-head speed) and ISO 179 (falling-weight impact tests). Bars with cross-section $4 \times 10 \text{ mm}^2$ and length 80 mm were tested flatwise. The span was 60 mm. For the falling weight tests, the impact speeds were in the range 1–4 m/s and the drop weight was 3.5 kg.

3. Material model and finite element implementation

The material model SAMP-1 (Semi-Analytical Model for Polymers with C^1 -differentiable yield surface) was used in this study. SAMP-1 is a phenomenological model which has been developed for ductile polymer materials [10]. It is an isotropic elastic-viscoplastic model, and the simulated specimens were assumed to be homogeneous. SAMP-1 has a linear elastic response with no effect of stress state on the elastic modulus. The pressure dependent yield surface of SAMP-1 is defined by:

$$J_2 - A_0 + A_1 I_1 - A_2 I_1^2 = 0 \quad (2)$$

where I_1 is the first invariant of the stress tensor, J_2 is the second invariant of the deviatoric stress tensor, and A_0 , A_1 and A_2 are coefficients determined by measuring the yield stresses in three different stress states; uniaxial tension, shear and uniaxial compression in our study. From the calibration tests, the yield stress values for these three stress states were determined to be 10.4 MPa, 7.0 MPa and 14.2 MPa, respectively.

Three different yield surfaces were calibrated, referred to as von Mises ($A_1 = A_2 = 0$, based on tension), Drucker-Prager ($A_2 = 0$, based on tension and compression) and SAMP-1 (all coefficients used). The term A_2 is rather small for our data set, see Figure 9. The strain rate dependence was based on the tensile data in Figure 2b.

The generally non-associated flow potential of SAMP-1 is

$$g = \sqrt{3J_2 + \alpha I_1^2} \quad (3)$$

where α is a function of the plastic Poisson's ratio ν_p (which is a function of the plastic strain):

$$\alpha = \frac{1 - 2\nu_p}{2(1 + \nu_p)} \quad (4)$$

For the simulations reported in this paper, the potential was based on a constant value of 0.2 for v_p (ref. Figure 3). Other parameters, such as $v_p = 0.5$ (von Mises) for compression combined with v_p following the curve in Figure 3 for tension, did not have a large effect on the simulated force-displacement curves.

The hardening curves in the mode, for all stress states, are based on scaling a curve from quasi-static uniaxial testing.

The damage parameter was given by Eq. (1) with data from Figure 4b. This parameter was then independent of stress state and strain rate (only indirect dependence via the plastic strain).

The commercial finite element code LS-DYNA (1s971_d_R4.2.1) was used in this study. Two element types were used to simulate the verification tests.

The geometry for three-point bending was modelled with 8-node hexahedron solid elements with reduced integration and Flanagan-Belytschko stiffness-based hour-[14] glass control, using ten elements through the beam thickness.

The 2 mm thick plate underwent a large local deformation under the striker, and a fine mesh was needed to capture this. For this reason, 4-node axisymmetric solid elements were used to model striker, plate and clamping. There were 10 elements through the thickness of the 2 mm thick plate, and 20 elements through the 4 mm thick plate. Again, reduced integration and Flanagan-Belytschko stiffness-based hour-glass control was used.

Coloumb friction was implemented, with friction coefficients 0.05 and 0.2 for lubricated and unlubricated surfaces, respectively.

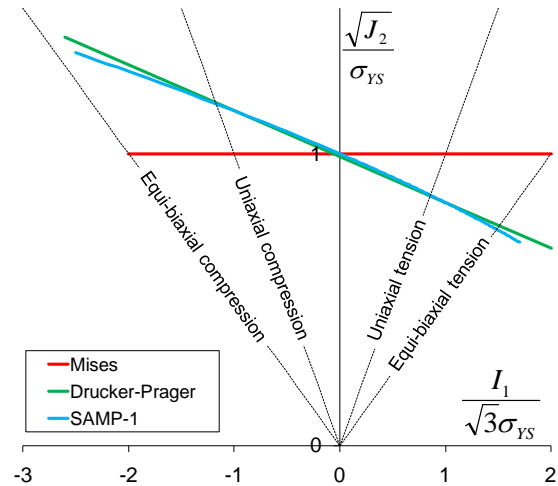


Figure 9 Yield surfaces mentioned in the main text. I_1 is the first invariant of the stress tensor, J_2 is the second invariant of the deviatoric stress tensor, and σ_{YS} is the yield stress in shear.

4. Results

Some comparisons between simulated and measured responses are shown below. For three-point bending, the quasi-static test and impact tests at low loading rates are well predicted (Figure 10a and Figure 10b). However, the maximum force in the test at 4 m/s is underpredicted (Figure 10c).

Regarding the falling-weight impact of clamped plates, the response of the 4 mm thick plate appears to be well predicted at impact speeds up to 3 m/s, see Figure 11. At the same impact speed, the response of the 2 mm thick plate (Figure 12) is well is predicted for small displacements. For larger displacements, SAMP-1 underpredicts the force, although the maximum force appears to be well predicted, see Figure 12. However, the thinning of the plate is not predicted, see Figure 13. The same deviation was also observed for the 4 mm plate at a loading rate of 4.4 m/s.

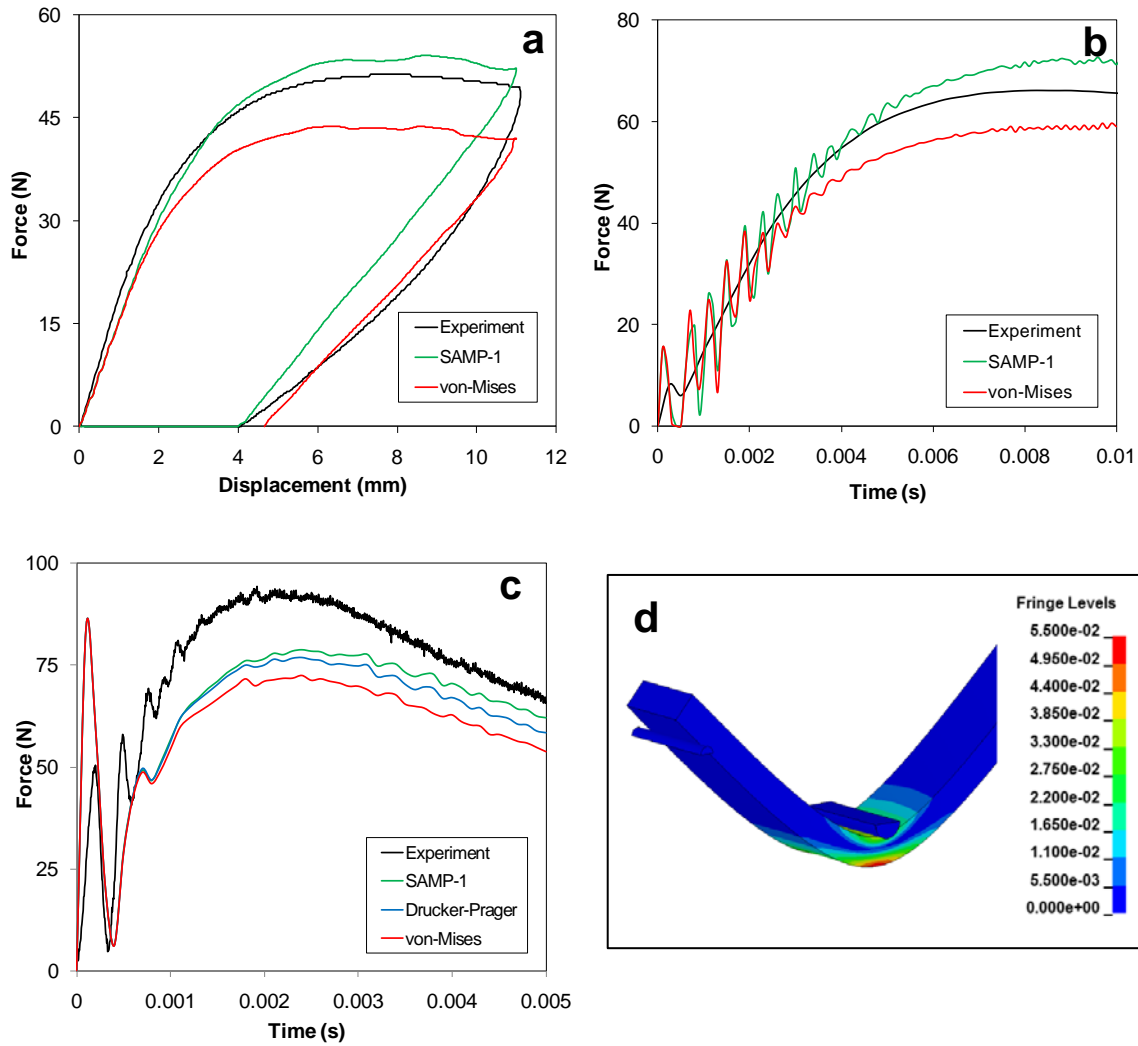


Figure 10 Results for three-point bending. Experimental data were obtained with bars from dogbones. a) Constant loading and unloading rate 10 mm/min. b) Falling-weight impact at 1 m/s. c) Falling-weight impact at 4 m/s. d) Simulated effective plastic strains after 5 ms for falling-weight impact at 4 m/s.

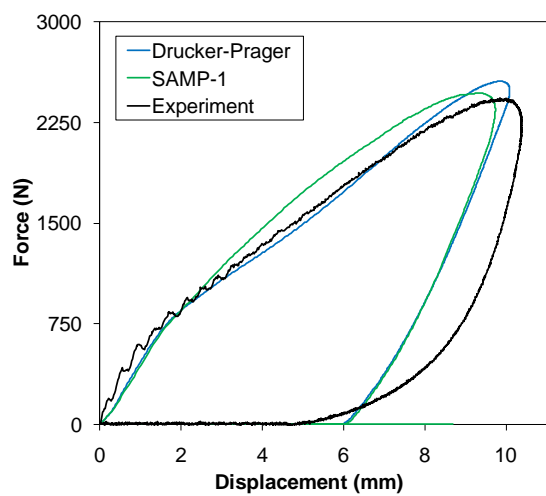


Figure 11 Falling-weight impact on 4 mm thick plate. Impact speed 3 m/s.

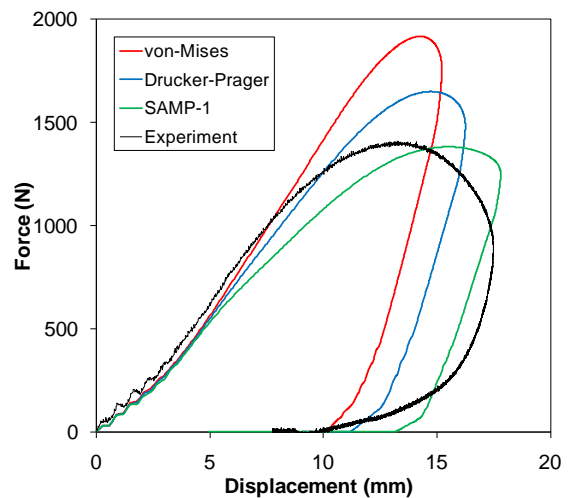


Figure 12 Falling weight impact on 2 mm thick plate. Impact speed 3 m/s.

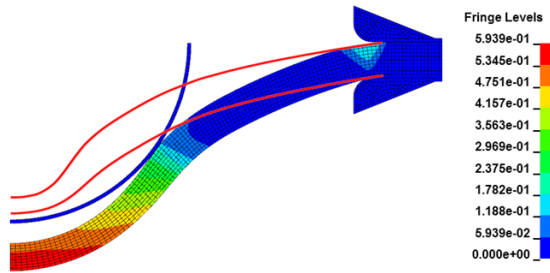


Figure 13 Comparison between measured cross-section (red lines, measured with DIC) and simulated cross-section of plate after unloading (permanent deformation). Data for 2 mm thick plate and impact speed 3 m/s. The contour plot shows the plastic strains as the striker rebounds.

5. Discussion

5.1 General

The model used in this study is based on a number of assumptions and simplifications. Whether these are valid or not will depend on factors such as loading/geometry, material characteristics (ductility, hardening curve etc), mechanical parameter(s) to be predicted (stiffness, absorbed energy etc) and the required accuracy of the simulations.

The model does not take into account the anisotropy and the heterogeneity of injection-moulded parts. The anisotropy is caused by the orientation of polymer chains and crystallites, which is induced by the moulding process. The heterogeneity is a result of the spatial variation in the thermo-mechanical conditions during moulding, resulting in a variation in properties through the cross-section of the part, and along the flow path. Anisotropy and heterogeneity can be assessed by testing specimens parallel and perpendicular to the flow direction, in bending (Figure 1) and tension, and by testing specimens with different fraction of the surface machined off. We plan to return to this in a forthcoming paper. One way to include the anisotropy effect in the simulations would be to represent the moulded part as a sandwich consisting of a core and a skin layer with different properties [14].

The elasticity of the model is linear and independent of stress state and strain rate. This is OK for ductile materials when the initial elastic response is a very small part of the total response. The unloading response of the model is linear-elastic, with an unloading modulus which is reduced relative to the initial modulus via a damage parameter, which is independent of stress state and strain rate. For more realistic simulations of the unloading response, other elastic models are required (hyperelastic, viscoelastic, anisotropic, temperature-dependent).

The SAMP-1 yield surface (Eq. 2) takes into account the pressure-dependence which is important for polymers. Furthermore, the quadratic expression allows for a more detailed representation of the yield surface (if data for more than three stress states are available, the model can be fitted to the data). The strain rate dependence of the yield stress can be represented freely in tabulated form, but in the model the dependence must be the same for all stress states. For the low strain rates used in other stress states than uniaxial tension in the present study ($< 1 \text{ s}^{-1}$), there was no significant effect of stress state on the strain rate sensitivity. However, Delhaye et al. [19] reported that the strain rate sensitivity increased with increasing pressure. Finally, the non-associated flow potential of SAMP-1 is rather simple, but it can represent the same main features as e.g. the model in ref. [8].

5.2 Three-point bending

The simplest validation test, quasi-static three-point bending, is well predicted (Figure 10a). During loading the force is slightly underpredicted at small deflections, and slightly overpredicted at larger deflections. The initial underprediction could be due to the compressive modulus being equal to the tensile modulus in the model. The overprediction could indicate that the compressive yield stress in the model was somewhat too high. Different hardening curves in tension and compression could also be a factor. Other factors could also

contribute to the overprediction, such as variation in properties through the cross-section of the bar (not included in the model) or an inadequate friction model. The simulated unloading response is as expected with this model, and it is OK for many industrial applications. The quasi-static three-point bending test can be a reference point for discussing the other validation tests below.

For the falling-weight impact bending tests, the difference between measured and simulated responses seems to increase with increasing loading rate (Figure 10b and Figure 10c). The force is underpredicted at the highest loading rate (Figure 10c). This could indicate that the strain rate dependence of the model needs to be improved. Initially, the simulated force is probably too low because viscoelasticity is neglected. At larger strains the underprediction could be related to the yield stress and/or the hardening curves. The calibration data for uniaxial compression are perhaps the most uncertain. Also, the tensile yield stress data (used for all stress states in the model) at the highest strain rates are the most uncertain, and the strain rate sensitivity may be higher for compression than for tension at the highest relevant rates [19].

Our model was based on a linear relation between yield stress and strain rate on a logarithmic scale (Figure 2b). However, the data in Figure 2b do not rule out a nonlinear strain rate dependence. Nonlinear dependencies have been reported for polypropylene in compression tests [6, 20-21]. Above a strain rate of about 100 s^{-1} the strain rate sensitivity was higher, and this was explained by the β relaxation process taking over for the α relaxation. The maximum strain rate in our simulation of the bending at 4 m/s was around 120 s^{-1} . If a nonlinear strain rate sensitivity, in line with refs. [6, 20-21], is assumed for both compression and tension, the simulated maximum force would be about 5 % higher. The experimental curve in Figure 10c would still be underpredicted.

Other shortcomings of the model could also be responsible for the underprediction in Figure 10c. This could e.g. be related to friction at the supports (this was checked, and the friction coefficient value only affected the curve after the maximum force) and indentation at the supports and under the striker (the indentation of the skin layer of the injection-moulded parts may not be well described by the model). Also note that the force oscillations are larger in the simulations than in the experiments. The variation in microstructure and mechanical properties through the cross-section of the injection-moulded beam could also play a role. Viana [14] reported that the yield stress of the core had higher strain rate sensitivity than that of the skin. In our case, the core contributed more in the calibration tests (Sect. 2.2) than in this bending verification test. Hence, the effect reported by Viana would rather have caused an overprediction of the strain rate sensitivity for bending.

5.3 Centrally loaded plate

The falling weight impact of the 4 mm thick plate (Figure 11) differs from the three-point bending of the 4 mm thick beam (Figure 10c) by having a stress state close to biaxial tension in some of the elements. The strains and strain rates were somewhat lower in the former case, partly due to the lower impact speed (3 vs. 4 m/s). Also, the plate impact test has more non-linearity due to the increase in contact area between the plate and the hemispherical striker during loading.

With our model, the plate impact test (Figure 12) seems to be better predicted than the three-point bending impact test (Figure 10c). This may, however, be the result of some neglected factors or shortcomings contributing to a higher force compensating for some which contribute to a lower force. Firstly, the anisotropy of the plate was not included in the model. As shown in Figure 1, a bar cut from the plate in the direction perpendicular to flow is less stiff than a bar cut parallel to flow, and

the model was calibrated with a specimens loaded along the flow direction. Hence, our model overpredicts the bending stiffness of the centrally loaded plate by neglecting this anisotropy. Secondly, the material may soften in biaxial tension and also biaxial compression, compared to the uniaxial stress states [11]. This is only indirectly included in our model, via the yield surface (Figure 9) giving a lower yield stress in biaxial tension than in uniaxial tension. However, if data for biaxial tension would show a stronger softening than our model, our model overpredicts the response. Thirdly, we are probably still underpredicting the strain rate dependence, as for the three-point bending in Figure 10c. However, it may be that with a stress state with less pressure, such as a centrally loaded plate, (compare the effects of the yield surfaces in Figure 12 and Figure 10c), the average strain rate dependence may be lower [19].

The last validation test is the falling-weight impact of the 2 mm thick plate (Figure 12 and Figure 13). In this test the strains are larger than for the 4 mm thick plate. The average stress state is also different in the domains with the largest strains. The most notable deficiency of the simulation is the fact that it fails to predict the localised thinning (Figure 13). This fact indicates that our model is not adequate for this case of biaxial drawing. Some model parameters were varied to see if thinning could occur. Numerical stability prevented the exploration of a lower yield stress in biaxial tension (lower than in Figure 9), probably due to the hardening curves. We will follow up this in further studies. Thinning occurred if a von Mises flow potential was used ($v_p = 0.5$), but this is not realistic, unless the microstructure has been transformed so that the material is isochoric at this stage. In any case, the thinning mechanism is probably affected by the reorganisation of the microstructure at these large strains (to such an extent that the calibration data may no longer be valid), leading to localised softening. Friction [1, 5, 22] and dissipative heating are

also important factors. Viscoelastic effects are also involved, as witnessed by the difference between the striker shape and the permanent shape of the deformed plate (Figure 13).

Thermo-mechanical coupling can be important at these high strain rates [5, 11], and local heating and plastic straining may accelerate each other. An adiabatic simulation of the 3 m/s impact of the 2 mm thick plate showed a localised temperature rise of approximately 20 °C, while the temperature rise was only a few degrees (less localised) for the 4 m/s impact bending of the 4 mm thick bar. Furthermore, Viana [14] reported that the yield stress of the skin layer of an injection-moulded part had higher temperature sensitivity than that of the core. The heating will mainly affect the force near and after the maximum. Hence, if a thermo-mechanical coupling was included in the model, the maximum force may still be reasonably well predicted.

6. Conclusion and final remarks

The SAMP-1 model seems to be suitable for simulating impact loading of such ductile polypropylene compounds in an industrial setting. Most of the key features of the mechanical response of ductile polymer materials are contained in this model. However, some of the verification cases were not satisfactory predicted.

A number of possible improvements should be considered. Some of these are related to the calibration testing in well-defined stress states, some are related to the heterogeneity and anisotropy of the injection-moulded parts, and some are related to shortcomings of the model. It should be noted, however, that with this rather complex material behaviour it is often difficult to separate the effects.

Regarding the calibration tests, these need to be analysed and developed further, so that we can get even closer to the true intrinsic response. In particular, this applies to the response at large strains and in biaxial tension.

At high strain rates, DIC must be used and special data analysis methods [23] need to be developed. Calibration tests should also be performed at different temperatures.

Regarding the SAMP-1 model, some features are clearly missing, such as viscoelasticity. However, the cost and labour involved in testing and model calibration must always be considered vs. the predictive power of the simulations. For the academic community, models based on polymer physics, micromechanical mechanisms and microstructure development are preferred. Gradually, features from these models will be implemented in models for industrial use. However, note that polypropylene-based compounds, such as the one used in the present study, have a complex molecular and composite structure.

Inverse modelling can be utilised to improve both calibration tests and models.

Acknowledgments

The authors would like to thank the Research Council of Norway (BIA programme) and Plastal AS for financial support, and for the PhD studentship grant to Hamid Daiyan.

References

- [1] H. Daiyan, E. Andreassen, F. Grytten, O.V. Lyngstad, T. Luksepp, H. Osnes, Low-velocity impact response of injection-moulded polypropylene plates - Part 1: Effects of plate thickness, impact velocity and temperature, *Polym. Test.*, 29 (2010) 648-657.
- [2] H. Daiyan, E. Andreassen, F. Grytten, O.V. Lyngstad, T. Luksepp, H. Osnes, Low-velocity impact response of injection-moulded polypropylene plates - Part 2: Effects of moulding conditions, striker geometry, clamping, surface texture, weld line and paint, *Polym. Test.*, 29 (2010) 894-901.
- [3] C. G'Sell, N.A. Aly-Helal, J.J. Jonas, Effect of stress triaxiality on neck propagation during the tensile stretching of solid polymers, *J. Mater. Sci.*, 18 (1983) 1731-1742.
- [4] Y. Tillier, Mechanical characterization of solid polymers using inverse analysis: application to high velocity and multiaxial tests, PhD thesis Sciences et Génie des Matériaux, CEMEF Centre de Mise en Forme des Matériaux (1998).
- [5] J.C. Viana, A.M. Cunha, N. Billon, Experimental characterization and computational simulations of the impact behavior of injection-molded polymers, *Polym. Eng. Sci.*, 47 (2007) 337-346.
- [6] Y. Wang, E.M. Arruda, Constitutive modeling of a thermoplastic olefin over a broad range of strain rates, *Journal of Engineering Materials and Technology-Transactions of the ASME*, 128 (2006) 551-558.
- [7] Q. Ma, X. Su, Z. Lin, J. Lasecki, X. Lai, A constitutive model for the nonlinear viscoplastic behavior of thermoplastic olefin, *Polym. Compos.*, 31 (2010) 587-595.
- [8] G. Dean, L. Crocker, Prediction of impact performance of plastics mouldings. Part 1: Material models and determination of properties, *Plast. Rubber Compos.*, 36 (2007) 1-13.
- [9] M. Polanco-Loria, A.H. Clausen, T. Berstad, O.S. Hopperstad, Constitutive model for thermoplastics with structural applications, *Int. J. Impact Eng.*, 37 (2010) 1207-1219.
- [10] S. Kolling, A. Haufe, M. Feucht, P. Du Bois, SAMP-1: A Semi-Analytical Model for the Simulation of Polymers, in: *LS-DYNA Anwenderforum*, 2005, pp. 26.
- [11] N. Temimi-Maaref, A. Burr, N. Billon, Damaging processes in polypropylene compound: Experiment and modeling, *Polymer Science Series A*, 50 (2008) 558-567.
- [12] M.C. Branciforti, C.A. Oliveira, J.A. de Sousa, Molecular orientation, crystallinity, and flexural modulus correlations in injection molded polypropylene/talc composites, *Polym. Adv. Technol.*, 21 (2010) 322-330.
- [13] B. Fisa, A. Meddad, Weldlines, in: J. Karger-Kocsis (Ed.) *Polypropylene: An A-Z Reference*, Kluwer Publisher, 1999.
- [14] J.C. Viana, Structural interpretation of the strain-rate, temperature and morphology dependence of the yield stress of injection molded semicrystalline polymers, *Polymer*, 46 (2005) 11773-11785.
- [15] F. Grytten, H. Daiyan, M. Polanco-Loria, S. Dumoulin, Use of digital image correlation to measure large-strain tensile properties of ductile thermoplastics, *Polym. Test.*, 28 (2009) 653-660.
- [16] J. Lemaitre, *A course on damage mechanics*, Springer-Verlag, Berlin, 1992.
- [17] B.A.G. Schrauwen, R.P.M. Janssen, L.E. Govaert, H.E.H. Meijer, Intrinsic deformation behavior of semicrystalline polymers, *Macromolecules*, 37 (2004) 6069-6078.
- [18] M. Jerabek, Z. Major, R.W. Lang, Uniaxial compression testing of polymeric materials, *Polym. Test.*, 29 (2010) 302-309.

- [19] V. Delhayé, A.H. Clausen, F. Moussy, O.S. Hopperstad, R. Othman, Mechanical response and microstructure investigation of a mineral and rubber modified polypropylene, *Polym. Test.*, 29 (2010) 793-802.
- [20] P. Buckley, Constitutive modelling of solid polymers: strategies for spanning wide ranges of temperature, strain and strain-rate, in: *International workshop on behaviour and modelling of polymers*, Trondheim, Norway, 2009.
- [21] M. Okereke, C.P. Buckley, High-rate compression of polypropylene, in: D. Acierno, A. Damore, L. Grassia (Eds.) *IVth International Conference on Times of Polymers*, 2008, pp. 18-20.
- [22] Z. Marciniak, J.L. Duncan, S.J. Hu, Ch 9, in: *Mechanics of Sheet Metal Forming*, Butterworth-Heinemann, 2002.
- [23] F. Lauro, B. Bennani, D. Morin, A.F. Epee, The SEE method for determination of behaviour laws for strain rate dependent material: Application to polymer material, *Int. J. Impact Eng.*, 37 (2010) 715-722.

Paper 6

M. Polanco-Loria, H. Daiyan, F. Grytten

Material parameters identification: An inverse modelling procedure applicable for thermoplastic materials

Accepted for publication, Polymer Engineering & Science, 2011

Material parameters identification: An inverse modeling methodology applicable for thermoplastic materials

M. Polanco-Loria^{1,*}, H. Daiyan² and F. Grytten²

¹ SINTEF Materials and Chemistry, Department of Applied Mechanics and Corrosion, NO-7465, Trondheim, Norway.

² SINTEF Materials and Chemistry, Department of Synthesis and Properties, NO-0314, Oslo, Norway.

Abstract

The methodology proposed in this work uses the local measured strain rate history as the applied “load” to the FE “material point”. Next, with this strain rate history, two objective functions related to the true stress-strain and volumetric strain response can be minimized to identify some of the material parameters of the constitutive model. The whole identification process, of the 9 material parameters required, is described in detail. In addition, a short description of the constitutive model used is given with an experimental program including mainly uniaxial tensile tests at different strain rates. 3D digital image correlation is used to determine full-field displacements and deduce true stress-strain, volume dilatation and local strain rates curves during deformation.

1. Introduction

Polymers are widely used in the transport industry, specially, when structural components and passengers/pedestrian safety are in focus. The experience in using polymers in impact protection and structural systems, however, is limited, and there are several challenges which call for research. One of the most obvious is the lack of robust material models in commercial finite element codes and in order to address this issue a new hyperelastic-viscoplastic constitutive model has been developed by Polanco-Loria et al. [1-3]. This model, limited to isothermal conditions, is able to handle finite deformations, pressure and rate sensitivity and non-isochoric plastic flow.

Development of new material models also involves experimental efforts where well defined material tests are required for calibration of the parameters in the model. Thereafter, it is common to validate the proposed material model by doing numerical predictions of a component test which serves as an independent check of the capabilities

of the model. At present, the static uniaxial tension test is the simplest mechanical test used for material characterization. However, for polymeric materials measurements of the true tensile stress-strain are difficult, in particular, when neck propagation and volumetric plastic strains are present during the deformation process. It seems that only optical-based systems should be used for a reliable material characterization when dealing with polymeric materials, as one can confirm from the literature [4-10].

On the other hand, extraction of experimental data and its utilization for material calibration purposes can be cumbersome because constitutive relations of polymers are strain, strain rate and temperature dependent. In particular after necking (e.g. strain localization), two basic problems are commonly observed: an non-homogenous increase of the local strain rate when compared to the global applied one; and an non-homogenous increase of temperature due to the low heat conduction capacity of polymers (e.g. adiabatic

* Corresponding author. Tel.: +47 98230435; fax: +47 73592931
E-mail address: mario.polanco@sintef.no (M. Polanco-Loria).

process). In addition, the variables involved in the thermo-mechanical characterization are highly coupled; consequently, material identification by trial and error procedures can be inefficient for such complex materials. Alternatively, nonlinear inverse computational methods have been applied to identify material parameters (see for instance references [11-16]) in cases where the parameters are not directly measurable or the deformations fields are of heterogeneous nature (e.g. complex boundary conditions, loss of homogeneity during the deformation process, among others). In addition, these nonlinear mathematical techniques are largely used during the design and performance of complex structures (e.g. crashworthiness) and the numerical simulation of complex manufacturing processes (e.g. forming, extrusion, molding). The basic principle of the inverse method, for parameter identification purposes, is illustrated in Figure 1.

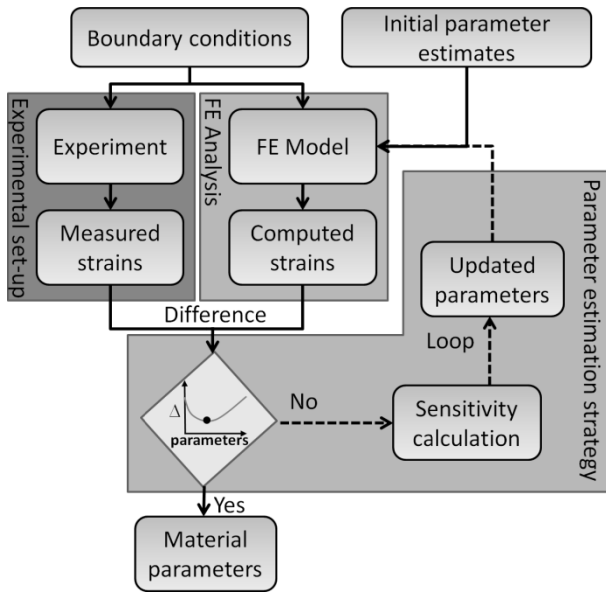


Figure 1 Basic principle of the inverse modeling approach for material identification purposes [12].

The objective of the present work is to describe a simple inverse modeling methodology to identify the material parameters of the recently developed constitutive model for thermoplastic materials [3]. For this purpose, an experimental program including uniaxial tensile and compression tests is performed on a mineral and rubber modified polypropylene compound. In addition, the optimization software LS-OPT [17] is used to demonstrate the identification procedure.

2. The modified Boyce-Raghava model for thermoplastic materials

The model presented here, limited to isothermal conditions, is a physically-based constitutive model, involving the typical mechanisms of the elastic behavior of polymers, i.e. relative rotation around backbone carbon-carbon bonds and entropy change by un-coiling molecule chains. In addition, viscoplastic flow associated with relative movement between molecules is included. Historically, the development of this model goes back to the work by Haward and Thackray [18] and further developed by Boyce [19] and Boyce et al. [20], who assumed that the total stress was the sum of an inter-molecular and intra-molecular contribution denoted A and B, respectively:

- A). An inter-molecular barrier to deformation related to relative movement between molecules.
- B). A network (entropic) resistance related to straightening of the molecule chains.

According to the rheological model shown in Figure 2, the two resistances A and B are assumed to have the same deformation gradient, i.e. $\mathbf{F} = \mathbf{F}_A = \mathbf{F}_B$, while the Cauchy stress tensor is obtained by summing the contributions from Parts A and B. The deformation gradient \mathbf{F}_A (part A) is decomposed into the elastic and the plastic parts, i.e. $\mathbf{F}_A = \mathbf{F}_A^e \cdot \mathbf{F}_A^p$. Similarly, the Jacobian is decomposed in a multiplicative way, i.e.

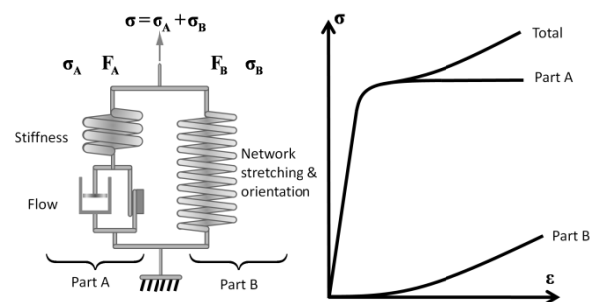


Figure 2 MBR constitutive model with inter-molecular (A) and network (B) contributions.

$J_A = \det \mathbf{F}_A = J_A^e J_A^p = J$. Next, a compressible Neo-Hookean material is chosen for the elastic part of the deformation, and the Cauchy stress

tensor $\boldsymbol{\sigma}_A$ reads

$$\boldsymbol{\sigma}_A = \frac{1}{J_A^e} \left[\lambda \ln J_A^e \mathbf{I} + \mu (\mathbf{B}_A^e - \mathbf{I}) \right] \quad (1)$$

where λ and μ are the classical Lamé constants of the linearized theory, $\mathbf{B}_A^e = \mathbf{F}_A^e \cdot (\mathbf{F}_A^e)^T$ is the elastic left Cauchy-Green deformation tensor, and \mathbf{I} is the second order unit tensor. The coefficients λ and μ may alternatively be expressed as functions of Young's modulus E and Poisson's ratio ν .

The yield criterion is assumed in the form $f_A = \bar{\sigma}_A - \sigma_T = 0$, where σ_T is the uniaxial yield stress in tension. The equivalent stress $\bar{\sigma}_A$ accounts for the pressure-sensitive behavior and is defined according to Raghava et al. [21] as:

$$\bar{\sigma}_A = \frac{(\alpha - 1)I_{1A} + \sqrt{(\alpha - 1)^2 I_{1A}^2 + 12\alpha J_{2A}}}{2\alpha} \quad (2)$$

The material parameter $\alpha = \sigma_c / \sigma_T \geq 1$ describes the pressure sensitivity, where σ_c is the uniaxial compressive yield strength of the material, I_{1A} and J_{2A} are the stress invariants related to respectively the volumetric and the deviatoric Cauchy stress tensor. In order to control the plastic dilatation, a non-associative flow rule is introduced where a Raghava-like plastic potential g_A is defined as

$$g_A = \frac{(\beta - 1)I_{1A} + \sqrt{(\beta - 1)^2 I_{1A}^2 + 12\beta J_{2A}}}{2\beta} \geq 0 \quad (3)$$

where $\beta \geq 1$ is a material parameter introduced to control the volumetric plastic strain. The flow rule gives the plastic rate-of-deformation tensor \mathbf{D}_A^p , as

$$\mathbf{D}_A^p = \dot{\bar{\epsilon}}_A^p \frac{\partial g_A}{\partial \boldsymbol{\sigma}_A} \quad (4)$$

where the equivalent plastic strain rate $\dot{\bar{\epsilon}}_A^p$, is chosen as

$$\dot{\bar{\epsilon}}_A^p = \begin{cases} 0 & \text{if } f_A \leq 0 \\ \dot{\epsilon}_0 \left\{ \exp \left[\frac{1}{C} \left(\frac{\bar{\sigma}_A}{\sigma_T} - 1 \right) \right] - 1 \right\} & \text{if } f_A > 0 \end{cases} \quad (5)$$

here the two coefficients C and $\dot{\epsilon}_0$ are material parameters easy to identify from uniaxial strain-rate tests.

The part B includes the deformation gradient $\mathbf{F}_B = \mathbf{F}_A = \mathbf{F}$, representing the network orientation. The network resistance is assumed to be hyperelastic. The Cauchy stress-stretch relation is used as the original definition of Boyce et al. [20]:

$$\boldsymbol{\sigma}_B = \frac{1}{J} \left[\frac{C_R}{3} \frac{\sqrt{N}}{\bar{\lambda}} L^{-1} \left(\frac{\bar{\lambda}}{\sqrt{N}} \right) (\mathbf{B}_B^* - \bar{\lambda}^2 \mathbf{I}) \right] \quad (6)$$

where $J = J_B = \det \mathbf{F}_B$ is the Jacobian, and L^{-1} is the inverse of the Langevin function defined as $L(x) = \coth x - 1/x$. The equivalent

distortional stretch is $\bar{\lambda} = \sqrt{\frac{1}{3} \text{tr}(\mathbf{B}_B^*)}$ and

$\mathbf{B}_B^* = \mathbf{F}_B^* \cdot (\mathbf{F}_B^*)^T$ is the distortional left Cauchy-Green deformation tensor. In this Equation $\mathbf{F}_B^* = J_B^{-1/3} \mathbf{F}_B$ represents the distortional part of \mathbf{F}_B . There are two material parameters describing the network resistance: C_R is the initial elastic modulus of Part B and N can be interpreted as the number of "rigid links" between the entanglements of the molecule chains (which can be related to a maximum attainable stretching).

Finally, the Cauchy stress tensor for the material is obtained by summing the contributions of parts A and B, i.e.

$$\boldsymbol{\sigma} = \boldsymbol{\sigma}_A + \boldsymbol{\sigma}_B \quad (7)$$

The stress update algorithm applied herein is valid for general rate-dependent hyperelastic-plastic formulations. The update scheme was proposed by Moran et al. [22] and is semi-implicit. Since the constitutive model is developed for explicit finite element analysis, it is assumed that the time steps are small and that a semi-implicit algorithm is

sufficiently accurate. The constitutive model was implemented as a user-defined model in the finite element code LS-DYNA [23]. Finally, because the source of inspiration of the present model is based on the work of Boyce and Raghava with some new features the model will be referred here as the modified Boyce-Raghava (MBR) model. Some examples of structural applications (e.g. three point bending beams and centrally loaded plates) with an in deep discussion of results and parameters identification are provided in the original reference [3].

3. Experimental data using a PP copolymer material

3.1 Introduction

In order to illustrate the material calibration process the experimental results presented here are complemented with the data obtained by Grytten et al. [24]. The material investigated in this study is a commercial impact-modified polypropylene used for injection molded automotive exterior parts. This is a 20 % mineral filled and rubber modified polypropylene compound. Tensile injection molded test specimens (type 1A of the ISO 527-2:1993) of 4 mm thickness were used. For digital image correlation (DIC) measurements a random black and white speckle pattern was applied to both the front and lateral side of the specimen prior to testing using mat spray paint. The commercial DIC system Vic3D [25] was used to measure the displacement field during loading.

Four tensile tests were carried out in a Zwick Z250 universal test machine at 23 °C using constant cross head speeds of 1, 10, 100 and 500 mm/min. The length of the narrow portion of the specimen was 80 mm, resulting in nominal strain rates of 2×10^{-4} , 2×10^{-3} , 2×10^{-2} and $1 \times 10^{-1} \text{ s}^{-1}$, respectively. The influence of the strain rate response on the four nominal stress–strain curves is illustrated in Figure 3a while Figure 3b indicates the increase of the nominal stress with strain rate (taken at a strain level of 3 %). The load was measured with a 2.5 kN load cell and the signal was logged using a 12 bit National Instruments DAQCard 6062E. DIC technique was used in two of the four tensile tests. The experimental program included in addition, compression tests on a cubic specimen of 4x4x4 mm at a loading speed of 2 mm/min. No DIC measurements were used for the compression tests.

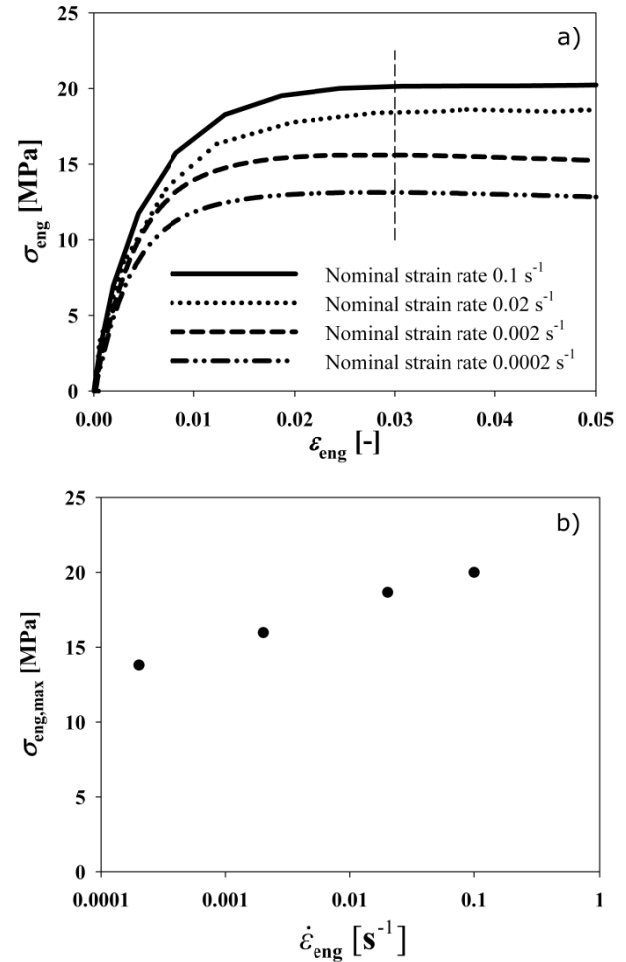


Figure 3 a) Nominal stress-strain response for different strain rates, b) Max stress (at strain level of 3 %) for different strain rates.

3.2 Global strain rate sensitivity based on tensile tests

For the DIC measurements an “area of interest” (AOI) was defined for each of the two faces visible to the two cameras used. Inside the AOI a “critical” section was always monitored where all post-processing data was taken from. This “critical” section was adopted based on observations of repeated events of necking occurrence for the geometry and material used. A more in-depth description of the test procedure can be seen in the work of Grytten et al. [24]. Other alternatives (e.g. introduction of a smooth notch [5, 7] or a geometrical imperfection [4, 6, 8]) have been used to define the “critical” section.

For the purpose of this work only one tensile test (actually two parallels) with DIC technique is

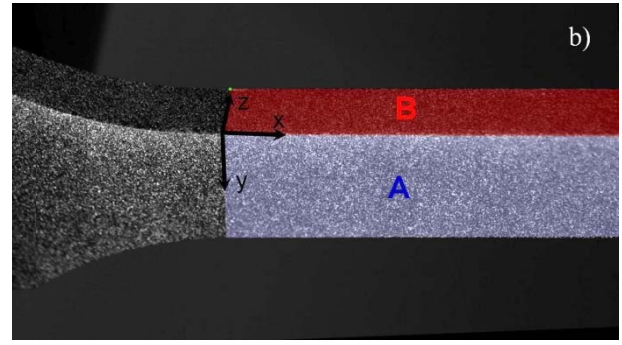
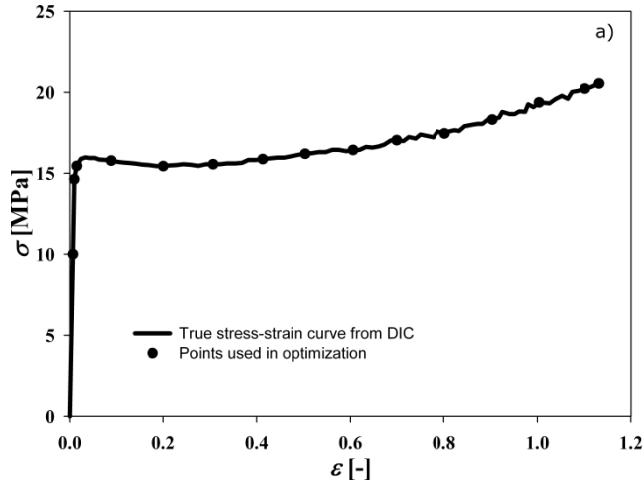


Figure 4 a) True stress-strain curve deduced from DIC measurements, b) Area of Interest (AOI) [24].

used here to deduce the true stress-strain curve, as reported in [24]. Indeed, the uniaxial tensile test loaded at a nominal strain rate of $2 \times 10^{-2} \text{ s}^{-1}$ is considered in this work. A full-field measurement of deformation is important because many polymers present volumetric plastic contribution during plastic flow [4, 6-9, 24, 26-28] requiring the monitoring of the actual cross section for true stress calculations purposes.

Different video system solutions have been reported in the literature attempting to measure the true stress-strain relation of polymers. With only one camera the images can only give the strain components at one surface of the specimen, i.e. at one coordinate plane. In the literature, true stresses have been calculated using the transversal strain and assuming transversal isotropy [4-5, 7-8, 24, 27-28] or using of one camera with a right-angle prism (measuring strain fields on both sides of a rectangular specimen) [9-10]. However, the results presented here (Grytten et al. [24]) are based on a set-up including 3D DIC with two cameras and stereo vision. Hence, the common assumption of transversal isotropy is not required in this set-up. Two cameras based system were also used in [6].

The true stress-strain curve deduced from DIC analysis is provided in Figure 4a. This figure represents the average response of two parallels. The stress-strain curve is also characterized by some discrete black points which will be used later as the target solution for the calibration procedure. Figure 4b illustrates the AOI adopted in this test. As previously mentioned, this test was run under displacement control with a nominal strain rate of $2 \times 10^{-2} \text{ s}^{-1}$. Generally, because of necking and cold drawing process, local strain rate is function of the

position (section) along the coupon as well as time, thus, each cross section is submitted to local strain rate variations during the deformation process. In other words, each of the experimental points that conforms the deduced true stress-strain curve (see Figure 4) are associated to a strain rate history the cross section has been exposed to. The longitudinal local strain rate history obtained during the deformation process for the material investigated here is illustrated in Figure 5 and calculated according to a backward finite difference scheme:

$$\dot{\epsilon} = \frac{\epsilon_{t+\Delta t} - \epsilon_t}{\Delta t} \quad (8)$$

This information is crucial for the correct calibration of material models, as it will be explained later. An interesting aspect of the strain rate history of the material investigated here is that both global and local strain rate values are about of the same order, thus indicating that necking phenomenon occurs in a gradual manner. This observation can also be deduced from the smoothly softening behavior of the true stress-strain curve of Figure 4. Contrary, other observations have been reported in the literature where large deviations between local and global strain rates have been measured [6, 8, 10].

Because of the low frame rate of the cameras used it was not possible to capture precisely the strain level at failure, thus, the last point reported in Figure 4 ($\epsilon = 1.13$) represents a strain level close to failure (see also the last point of Figure 5,

where a tendency of strain rate increase can be observed).

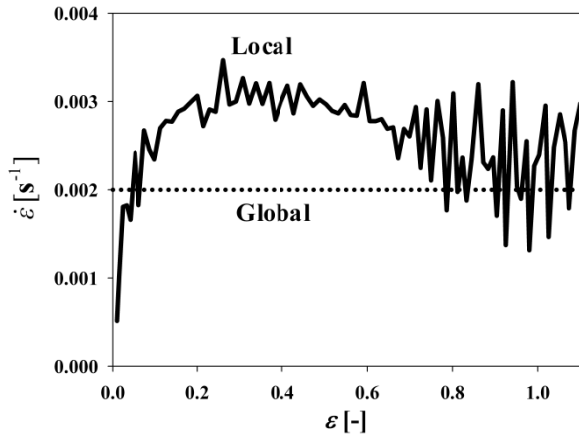


Figure 5 Local strain rate measurements by DIC.

3.3 Volumetric strain response

Considering the same “critical” section and the 3D DIC set-up, transversal strains along the width and the thickness of the tensile test specimen could be measured. True strain measurements (transversal vs. longitudinal) are presented in Figure 6, where it is possible to observe the close similarity between strain values along the width and thickness direction.

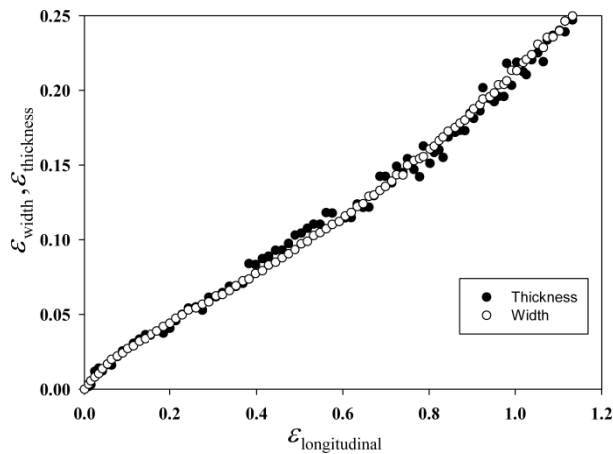


Figure 6 Verification of transversal isotropy for the PP copolymer material.

Hence, confirming that for this material, the transversal isotropy condition during the deformation process. On the other hand, utilizing the definition of the elastic Poisson’s ratio during

the whole deformation process, i.e.

$$v_w = \frac{-\epsilon_{width}^T}{\epsilon_{longitudinal}} \text{ and } v_t = \frac{-\epsilon_{thickness}^T}{\epsilon_{longitudinal}}$$

as a function of the longitudinal strain $\epsilon_{longitudinal}$

can be constructed, see Figure 7. In the elastic range a Poisson’s ratio close to 0.4 can be deduced while a smoothly reduction until an asymptotic value close to 0.20 is observed in the inelastic regime. Thus, indicating that the PP copolymer material studied here presents large volumetric plastic dilatation, due, probably, to damage and crazes creation at the micro scale level.

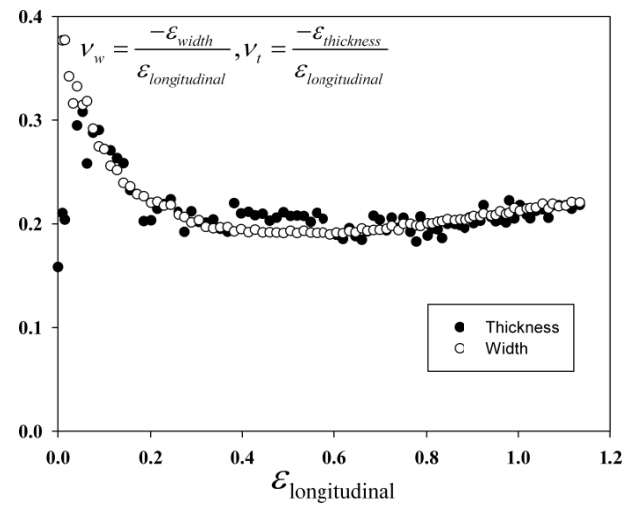


Figure 7 Variation of Poisson’s ratio during the whole deformation process.

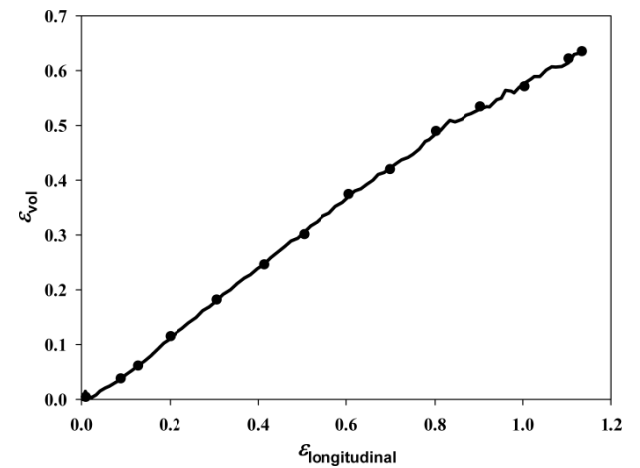


Figure 8 Total volumetric dilatation during the whole deformation process.

These results are summarized, for calibration purposes, in Figure 8, where the total volumetric strain ($\varepsilon_{vol} = \varepsilon_{width} + \varepsilon_{thickness} + \varepsilon_{longitudinal}$) is plotted against the longitudinal strain $\varepsilon_{longitudinal}$. This figure represents the average response of two parallels. The averaged response is also characterized by some discrete points (black) which will be used later as the target solution for calibration of the plastic potential parameter β , see Equation(3).

3.4 Compression tests

Two compressive tests on the PP copolymer were performed on cubic specimens. These tests were carried out under displacement control, applying a constant velocity of 2 mm/min to the machine's upper cross-head. This velocity was kept constant during the entire test. The rate of deformation corresponds to a nominal strain rate of 0.00833 s^{-1} . The cubic samples had a main dimension of 4 mm per side.

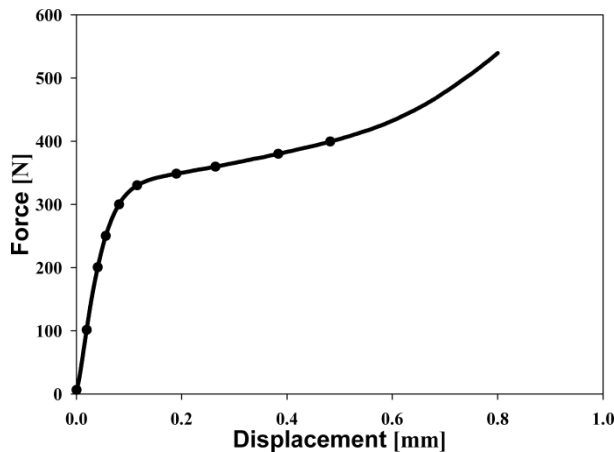


Figure 9 Force-displacement response for the compression test.

The averaged force-displacement curve of the two tests is shown in Figure 9; as registered by the servohydraulic machine. It is well known, that because of friction and planarity is very difficult to perform uniaxial compression tests with homogeneous stress and strain distributions. Consequently, DIC techniques are preferred to capture the potential strain inhomogeneities that the boundary conditions could have introduced. Unfortunately, DIC was not used in the compression tests and it was necessary to assume that the deformation is uniform during the first stage of the test. Hence, it is believed that until

strain levels of 10 to 20 % the registered measurements, from the servohydraulic machine, characterize the compressive behavior of the material relatively well. Therefore for material calibration purposes only one portion of the stress-strain curve in compression will be used (indicated with the black points in Figure 9).

4. Inverse modeling strategy

4.1 Introduction

Material parameters identification by inverse modeling relies on, basically, a non-linear optimization technique where a certain objective function is minimized. Commonly, the objective function is assumed as the residual norm between numerical and experimental results. The establishment of the target (e.g. experiments) solution depends largely on the material and measurement technique used, among others. For material identification purposes three types of solution strategies are usually encountered in the literature [11-13, 15-16]:

- A) Global approach based on force-displacement response
- B) Local approach based on stress-strain response
- C) Mixed approach based on both global and local responses

It is worthy to mention that, because of the necessity of modeling the whole specimen (or part of it) alternative A demands relatively high computational resources while C requires, both, advanced experimental and computational resources. On the other hand, the option B imposes access to the stress-strain history in one or various material points of the specimen. This information is obtainable with the DIC technique as employed in this work. The computational resources are minimal because the calibration procedure uses only one finite element to characterize the material point behavior. Alternatively, material model driver, where strain rate history is prescribed, could have been used.

One important aspect of the calibration procedure is the correct data transfer between experiments and finite element loading conditions, in particular for option B strategy. Indeed, because of necking and strain rate effects global and local strains can be quite different. Therefore, any true stress-strain curve to be used for material characterization should have a strain rate history

associated to it [29]. In essence, the applied displacement control of the finite element used must follow the experimental local strain and the time history according to:

$$u(t) = L \left(\exp^{\varepsilon(t)_{local}} - 1 \right) \quad (9)$$

where L represents any arbitrary initial element length of the finite element used, $\varepsilon(t)_{local}$ the measured local strain and $u(t)$ the displacement history to be applied, see Figure 10.

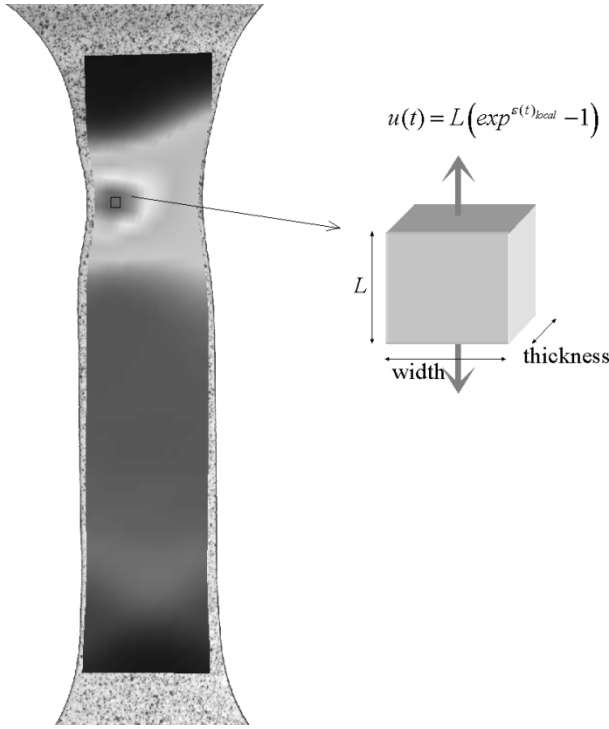


Figure 10 Local response strategy for material calibration purposes.

Finally, we should mention that this local strategy can be enhanced by including more “material points”, to represent the stress-strain behavior of different cross sections of the specimen, each of them with their corresponding strain rate history.

The constitutive model requires the identification of 9 material parameters. The elastic constants of part A (e.g. the Young’s modulus E and the Poisson’s ratio ν) are identified by reproducing an averaged linear response of the actual non-linear behavior. For this, we use the uniaxial tensile test submitted to the lowest loading strain rate (e.g. $\dot{\varepsilon}_0$). Next, the parameter C is identified using the nominal stress-strain curves at

different strain rates with the reference strain rate $\dot{\varepsilon}_0$ taken as the lowest strain rate used in the tests. Using the true stress-strain curve and the volumetric strain response as the main targets the identification of the four variables σ_T , C_R , N and β is done by inverse modeling using the local response approach (B strategy). Finally, the parameter α , which defines the pressure sensitivity of the yield stress, is calibrated from a uniaxial compression test using a similar local approach.

4.2 The response surface methodology (RSM)

Identification of the material parameters was performed with the optimization software LS-OPT [17]. The optimization technique used relies on the response surface methodology, a mathematical method for constructing smooth approximations of functions in a design space.

Let us assume that the response of a system is characterized by the function $f(\mathbf{x})$. This function can represent the results of finite element analyses. The response surface methodology (RSM) seeks to iteratively fit the function $f(\mathbf{x})$ with the approximation, $\tilde{f}(\mathbf{x})$, in a least-square sense. This approximating function can be written as a sum of products of the interpolation functions, ϕ_i , with the undetermined coefficients (e.g. the regression constants), a_i , as:

$$\tilde{f}(\mathbf{x}) = \sum_{i=1}^L a_i \phi_i(\mathbf{x}) \approx f(\mathbf{x}) \quad (10)$$

where L is the number of the interpolation functions and \mathbf{x} is the independent variables (e.g. design variables) vector. To obtain an approximate solution we must determine values of a_i such that

f and \tilde{f} remains as close as possible. For this purpose, the approximation functions are evaluated at N experimental points and the unknown constants (a_i , $i = 1, \dots, L$) are then determined by forcing the sum of errors squared, ε^2 , to be minimized, according to:

$$\varepsilon^2 = \sum_{j=1}^N [f(\mathbf{x}_j) - \tilde{f}(\mathbf{x}_j)]^2 = \sum_{j=1}^N [f(\mathbf{x}_j) - a_i \phi_i(\mathbf{x}_j)]^2 \quad (11)$$

By collecting f and \tilde{f} in a vector form and defining the error vector as $\boldsymbol{\varepsilon} = \mathbf{f} - \tilde{\mathbf{f}}$, the matrix notation of Equation (11) can be re-written as:

$$\boldsymbol{\varepsilon}^2 = \boldsymbol{\varepsilon}^T \boldsymbol{\varepsilon} = (\mathbf{f} - \tilde{\mathbf{f}})^T (\mathbf{f} - \tilde{\mathbf{f}}) = (\mathbf{f} - \mathbf{X}\mathbf{a})^T (\mathbf{f} - \mathbf{X}\mathbf{a}) \quad (12)$$

Where $\mathbf{a} = [a_1 \ a_2 \ \dots \ a_L]^T$ is the undetermined constants vector and \mathbf{X} is the interpolation matrix defined as:

$$\mathbf{X} = \begin{bmatrix} \phi_1(\mathbf{x}_1) & & \phi_L(\mathbf{x}_1) \\ \phi_1(\mathbf{x}_2) & \dots & \phi_L(\mathbf{x}_2) \\ \cdot & \cdot & \cdot \\ \cdot & \cdot & \cdot \\ \phi_1(\mathbf{x}_N) & \dots & \phi_L(\mathbf{x}_N) \end{bmatrix}_{N \times L} \quad (13)$$

The undetermined coefficients, a_i , can be determined by minimizing Equation (12) in the form $\frac{\partial(\boldsymbol{\varepsilon}^2)}{\partial \mathbf{a}} = 2\mathbf{X}^T \mathbf{X}\mathbf{a} - 2\mathbf{X}^T \mathbf{f} = 0$, which yields:

$$\mathbf{a} = [\mathbf{X}^T \mathbf{X}]^{-1} \mathbf{X}^T \mathbf{f} \quad (14)$$

Equation (14) defines the coefficients a_i of the approximation function $\tilde{f}(\mathbf{x})$ which represent the best fit to the function $f(\mathbf{x})$. The LS-OPT software [17] uses, in addition, an adaptive surface response generator known as the successive response surface method (SSRM). This technique focuses on the automatic creation of a subspace of the design space. By successive iterations nested sub-regions are generated with advancements of panning and zooming steps. A more in-depth study of this technique can be found in [17].

Finally, for this purposes of this work a linear order approximation model was used together with a D-optimality criterion for the selection of the experimental points.

5. Numerical calibration

5.1 Parameter identification procedure

The calibration procedure can become cumbersome because the seven variables, describing the non-linear behavior, are in some degree coupled to each other and a detailed knowledge of the constitutive model is necessary to facilitate such identification. The strain rate parameters C and $\dot{\varepsilon}_0$, of our model, do not have any effect on the “hardening” shape and volumetric strain response; they only affect the expansion of the yield surface by a scaling factor. Thus, according to our strategy, these two parameters should be identified first from the nominal stress-strain data. The “plastic” variables σ_T , C_R and N are mainly the responsible of the true stress-strain behavior and they are weakly coupled with the volumetric response. The plastic potential is characterized by the constant β which controls the volumetric plastic dilatation and the evolution of the cross section (e.g. true stress). Consequently, the uniaxial true stress-strain response is affected by the β parameter.

The identification procedure of the material parameters is based on the comparison between the numerical response and the experimental data by minimizing the least square residual (LSR) according to the expressions [29]:

$$\begin{aligned} \min LSR(\mathbf{x}) &= \sqrt{\sum_{i=1}^N [\sigma(\varepsilon_i)_{\text{exp}} - \sigma(\mathbf{x}, \varepsilon_i)_{\text{num}}]^2} \\ \min LSR(\mathbf{x}) &= \sqrt{\sum_{i=1}^N [\varepsilon^{\text{vol}}(\varepsilon_i)_{\text{exp}} - \varepsilon^{\text{vol}}(\mathbf{x}, \varepsilon_i)_{\text{num}}]^2} \end{aligned} \quad (15)$$

with respect to the design variables, $\mathbf{x} = [\sigma_T \ C_R \ N \ \beta]^T$. Where, σ_T is the yield stress in tension. C_R and N are the “hardening” variables and β is the parameter which controls the volumetric plastic strains.

5.2 Identification of the strain rate parameters

The nominal stress-strain responses (see Figure 3) of the four tensile tests are used for identification of the strain rate parameters.

The tests were submitted to nominal strain rate values of 2×10^{-4} , 2×10^{-3} , 2×10^{-2} and $1 \times 10^{-1} \text{ s}^{-1}$. The lowest strain rate used is chosen as the reference strain rate, $\dot{\epsilon}_0 = 2 \times 10^{-4}$. In addition, for each nominal strain rate value the maximal stress (at total strain level of 3 %) is taken to build up the diagram of Figure 11. A value of $C = 0.073$ is found for this material.

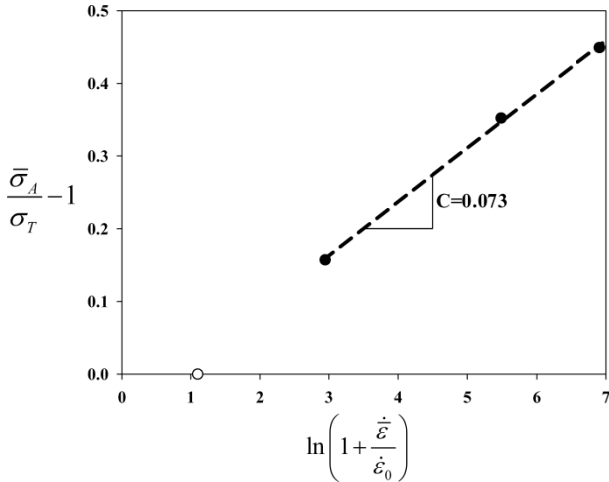


Figure 11 Identification of material parameters C and $\dot{\epsilon}_0$.

5.3 Identification of σ_T, C_R, N and β using inverse modeling

We use the optimization software LS-OPT [17] to perform the identification procedure of the variables σ_T, C_R, N and β . At this stage, the elastic constants were assumed as $E = 1500 \text{ MPa}$ and $\nu = 0.40$, based on the experimental results. Next, we fixed the strain rate parameters according to the results found previously ($C = 0.073$ and $\dot{\epsilon}_0 = 2 \times 10^{-4}$). The identification procedure is based on the minimization of two objective functions related to the true stress-strain behavior and the volumetric response. We use the default linear optimization algorithm (LOFP). The finite element used (e.g. 8 node hexahedral) is submitted to a local strain rate history according to Figure 5. The values obtained are shown in Table 1.

Furthermore, the comparisons between numerical and experimental responses are shown in Figure 13. It should be mentioned that we

Table 1. Identification of material parameters

σ_T (MPa)	C_R (MPa)	N	β
12.90	0.927	4.35	1.47

assumed a pressure sensitivity value of $\alpha = 1.17$ in the identification procedure. This parameter is weakly coupled to the stress-strain and volumetric response of the tensile test; hence, the values indicated in Table 1.

are the outcome of the α assumed in the optimization. In order to illustrate this observation we perform a new identification procedure but this time assuming a value of $\alpha = 1.0$. The new resulting values were $\sigma_T = 12.91$, $C_R = 0.86$, $N = 4.27$ and $\beta = 1.47$ which are quite similar to these indicated in Table 1, corroborating then the slight influence of on the stress-strain and volumetric tensile responses. Figure 13 illustrates the variation of one of the design variables (e.g. the yield stress, σ_T) given by LS-OPT during iteration of the optimal solution.

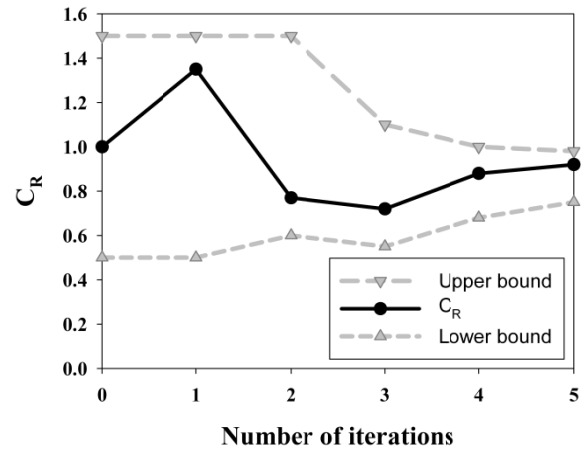


Figure 12 variation of the design variable C_R during iteration of the optimization procedure.

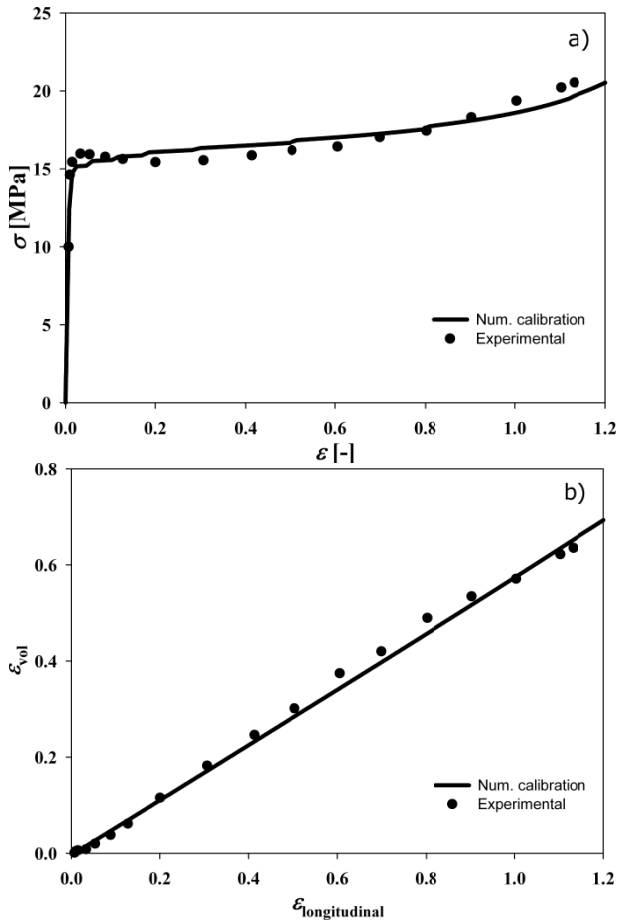


Figure 13 Identification of σ_T, C_R, N and β based on a) Tensile true stress-strain response b) Tensile volumetric response.

5.4 Identification of the pressure dependent parameter

Finally, the identification of the parameter α , which defines the pressure dependence of the yield stress, is calibrated from the experimental load-displacement curve from the compression test. The optimization procedure yields a value of $\alpha = 1.168$ which compares fairly well with the assumed value of $\alpha = 1.17$. It should be pointed out that an iterative procedure is required if large deviations between the assumed α value (used to perform the optimization of the design variables \mathbf{x}) and that found from the minimization of the compressive response exist. This situation was unnecessary in our case.

5.5 Numerical verification using the uniaxial tensile test

The inverse modeling strategy used in this work is, in fact, a combination of global and local responses, in the sense that, nominal (global) stress-strain results are used to identify the strain

rate parameters and true (local) stress-strain-volume curves were used to identify the four “plastic” parameters which characterize the “yielding” behavior. This section intends to show the capability of the constitutive model presented in section 2 to predict the experimental tensile response the main parameter were identified from. For this purpose we perform a numerical analysis of the tensile specimen using the finite element mesh illustrated in Figure 14. The cross section of

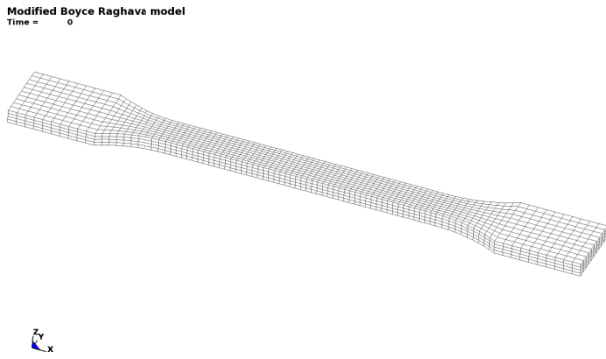


Figure 14 Finite element model of the tensile specimen.

the specimen was $10 \times 4 \text{ mm}^2$ while the global displacement was monitored with an extensometer of 50 mm gauge length. The set of parameters

Table 2 Material parameters for the PP copolymer

E (MPa)	ν	C	$\dot{\epsilon}_0$ (1/s)	σ_T (MPa)	C_R (MPa)	N	β	α
1500	0.40	0.073	2×10^{-4}	12.90	0.927	4.35	1.47	1.17

failure occurrence. The strain level predicted by the numerical model was underestimated ($\epsilon_{xx} = 0.65$). However, these results are improved if a geometrical imperfection is introduced in the FE model to trigger strain localization, as illustrated in Figure 16. In this figure a strain level of $\epsilon_{xx} = 0.82$ is attained and it compares relatively well to that observed at failure, $\epsilon_{xx} = 1.13$.

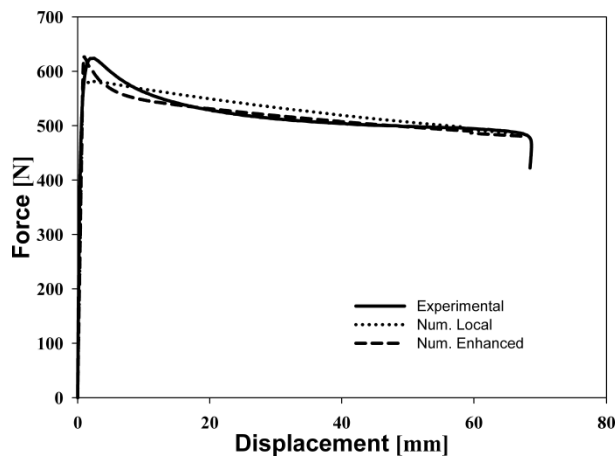


Figure 15 Numerical prediction of the uniaxial tensile test and its comparison with the experimental response.

adopted (found in the previous sections) are indicated in Table 2.

A comparison between the experimental test response and numerical simulations is shown in the force-displacement curve of Figure 15. Deviation of about 6 % (e.g. over and under predictions) in the load-carrying capacity are observed. Because there is no failure criterion introduced in the model the analysis was stopped at a displacement level of 67 mm while the specimen presented rupture at a displacement of 68 mm. Furthermore, the numerical model predicted a uniform strain distribution without any indication of strain localization; contrary, to the experiments where strain localization was observed just before



Figure 16 Strain localization prediction by introducing a geometrical imperfection.

Finally, it is believed that the deviations observed are more related to the robustness of the

constitutive model used than, in a less degree, on the parameter identification strategy adopted. In this direction some enhancements of the constitutive model to capture hardening/softening behavior are under development. Some preliminary results indicate that introducing an isotropic hardening/softening response in Part A the numerical prediction of the tensile test is enhanced, as illustrated in Figure 15.

6. Conclusion

Three main ingredients included in this work are: A short description of the MBR constitutive model, an experimental program, on a PP copolymer, consisting of uniaxial tension and compression tests and an inverse modeling strategy for material identification purposes. The MBR model is suitable for the analysis of thermoplastic structural components subjected to quasi-static or impact loading conditions and it requires the characterization of 9 parameters. Some of the model parameters are identified directly from the experimental results. Indeed, the elastic constants (E, ν) is taken from the true stress-strain curve and the lateral strain measurements, respectively. In addition, the strain rate parameters ($C, \dot{\epsilon}_0$) are identified from the nominal stress-strain curves of four uniaxial tensile tests at different strain rates. An inverse modeling strategy is adopted to identify the other 5 material constants. The pressure dependent parameter (α) is calibrated by minimization of one objective function related to the force-displacement response in compression. The “plastic” variables σ_T, C_R, N and β are found from minimizing two objective functions related to the true stress-strain behavior and the volumetric response, simultaneously.

The main experimental data, of the PP copolymer investigated here, is measured by 3D-DIC technique, where the common transversal isotropy assumption is avoided. However, such common hypothesis is verified for the material studied here. Next, volumetric plastic dilatation could be confirmed due, possibly, to damage and craze formation during deformation process.

Finally, the inverse modeling approach is based on a local strategy where the correct data transfer between experiments and finite element loading conditions is guaranteed. Accordingly, local strain rate values, measured from DIC, are directly applied as the loading condition to the finite element used to represent the material point. The methodology presented in this work can be extended to include the local temperature history due to adiabatic heating process in the necking zone. Indeed, measurements of local temperature jumps of 26 °C on an ABS polymer, using an infrared camera, have been reported by Louche et al. [30]. With this additional information reliable identification procedures can be expected on constitutive models with temperature dependent parameters.

Acknowledgements

The present work was carried out with financial support from SINTEF Materials and Chemistry under the internal SEP program MechPol-2008.

References

1. M. Polanco-Loria, A.H. Clausen, T. Berstad, and O.S. Hopperstad, *A constitutive model for thermoplastics in structural applications*, in *14th International Conference on Deformation, Yield and Fracture of Polymers*. 2009: Kerkrade, The Netherlands. p. 261-264.
2. M. Polanco-Loria, A.H. Clausen, T. Berstad, and O.S. Hopperstad, *A constitutive model for thermoplastics intended for structural applications*, in *7th European LS-DYNA Conference 2009*: Salzburg, Austria. p. D-II-3.
3. M. Polanco-Loria, A.H. Clausen, T. Berstad, and O.S. Hopperstad, *Constitutive model for thermoplastics with structural applications*. *International Journal of Impact Engineering*, 2010. **37**(12): p. 1207-1219.
4. S. Castagnet, J.L. Gacougnolle, and P. Dang, *Macroscopic volume changes of PVF2 undergoing uniaxial tension and creep*. *Journal of Materials Science*, 1999. **34**(20): p. 5133-5138.
5. G.D. Dean and R.D. Mera, *Measurement of failure in tough plastics at high strain rates*. 2005, NPL.
6. Q.Z. Fang, T.J. Wang, H.G. Beom, and H.P. Zhao, *Rate-dependent large deformation behavior of PC/ABS*. *Polymer*, 2009. **50**(1): p. 296-304.
7. C. G'Sell, J.M. Hiver, and A. Dahoun, *Experimental characterization of deformation damage in solid polymers under tension, and its interrelation with necking*. *International Journal of Solids and Structures*, 2002. **39**(13-14): p. 3857-3872.
8. R.T. Moura, A.H. Clausen, E. Fagerholt, M. Alves, and M. Langseth, *Impact on HDPE and PVC plates - Experimental tests and numerical simulations*. *International Journal of Impact Engineering*, 2010. **37**(6): p. 580-598.
9. E. Parsons, M.C. Boyce, and D.M. Parks, *An experimental investigation of the large-strain tensile behavior of neat and rubber-toughened polycarbonate*. *Polymer*, 2004. **45**(8): p. 2665-2684.
10. G. Spathis and E. Kontou, *Experimental and theoretical description of the plastic*

- behaviour of semicrystalline polymers.* Polymer, 1998. **39**(1): p. 135-142.
11. G.B. Broggiato, F. Campana, and L. Cortese, *Identification of material damage model parameters: An inverse approach using digital image processing.* Meccanica, 2007. **42**(1): p. 9-17.
 12. S. Cooreman, D. Lecompte, H. Sol, J. Vantomme, and D. Debruyne, *Identification of mechanical material behavior through inverse modeling and DIC.* Experimental Mechanics, 2008. **48**(4): p. 421-433.
 13. D.R. Einstein, A.D. Freed, N. Stander, B. Fata, and I. Vesely, *Inverse parameter fitting of biological tissues: A response surface approach.* Annals of Biomedical Engineering, 2005. **33**(12): p. 1819-1830.
 14. M. Grediac and F. Pierron, *Applying the virtual fields method to the identification of elasto-plastic constitutive parameters.* International Journal of Plasticity, 2006. **22**(4): p. 602-627.
 15. E. Omerspahic, K. Mattiasson, and B. Enquist, *Identification of material hardening parameters by three-point bending of metal sheets.* International Journal of Mechanical Sciences, 2006. **48**(12): p. 1525-1532.
 16. N. Stander, K.J. Craig, H. Mullerschön, and R. Reichert, *Material identification in structural optimization using response surfaces.* Structural and Multidisciplinary Optimization, 2005. **29**(2): p. 93-102.
 17. N. Stander, W. Roux, T. Goel, T. Eggelston, and K. Craig, *LS-OPT User's manual.* 2008, Livermore Software Technology Corporation.
 18. R.N. Haward and G. Thackray, *The Use of a Mathematical Model to Describe Isothermal Stress-Strain Curves in Glassy Thermoplastics.* Proceedings of the Royal Society of London. Series A. Mathematical and Physical Sciences, 1968. **302**(1471): p. 453-472.
 19. M.C. Boyce, *Large inelastic deformation of glassy polymers,* in *Department of Mechanical Engineering.* 1986, Massachusetts Institute of Technology: Boston, USA.
 20. M.C. Boyce, S. Socrate, and P.G. Llana, *Constitutive model for the finite deformation stress-strain behavior of poly(ethylene terephthalate) above the glass transition.* Polymer, 2000. **41**(6): p. 2183-2201.
 21. R. Raghava, R.M. Caddell, and G.S.Y. Yeh, *The macroscopic yield behaviour of polymers.* Journal of Materials Science, 1973. **8**(2): p. 225-232.
 22. B. Moran, M. Ortiz, and C.F. Shih, *formulation of implicit finite-element methods for multiplicative finite deformation plasticity.* International Journal for Numerical Methods in Engineering, 1990. **29**(3): p. 483-514.
 23. J.O. Hallquist, *LS-DYNA keyword user's manual,* Livermore Software Technology Corporation.
 24. F. Grytten, H. Daiyan, M. Polanco-Loria, and S. Dumoulin, *Use of digital image correlation to measure large-strain tensile properties of ductile thermoplastics.* Polymer Testing, 2009. **28**(6): p. 653-660.
 25. www.correlatedsolutions.com
 26. G.D. Dean and R.D. Mera, *Determination of material properties and parameters required for the simulation of impact performance of plastics using finite element analysis.* 2004, NPL.
 27. T. Glomsaker, E. Andreassen, M. Polanco-Loria, O.V. Lyngstad, R.H. Gaarder, and E.L. Hinrichsen, *Mechanical response of injection-moulded parts at high strain rates,* in *Polymer Processing Society Europe/Africa Regional meeting.* 2007: Gothenburg, Sweden.
 28. J. Mohanraj, D.C. Barton, I.M. Ward, A. Dahoun, J.M. Hiver, and C. G'Sell, *Plastic deformation and damage of polyoxymethylene in the large strain range at elevated temperatures.* Polymer, 2006. **47**(16): p. 5852-5861.
 29. M. Polanco-Loria, S. Dumoulin, and T. Coudart, *Computational modelling of thermoplastics: Parameter identification procedure,* in *10th International Conference on Computational Plasticity: Fundamentals and Applications.* 2009: Barcelona, Spain.
 30. H. Louche, F. Piette-Coudol, R. Arrieux, and J. Issartel, *An experimental and modeling study of the thermomechanical behavior of an ABS polymer structural component during an impact test.* International Journal of Impact Engineering, 2009. **36**(6): p. 847-861.